SOLARNET-FoMICS Summer School ”Solar spectropolarimetry: From virtual to real observations”

September 9-14, 2019, Università della Svizzera italiana, Lugano

Aspects of magnetohydrodynamic simulations of stellar atmospheres

Oskar Steiner

Istituto Ricerche Solari Locarno (IRSOL), Locarno and

Leibniz-Institut für Sonnenphysik (KIS), Freiburg i.Br.

steiner@leibniz-kis.de

Table of content

Table of content (cont.)

Part I:

Fundamentals of the numerics of hyperbolic partial differential equations

§ 1 Linear and non-linear advection equations

We start with the *continuity equation* as the reference equation for advection:

$$\boxed{\frac{\partial \rho}{\partial t} + \boldsymbol{\nabla} \cdot (\rho \boldsymbol{v}) = 0 \, ,} \quad \frac{\partial}{\partial t} \int_{\mathcal{V}} \rho \, \mathrm{d}V = - \oint_{\partial \mathcal{V}} (\rho \mathbf{v}) \cdot \mathbf{n} \, \mathrm{d}a$$

in 1-D

$$\frac{\partial \rho}{\partial t} + \frac{\partial}{\partial x}(\rho u) = 0 \, .$$

With $u = \mathrm{const.}$ (the advection velocity) we get the *linear advection equation*

$$\frac{\partial \rho}{\partial t} + u \frac{\partial \rho}{\partial x} = 0 \, .$$

Its solution is

$$\rho(x, t) = \rho_0(x - ut) \, .$$

Linear and non-linear advection equations (cont.)

The initial density profile is simply moved (advected) with velocity u.

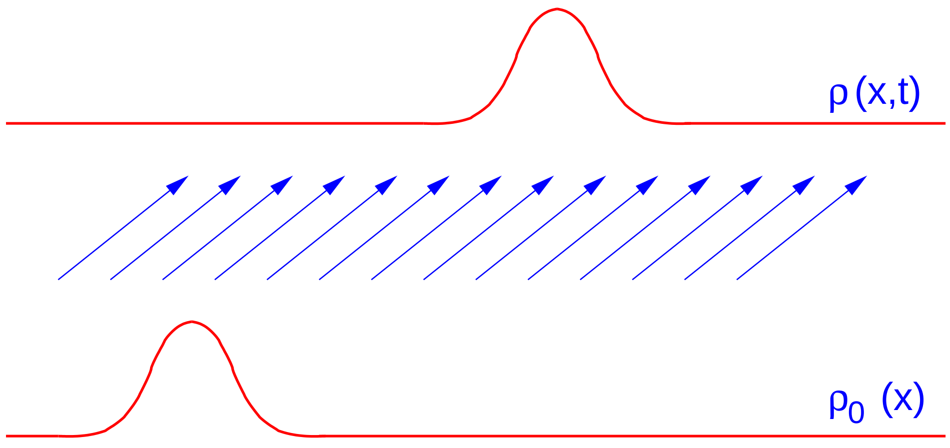

The initial density profile is simply moved (advected) with velocity u.

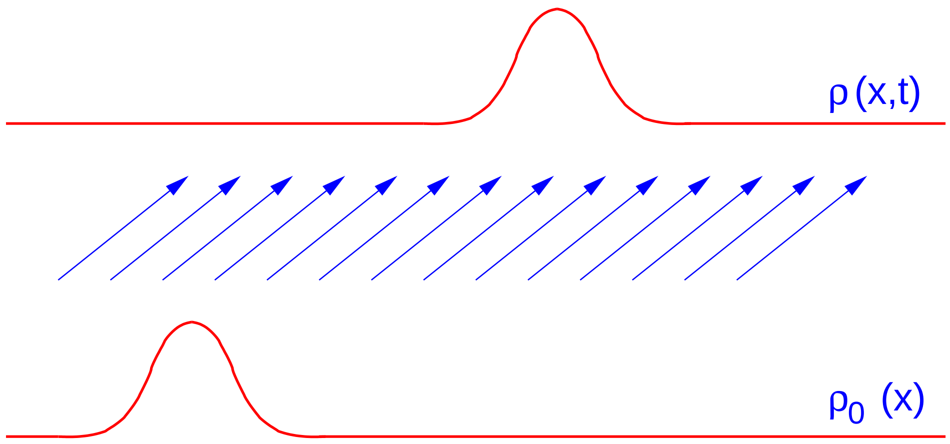

Representation on a discrete numerical Eulerian grid:

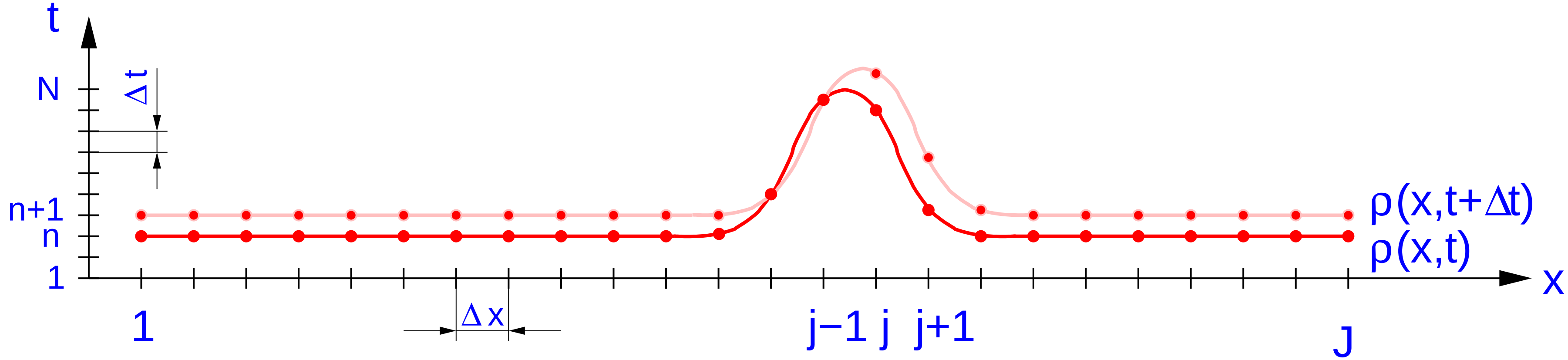

Linear and non-linear advection equations (cont.)

$$\boxed{\frac{\partial \rho}{\partial t} + u\frac{\partial \rho}{\partial x} = 0} \quad \Longrightarrow \quad \frac{\partial \rho}{\partial t} + u\frac{\rho_j - \rho_{j-1}}{\Delta x} = 0$$

Taylor expansion:

$$\rho_{j-1} = \rho_j - \left.\frac{\partial \rho}{\partial x}\right|_j \Delta x + \frac{1}{2}\left.\frac{\partial^2 \rho}{\partial x^2}\right|_j \Delta x^2 - \frac{1}{6}\left.\frac{\partial^3 \rho}{\partial x^3}\right|_j \Delta x^3 + \ldots$$

Substitution:

$$\underbrace{\boxed{\frac{\partial \rho}{\partial t} + u\left.\frac{\partial \rho}{\partial x}\right|_j}}_{\text{original l.h.s.}} - \underbrace{\overbrace{\frac{1}{2}\Delta x\, u}^{\text{diffusion coefficient}}\left.\frac{\partial^2 \rho}{\partial x^2}\right|_j}_{\text{diffusive term}} + \underbrace{\frac{1}{6}u\,\Delta x^2\left.\frac{\partial^3 \rho}{\partial x^3}\right|_j - \ldots}_{\text{higher order terms}} = 0$$

The diffusion term looks like a viscous term with viscosity $(\Delta x/2)u$.

Linear and non-linear advection equations (cont.)

$$\boxed{\frac{\partial \rho}{\partial t} + u\frac{\partial \rho}{\partial x} = 0} \quad \Longrightarrow \quad \frac{\partial \rho}{\partial t} + u\frac{\rho_j - \rho_{j-1}}{\Delta x} = 0$$

Taylor expansion:

$$\rho_{j-1} = \rho_j - \left.\frac{\partial \rho}{\partial x}\right|_j \Delta x + \frac{1}{2}\left.\frac{\partial^2 \rho}{\partial x^2}\right|_j \Delta x^2 - \frac{1}{6}\left.\frac{\partial^3 \rho}{\partial x^3}\right|_j \Delta x^3 + \ldots$$

Substitution:

$$\underbrace{\boxed{\frac{\partial \rho}{\partial t} + u\left.\frac{\partial \rho}{\partial x}\right|_j}}_{\text{original l.h.s.}} - \underbrace{\overbrace{\frac{1}{2}\Delta x\, u}^{\text{diffusion coefficient}} \left.\frac{\partial^2 \rho}{\partial x^2}\right|_j}_{\text{diffusive term}} + \underbrace{\frac{1}{6} u\, \Delta x^2 \left.\frac{\partial^3 \rho}{\partial x^3}\right|_j - \ldots}_{\text{higher order terms}} = 0$$

The diffusion term looks like a viscous term with viscosity $(\Delta x/2)u$.

Lesson: The discrete scheme does not solve the original equation but the original equation with an inherent numerical diffusion term added.

Linear and non-linear advection equations (cont.)

It is remarkable that Eulerian numerical schemes have generally difficulties to solve the linear advection equation accurately. Some amount of diffusion is unavoidable.

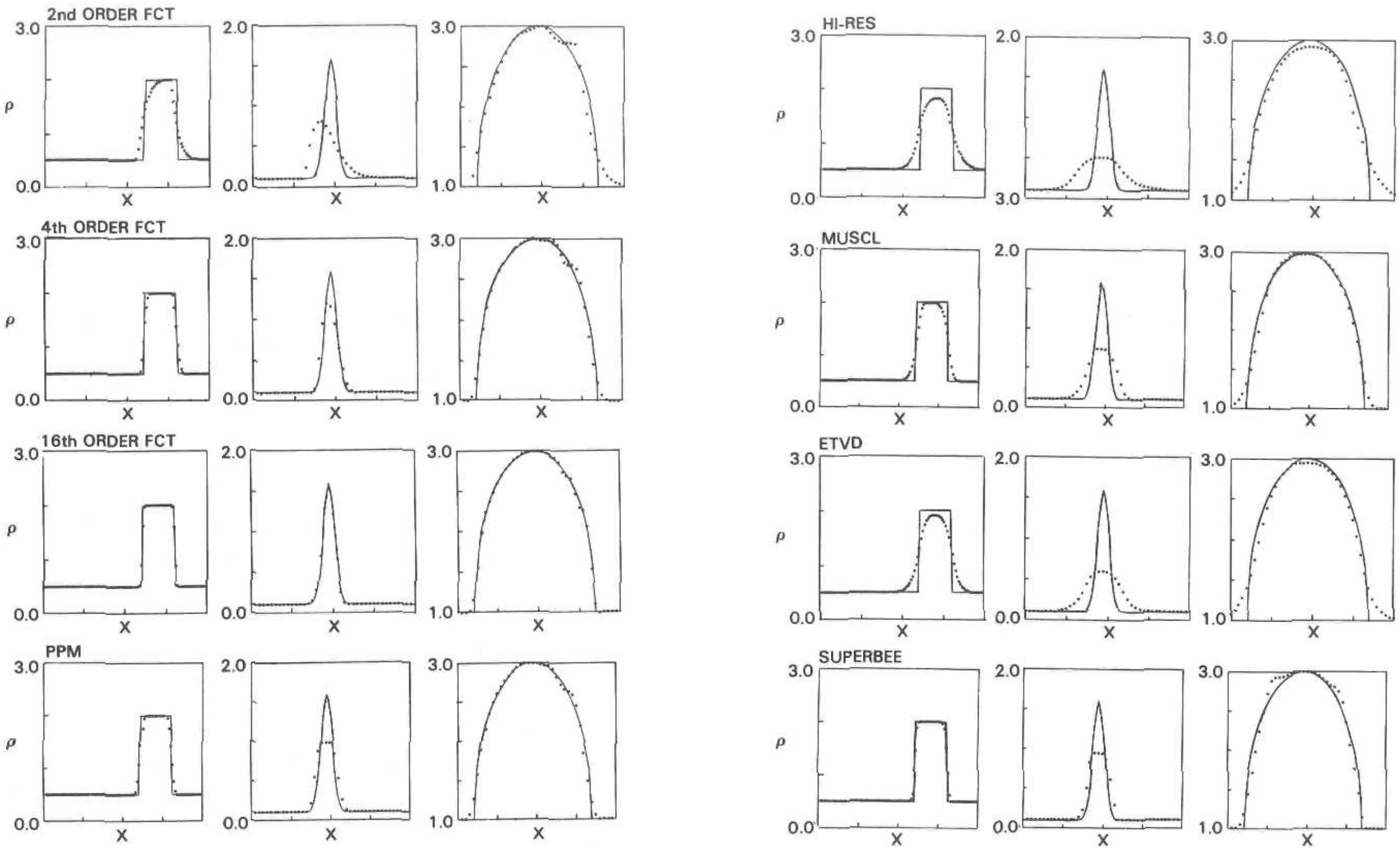

From *Oran & Boris (1987)*

We next consider the momentum equation

$$\frac{\partial}{\partial t}(\rho u) + \frac{\partial}{\partial x}(\rho u^2 + p) - \varepsilon \rho \frac{\partial^2 u}{\partial x^2} = 0 \ ,$$

and assume $p = 0$:

$$u\frac{\partial \rho}{\partial t} + \rho \frac{\partial u}{\partial t} + u^2 \frac{\partial \rho}{\partial x} + \rho 2u \frac{\partial u}{\partial x} - \varepsilon \rho \frac{\partial^2 u}{\partial x^2} = 0 \ .$$

Using the continuity equation, the first term can be written as:

$$u\frac{\partial \rho}{\partial t} = -u\frac{\partial}{\partial x}(u\rho) = -u^2\frac{\partial \rho}{\partial x} - u\rho\frac{\partial u}{\partial x}$$

$$\Rightarrow \quad \rho\frac{\partial u}{\partial t} + \rho u \frac{\partial u}{\partial x} - \rho\varepsilon\frac{\partial^2 u}{\partial x^2} = 0 \ .$$

Division by ρ and reordering terms leads to:

Burgers' equation

$$\boxed{\frac{\partial u}{\partial t} + u\frac{\partial u}{\partial x} = \varepsilon\frac{\partial^2 u}{\partial x^2}}$$

and the *inviscid Burgers' equation*

$$\boxed{u_t + uu_x = 0}$$

Linear and non-linear advection equations (cont.)

Burgers' equation

$$\boxed{\frac{\partial u}{\partial t} + u\,\frac{\partial u}{\partial x} = \varepsilon\,\frac{\partial^2 u}{\partial x^2}}$$

and the *inviscid Burgers' equation*

$$\boxed{u_t + u u_x = 0}$$

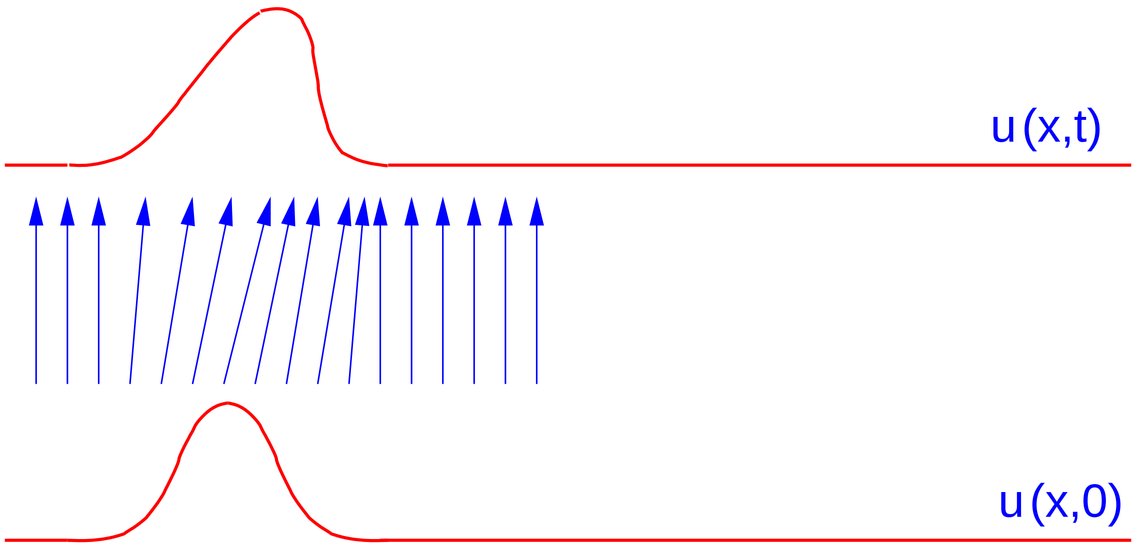

Solutions to the inviscid Burgers equation $u_t + uu_x = 0$:

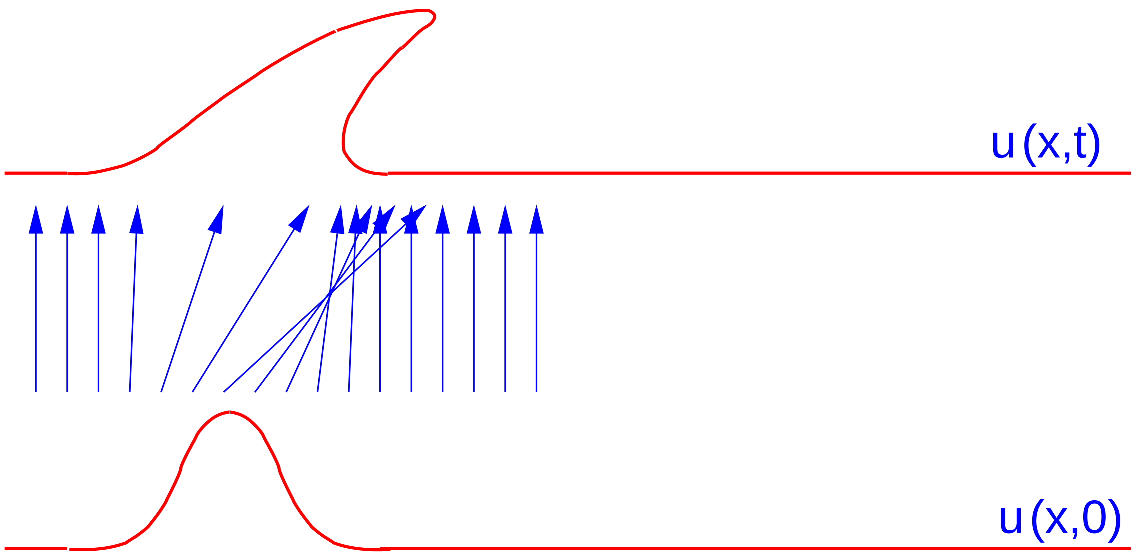

Solutions to the Burgers equation $u_t + uu_x = \varepsilon u_{xx}$:

Consider the inviscid Burgers equation $u_t + uu_x = 0$ with the initial data

$$u_0 = \begin{cases} 1 & \text{for} \quad x \le 0 \\ 0 & \text{for} \quad x > 0 \end{cases}$$

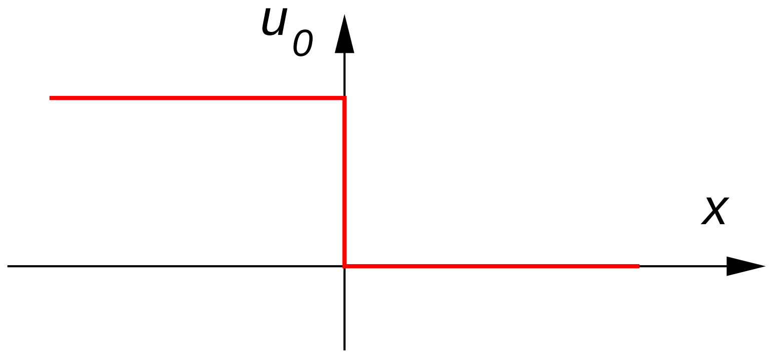

and construct a straightforward discretization:

$$\frac{U_j^{n+1} - U_j^n}{k} + U_j^n \left(\frac{U_j^n - U_{j-1}^n}{h} \right) = 0 \; ,$$

which is an ‘upwind” or “donor cell” scheme. How does this scheme handle the discontinuity of the initial data ?

First we rewrite the scheme in *explicite form*:

$$U_j^{n+1} = U_j^n - \frac{k}{h} U_j^n \left(U_j^n - U_{j-1}^n\right) \; .$$

Next we compute the first time step:

$$\begin{aligned}
\text{for} \quad x < 0: \quad U_j^1 &= 1 - \frac{k}{h} 1 \,(1 - 1) \quad &= 1 \, , \\
\text{for} \quad x > 0: \quad U_j^1 &= 0 - \frac{k}{h} 0 \,(0 - 0) \quad &= 0 \, , \\
\text{for} \quad U_{j-1} = 1 \quad \text{and} \quad U_j = 0: \quad U_j^1 &= 0 - \frac{k}{h} 0 \,(0 - 1) \quad &= 0 \, .
\end{aligned}$$

First we rewrite the scheme in *explicite form*:

$$U_j^{n+1} = U_j^n - \frac{k}{h} U_j^n \left(U_j^n - U_{j-1}^n \right) \ .$$

Next we compute the first time step:

$$\begin{aligned} \text{for} \quad x < 0 : \quad U_j^1 &= 1 - \frac{k}{h} 1 \, (1 - 1) \quad &= 1 \, , \\ \text{for} \quad x > 0 : \quad U_j^1 &= 0 - \frac{k}{h} 0 \, (0 - 0) \quad &= 0 \, , \\ \text{for} \quad U_{j-1} = 1 \quad \text{and} \quad U_j = 0 : \quad U_j^1 &= 0 - \frac{k}{h} 0 \, (0 - 1) \quad &= 0 \, . \end{aligned}$$

$\Rightarrow$ *After one time step we recover the initial data again!*

Whatever step size h and k we choose, the shock front stays at the same position.

Linear and non-linear advection equations (cont.)

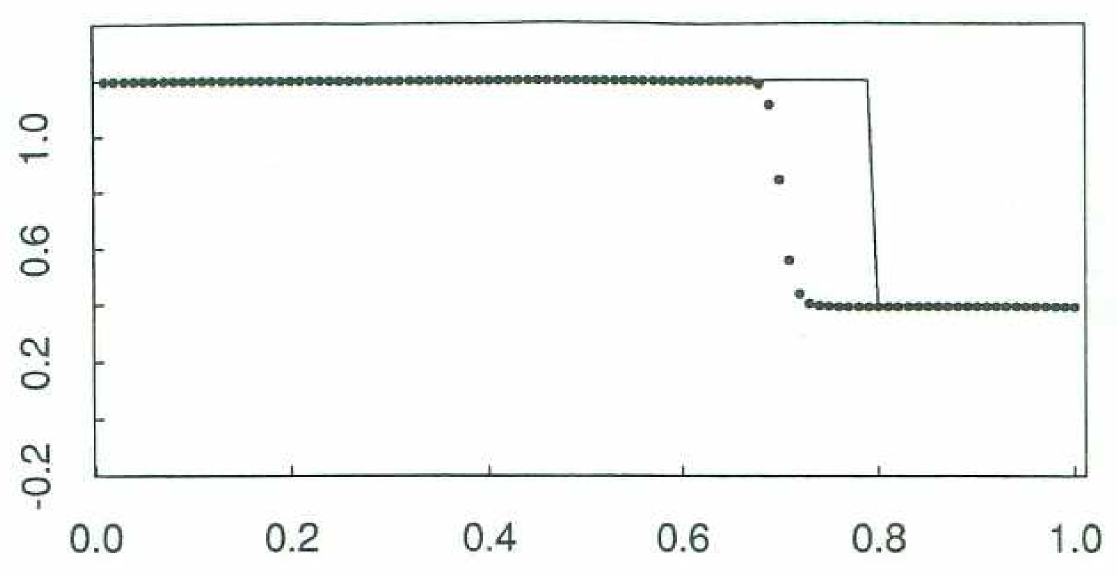

From *R.J. LeVeque (1992)*

True (solid curve) and computed (dotted curve) solution to Burgers' equation with adjacent initial data and using the upwind scheme. Note that the *shock speed is wrong*.

$$u_0 = \begin{cases} 1.2 & \text{for} \quad x \le 0 \\ 0.4 & \text{for} \quad x > 0 \end{cases}$$

§ 2 Conservative methods

A good way to obtain conservation law form ist to start discretization from the conservative form of the PDE.

For example in case of the inviscid Burgers equation:

$$\begin{aligned} \text{quasi linear form} \quad &: \quad u_t + u u_x &= 0 \,, \\ \text{conservative form} \quad &: \quad u_t + \left(\tfrac{1}{2}u^2\right)_x &= 0 \,. \end{aligned}$$

Using the same upwind discretization as before but starting from the conservative form of the PDE we obtain:

$$\frac{U_j^{n+1} - U_j^n}{k} + \frac{1}{h}\left[\frac{1}{2}(U_j^n)^2 - \frac{1}{2}(U_{j-1}^n)^2\right] = 0 \,.$$

The *explicit form* is

$$U_j^{n+1} = U_j^n - \frac{k}{h}\left[\frac{1}{2}(U_j^n)^2 - \frac{1}{2}(U_{j-1}^n)^2\right] = 0 \ ,$$

which is distinctly different from the difference equation that we had before:

$$U_j^{n+1} = U_j^n - \frac{k}{h} U_j^n \left(U_j^n - U_{j-1}^n\right) \ .$$

The first equation has the form

$$U_j^{n+1} = U_j^n - \frac{k}{h}\left[F(U_j^n) - F(U_{j-1}^n)\right] \ ,$$

hence, it is in conservation law form according to the definition. Applying it to the same initial data as before produces the correct solution with the correct shock speed.

Conservative methods (cont.)

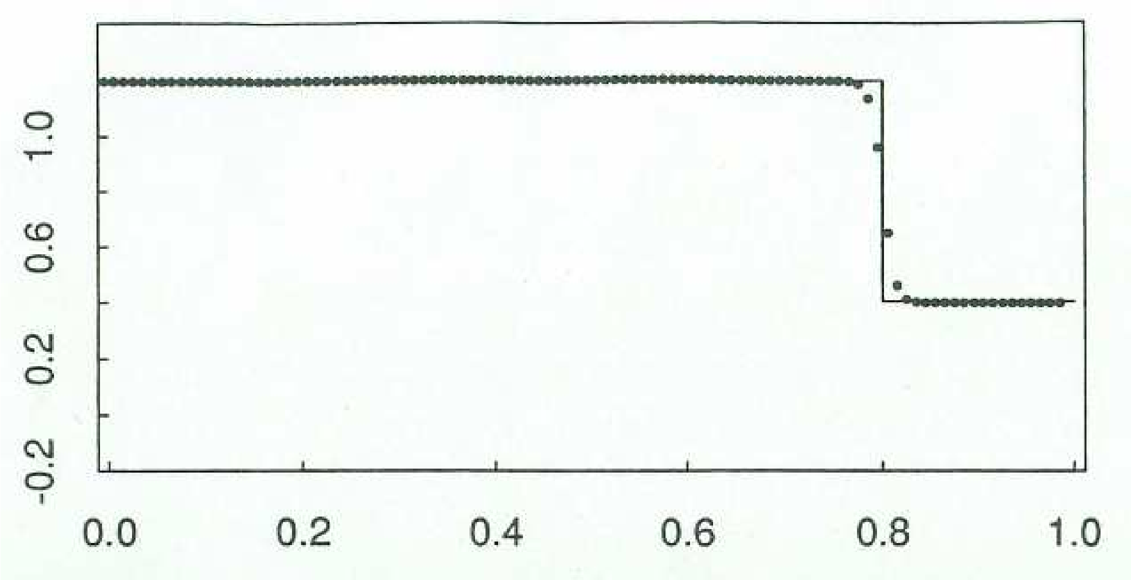

From *R.J. LeVeque (1992)*

True (solid curve) and computed (dotted curve) solution to Burgers' equation with adjacent initial data and using the *conservative upwind scheme*. Note that the *shock speed is correct*.

$$u_0 = \begin{cases} 1.2 & \text{for} \quad x \leq 0 \\ 0.4 & \text{for} \quad x > 0 \end{cases}$$

Def.: A scheme is in *conservation law form* if it has the form

$$U_j^{n+1} = U_j^n - \frac{k}{h}\left[F(U_{j-p}^n, U_{j-p+1}^n, \ldots, U_{j+q}^n)\right.$$
$$\left. - F(U_{j-p-1}^n, U_{j-p}^n, \ldots, U_{j+q-1}^n)\right] \ .$$

F is called the *numerical flux function* .

Lesson: When dealing with shock waves, better use a scheme of conservation law form.

A *scheme in conservation law form*

$$\begin{aligned} U_j^{n+1} &= U_j^n - \frac{k}{h}\left[F(U_{j-p}^n, U_{j-p+1}^n, \ldots, U_{j+q}^n)\right. \\ &\qquad \left. -F(U_{j-p-1}^n, U_{j-p}^n, \ldots, U_{j+q-1}^n)\right] \end{aligned}$$

is *consistent* with the conservative PDE

$$\frac{\partial u}{\partial t} + \frac{\partial}{\partial x}(f(u))$$

if

$$\boxed{\text{F(u,u,...,u) = f(u)}}$$

and there exists a K such that

$$|F(U_{j-p}, \ldots, U_{j+q}) - f(u)| \le K \max_{-p \le i \le q} |U_{j+1} - u| \,.$$

Theorem of Lax and Wendroff (1960)

Consider a sequence of grids, indexed by $l = 1, 2, \ldots$ with mesh parameters $k_l, h_l \to 0$ as $l \to \infty$. Let $U_l(x,t)$ denote the numerical solution computed with a *consistent* and *conservative* method on the lth grid. Suppose that U_l converges* to a function u as $l \to \infty$.

Then $u(x,t)$ is *a weak solution of the conservation law*.

* Convergence in the following sense:

Over every bounded set $\Omega = [a,b] \times [0,T]$

$$\int_0^T \int_a^b |U_l(x,t) - u(x,t)| \mathrm{d}x \, \mathrm{d}t \to 0 \text{ as } l \to \infty$$

and $$\mathrm{TV}(U(\,.\,,t)) < R \quad 0 \le t \le T, l = 1, 2, \ldots$$

where $$\mathrm{TV}(v) = \sup \sum_{j=1}^{N} |v(\xi_j) - v(\xi_{j-1})|$$

Lesson: C^3: Conservation and consistency leads to convergence. Theorem of Lax and Wendroff (1960).

§ 3 Conservation laws – finite volumes

Consider the continuity equation:

$$\rho_t + \nabla \cdot (\rho \mathbf{u}) = 0 \ . \tag{1}$$

Integration over a finite volume, $\mathcal{V}$, and time period, T, leads to the *integral form* of this equation:

$$\int_{\mathcal{V}} \rho(T, \mathbf{x}) \mathrm{d}V - \int_{\mathcal{V}} \rho(0, \mathbf{x}) \mathrm{d}V = - \int_0^T \oint_{\partial \mathcal{V}} (\rho \mathbf{u}) \cdot \mathbf{n} \, \mathrm{d}s \, \mathrm{d}t \tag{2}$$

Solutions to Eq. (2) are called *weak solutions* to the partial differential equation, Eq. (1). Additionally to the solutions of Eq. (1), the set of solutions to Eq. (2) encompasses discontinuous solutions, because no derivatives appear in Eq. (2). Discontinuous solutions to the Euler equations represent *shock fronts* of the real world.

Consider the mass conservation in a one-dimensional finite tube element:

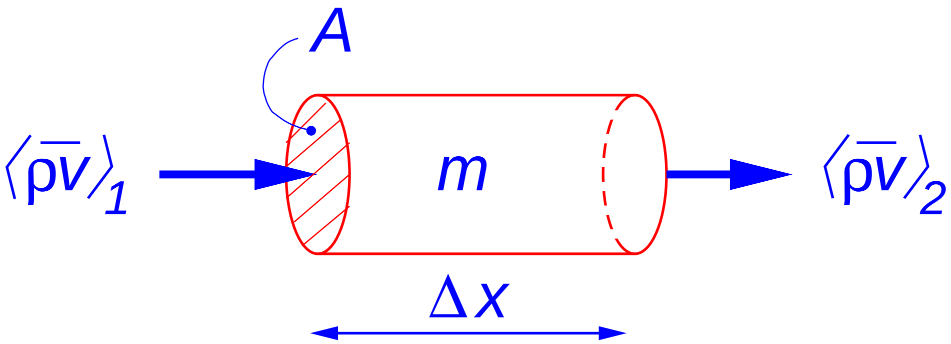

$$m(t+\Delta t) = m(t) + \langle\overline{\rho v}\rangle_1 A\Delta t - \langle\overline{\rho v}\rangle_2 A\Delta t \tag{3}$$

$$\langle\rho\rangle(t+\Delta t) = \langle\rho\rangle(t) - \frac{\Delta t}{\Delta x}\left(\langle\overline{\rho v}\rangle_2 - \langle\overline{\rho v}\rangle_1\right) \tag{4}$$

Eq. (4) has the form of a *conservative finite volume scheme*.

in the limit of $\Delta x \to 0$ and $\Delta t \to 0$ $\quad \dfrac{\partial \rho}{\partial t} = \dfrac{\partial(\rho v)}{\partial x}$

But Eq. (3) is *identical to the integral form* Eq. (2):

$$\int_{\mathcal{V}} \rho(T,\mathbf{x})\mathrm{d}V - \int_{\mathcal{V}} \rho(0,\mathbf{x})\mathrm{d}V = -\int_0^T \oint_{\partial\mathcal{V}} (\rho\mathbf{u})\cdot\mathbf{n}\,\mathrm{d}s\,\mathrm{d}t$$

Conservation laws – finite volumes (cont.)

The conservative, finite volume formulation has three highly desirable properties:

- Conserved quantities (mass, momentum, energy) remain accurately conserved
- Discontinuous solutions are include by solving the integral form of the partial differential equation
- It fulfills one of two requirements of the theorem of Lax and Wendroff (1960) that says:

  The approximate solution that is computed with a *consistent* and *conservative* scheme *converges* to a weak solution of the conservation law.

Conservation laws – finite volumes (cont.)

Euler's equation in one dimension is given by

$$\mathbf{q}_t + \mathbf{f}(\mathbf{q})_x = 0 \ , \qquad \mathbf{q}_i^{n+1} = \mathbf{q}_i^n + \frac{\Delta t}{\Delta x}[\mathbf{f}_{i-1/2} - \mathbf{f}_{i+1/2}] \ ,$$

where

$$\mathbf{q} = \begin{pmatrix} \rho \\ \rho u \\ E \end{pmatrix} \qquad \mathbf{f}(\mathbf{q}) = \begin{pmatrix} \rho u \\ \rho u^2 + p \\ u(E+p) \end{pmatrix}$$

In 3-D we have

$$\mathbf{q}_t + \mathbf{f}(\mathbf{q})_x + \mathbf{g}(\mathbf{q})_y + \mathbf{h}(\mathbf{q})_z = 0 \ ,$$

with

$$\mathbf{q} = \begin{pmatrix} \rho \\ \rho u \\ \rho v \\ \rho w \\ E \end{pmatrix} \qquad \mathbf{f}(\mathbf{q}) = \begin{pmatrix} \rho u \\ \rho u^2 + p \\ \rho u v \\ \rho u w \\ u(E+p) \end{pmatrix} \qquad \cdots$$

§ 4 Riemann solvers

A conservative finite volume scheme is an exact representation of the integral form of the partial differential equation describing the conservation law. The problem consists in computing the correct flux function $\mathbf{f}(\mathbf{q})$, i.e., $\langle\overline{\rho v}\rangle$ in the case of the continuity equation.

It turns out that these fluxes can be computed *exactly*.

Idea of S.K. Godunov (1959): Piecewise constant reconstruction with discontinuities at cell interfaces

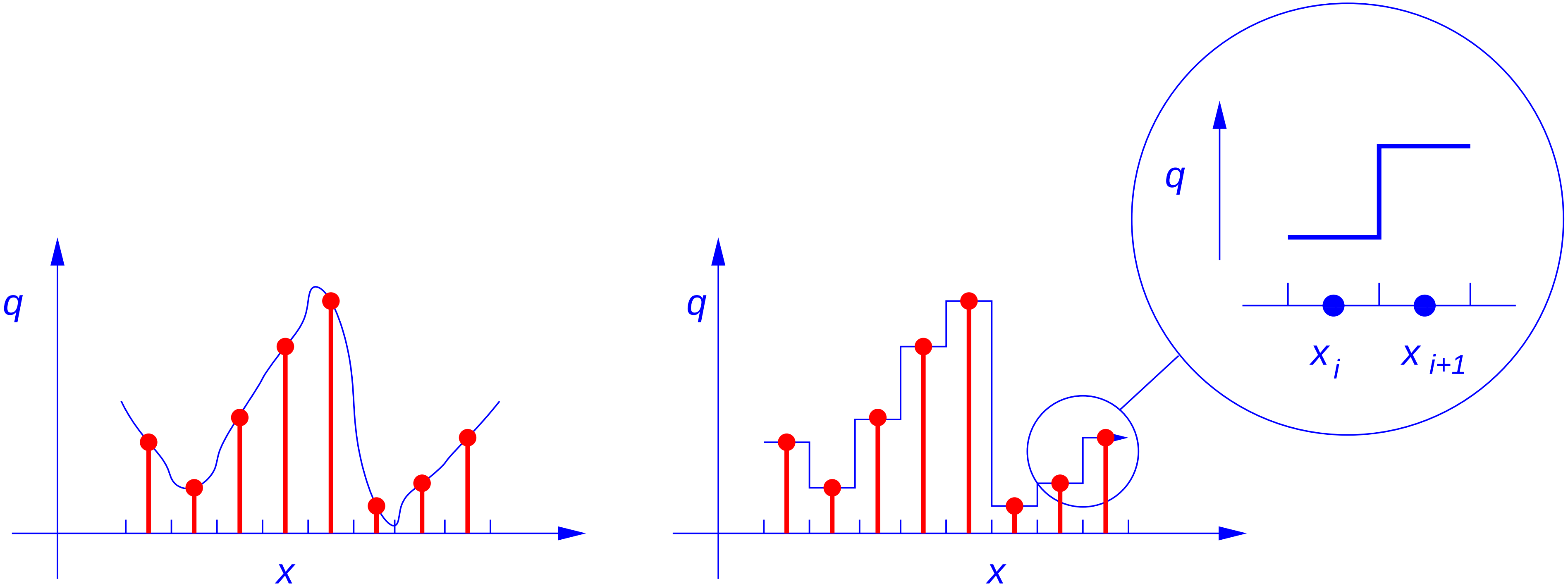

The shock-tube problem

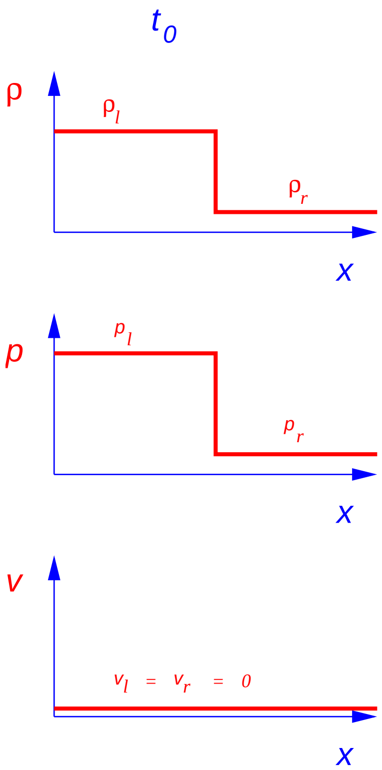

The shock-tube problem

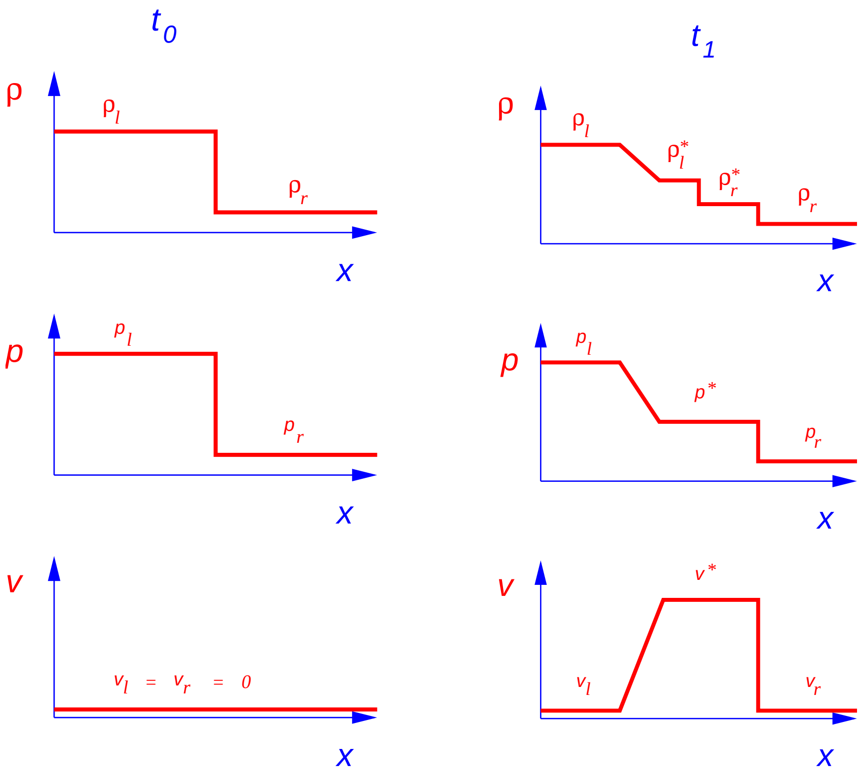

Riemann solvers (cont.)

The shock-tube problem

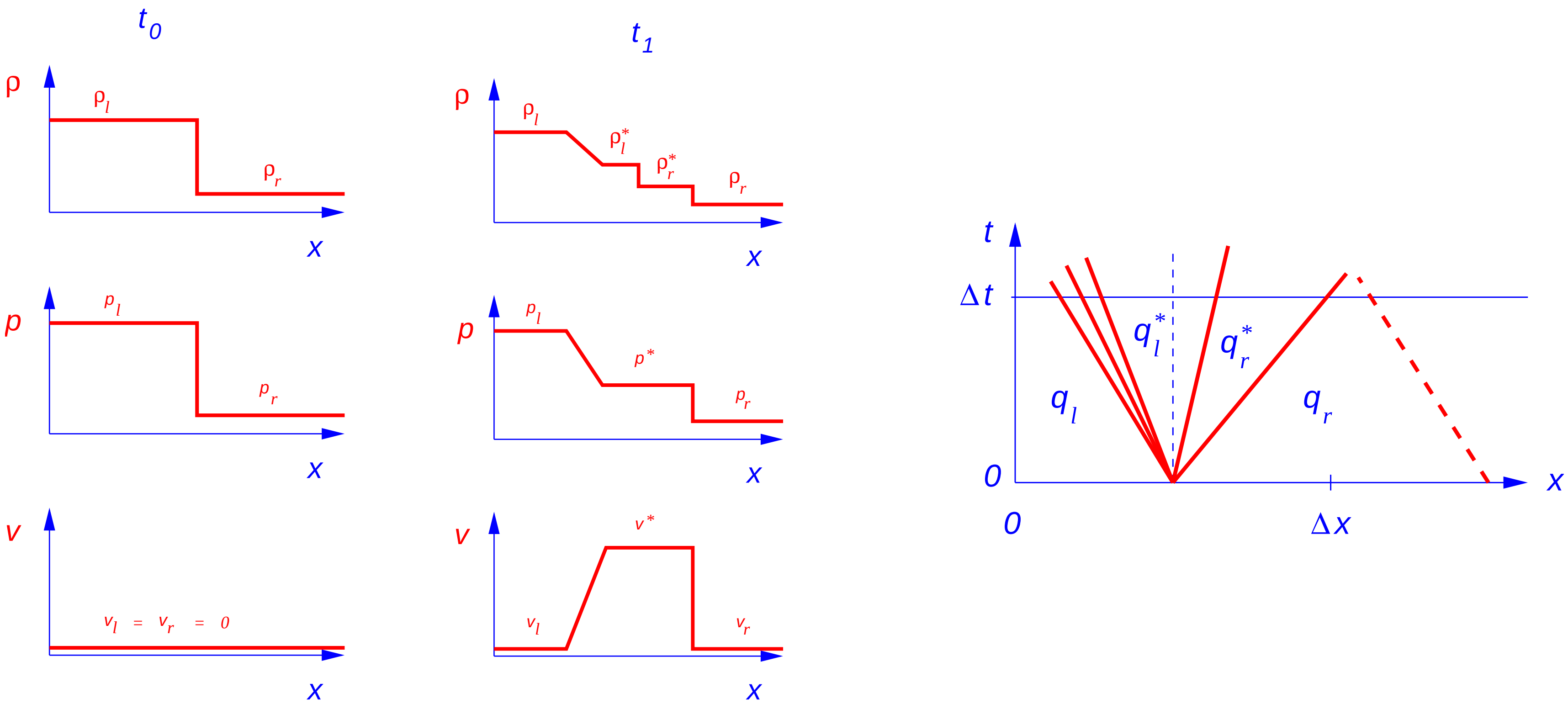

Riemann solvers (cont.)

The shock-tube problem

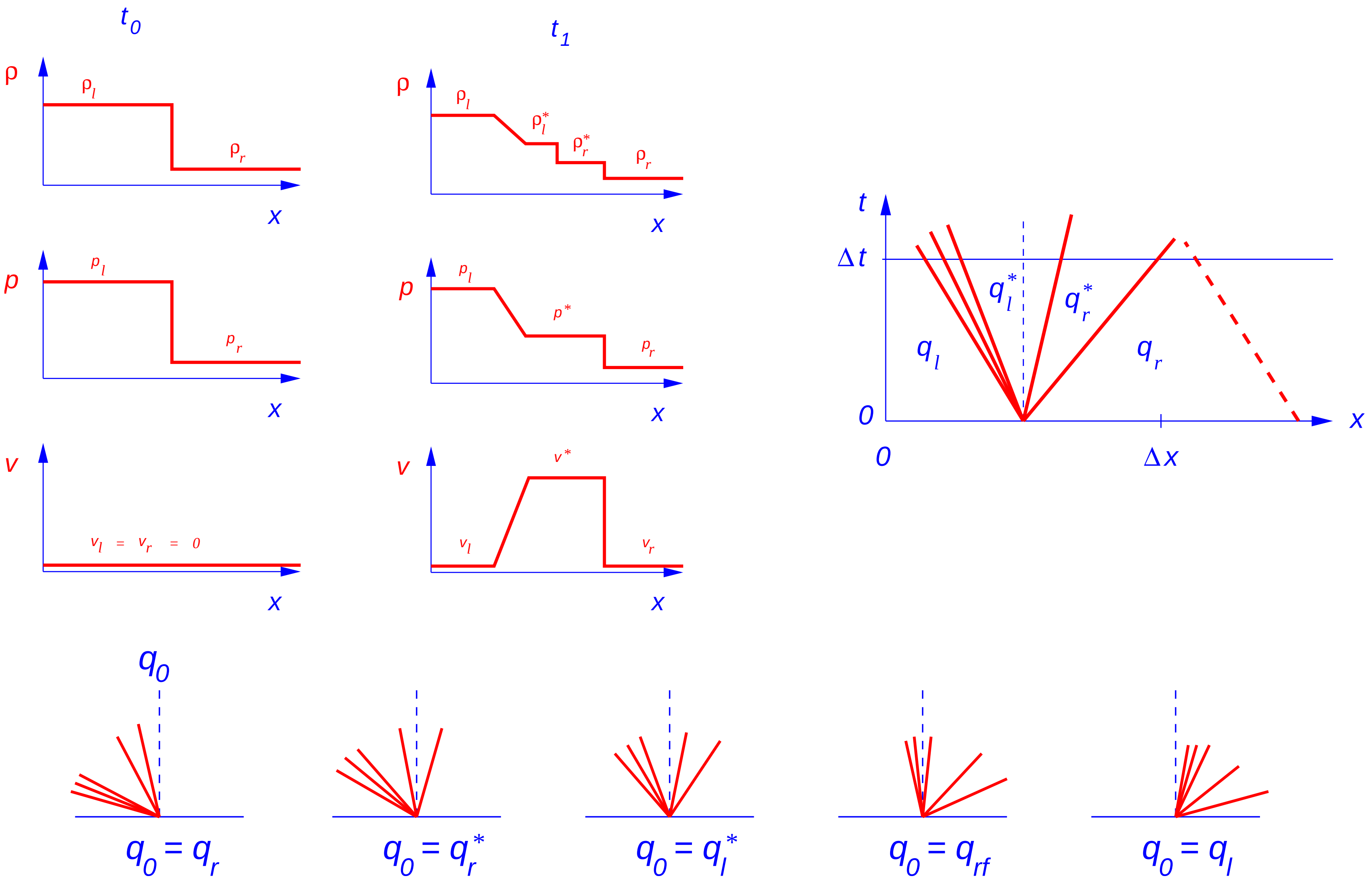

§ 5 Explicit vs implicit and the CFL condition

Let's go back to the *linear advection equation*

$$\boxed{\frac{\partial \rho}{\partial t} + \frac{\partial (u\rho)}{\partial x} = 0}$$

with constant velocity u. The straightforward *upwind differentiation* is

$$\frac{\rho_j^{n+1} - \rho_j^n}{k} + \frac{u\rho_j^n - u\rho_{j-1}^n}{h} = 0 \, ,$$

where $k = \Delta t$ and $h = \Delta x$. Next, we keep ρ at the new time step, $n+1$ on the left hand side and express it in terms of the known densities at the old time step n:

$$\rho_j^{n+1} = \rho_j^n - \frac{k}{h} u \left(\rho_j^n - \rho_{j-1}^n \right) \, .$$

This is called an *explicit scheme*.

For an explicit scheme, the time step k is restricted by the *CFL-condition (Courant-Friedrichs-Lewy)*

$$\boxed{C = \frac{uk}{h} < 1}$$

Typically, u is the speed of sound, or the Alfvén speed, which both may become very large, hence, the time step k must be very small, which drastically increases the computation costs.

Explicit vs implicit and the CFL condition (cont.)

A way around the CFL bottleneck provides the *implicit scheme*. We still use the upwind differentiation but now in terms of the quantities at the new time step $n+1$:

$$\frac{\rho_j^{n+1} - \rho_j^n}{k} + \frac{u\rho_j^{n+1} - u\rho_{j-1}^{n+1}}{h} = 0 \, ,$$

Keeping all quantities at time $n+1$ on the left hand side, we obtain

$$\rho_j^{n+1} - \frac{k}{h} u\rho_{j-1}^{n+1} + \frac{k}{h} u\rho_j^{n+1} = \rho_j^n \, , \quad \Longrightarrow \quad \rho_j^{n+1}(1+C) - C\rho_{j-1}^{n+1} = \rho_j^n \, ,$$

which leads to the algebraic system of equations

$$\begin{pmatrix} (C+1) & 0 & 0 & \cdots & 0 & 0 & -C \\ -C & (1+C) & 0 & \cdots & 0 & 0 & 0 \\ 0 & -C & (1+C) & \cdots & 0 & 0 & 0 \\ \vdots & \vdots & \vdots & \ddots & \vdots & \vdots & \vdots \\ 0 & 0 & 0 & \cdots & 0 & -C & (1+C) \end{pmatrix} \begin{pmatrix} \rho_1^{n+1} \\ \rho_2^{n+1} \\ \rho_3^{n+1} \\ \vdots \\ \rho_N^{n+1} \end{pmatrix} = \begin{pmatrix} \rho_1^n \\ \rho_2^n \\ \rho_3^n \\ \vdots \\ \rho_N^n \end{pmatrix},$$

Typically, an implicit scheme is not subject to the CFL restriction. However, the time step should not be arbitrarily large to avoid large discretization (dispersion) errors.

References

Lax P.D. and Wendroff, B.: 1960, *Systems of conservation laws*, Comm. Pure Appl. Math., 13, 217-237.

Laney, C.B.: 1998, *Computational Gasdynamics*, Cambridge University Press, Cambridge

LeVeque, R.J.: 2002, *Finite Volume Methods for Hyperbolic Problems*, Cambridge University Press, Cambridge

LeVeque, R.J.: 1992, *Numerical Methods for Conservation Laws*, Birkhäuser Verlag, Basel

LeVeque, R.J., Mihalas, D., Dorfi, E.A., and Müller, E.: 1998, *Computational Methods for Astrophysical Fluid Flow*, O. Steiner & A. Gautschy (eds.), Springer-Verlag, Berlin

Oran E.S. and Boris, J.P.: 2001, *Numerical Simulation of Reactive Flow*, Cambridge University Press, 2nd ed.

Toro, E.F.: 1999, *Riemann Solvers and Numerical Methods for Fluid Dynamics*, Springer-Verlag, Berlin

Part II: Aspects of computational astrophysics

§ 6 The role of computer simulations in astrophysics

Historical Perspective:

- 1950's and 1960's: Stellar evolution calculations (Martin Schwarzshild in the U.S. and Rudolph Kippenhahn in Göttingen, Germany). At that time *computers were viewed as tools for the numerical integration* rather than as a tool for experimentation.

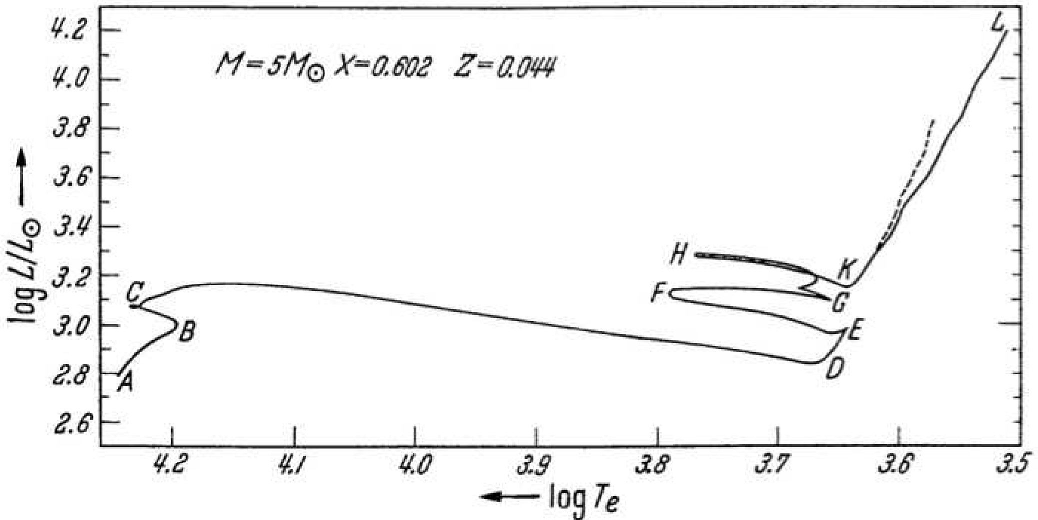

Evolution of a 5 $M_\odot$ star in the HRD

Kippenhahn et al. (1965, Zeitschrift für Astrophysik)

Rudolph Kippenhahn

The role of computer simulations in astrophysics (cont.)

- 1960's: N-body stellar dynamics simulations (e.g. tidal interaction of galaxies) and hydrodynamical systems (e.g. core collapse supernovae). Notion of *computational astrophysics as experimental astronomy*.

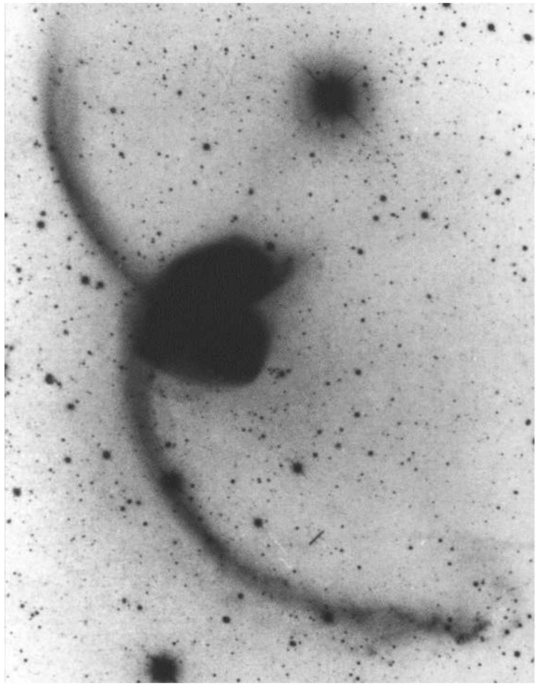

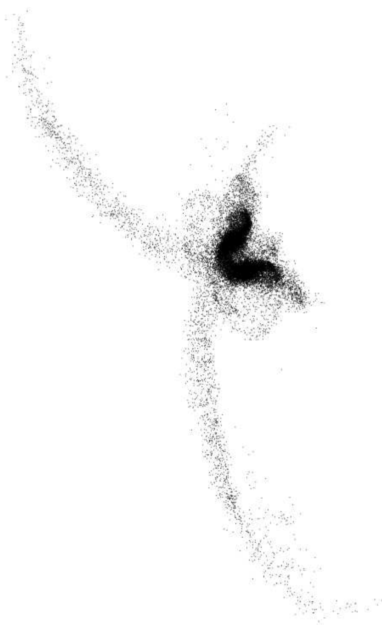

The antenna nebula NGC 4038/4039 evolved from a collision of two similarly sized spiral galaxies. *Left:* Observed present state. *Right:* Present state from a computer simulation of the complete collision (www.ifa.hawaii.edu/˜barnes).

These simulations are generally *motivated by the question "What happens if?"* more so than "What is the solution to these equations?".

Computational astrophysics is the experimentation with astrophysical objects in a virtual (numerical) laboratory, comparable to the manipulation with real probes in classical physics experiments.

The role of computer simulations in astrophysics (cont.)

Role of Computational astrophysics:

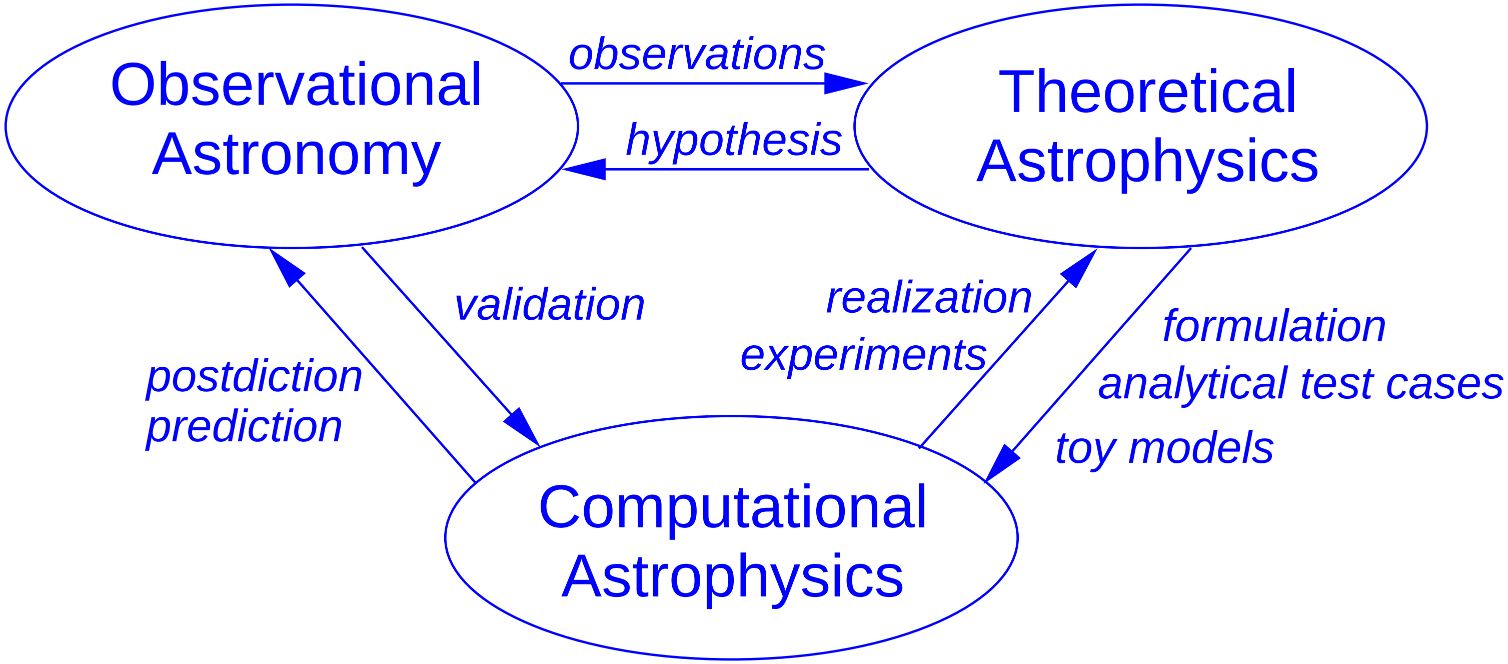

Adapted from *M. Norman (1997)*

The role of computer simulations in astrophysics (cont.)

Simulations tend to model a *time dependent* physical system with some degree of *realism*. Usually, simulated systems have no simple closed form analytic solutions. Otherwise, one rather talks of *modeling*.

Realistic simulations produce observable quantities like intensity maps or polarimetric maps that look like corresponding actual observations, so called *virtual or synthetic observations*. Typically, a realistic solar simulation uses a *realistic equation of state* that takes ionization and the composition of the solar plasma into account and it carries out *radiation transfer with actual opacities* as occurring in the solar plasma.

Progress in computational astrophysics:

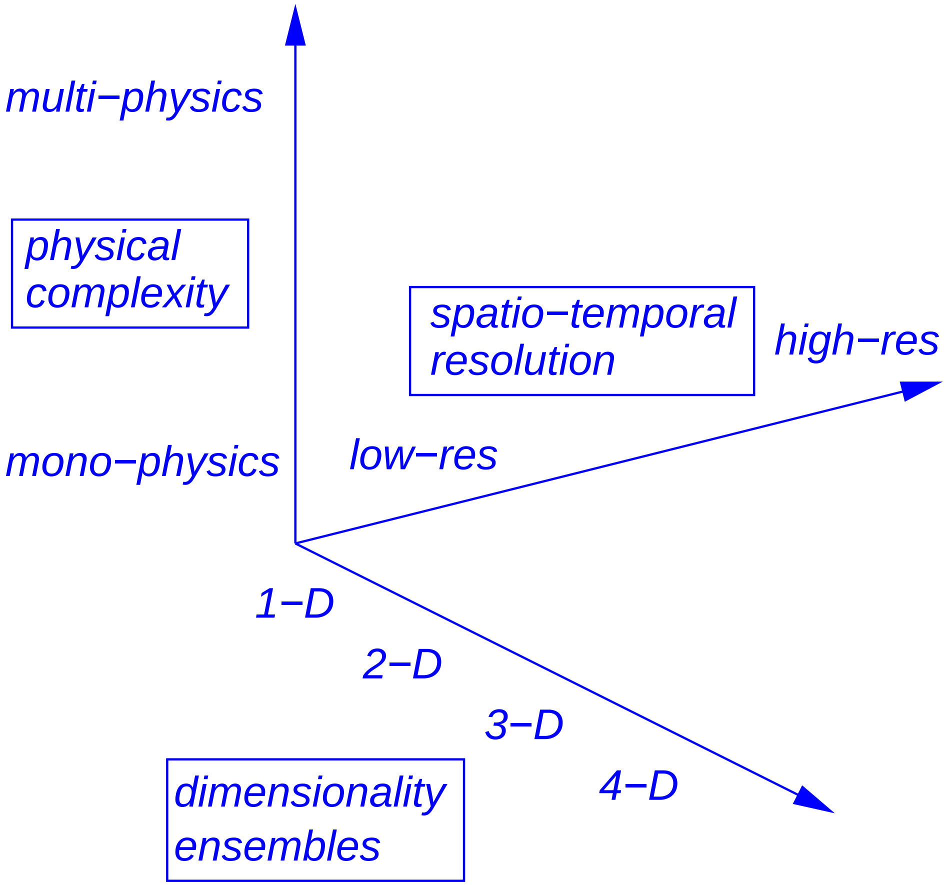

Adapted from *M. Norman (1997)*

References

Kippenhahn, R., Thomas, H.-C., and Weigert, A.: 1965, *Sternetnwicklung IV. Zentrales Wasserstoff- und Heliumbrennen bei einem Stern von 5 Sonnenmassen*, Zeitschrift für Astrophysik 61, 241-267

Kippenhahn, R.: 2008, *Als die Computer die Astronomie eroberten*, Reviews in Modern Astronomy 20, 1-14

Norman, M.: 1997, *Computational Astrophysics: The "New Astronomy" for the 21st Century*, in ASP Conf. Series Vol. 123, D.A. Clarke & M.J. West (eds.), p. 3-14

Ostriker, J.P.: 2000, *Historical Reflection on the Role of Numerical Modeling in Astrophysics*, Reviews in Modern Astronomy 13, 1-11

Part III: Concrete implementations

§ 7 Computer Codes

The following is a non-exhaustive, arbitrarily selected list of codes that may or may not be suitable for serving your needs. Details are without guarantee.

acronym	AMR-VAC		
name	Versatile Advection Code	PENCIL	NIRVANA
web page	http://amrvac.org/doc-contents.html	http://www.nordita.org/software/pencil-code/	http://nirvana-code.aip.de/
principal authors	Gábor Tóth / Ronny Keppens	Axel Brandenburg / Wolfgang Dobler	Udo Ziegler
language	dimension independent notation, (convertible to FORTRAN via VAC Preprocessor)	FORTRAN	C
MHD	yes	yes	yes
radiative transfer	no	yes	no
parallelization	HPF, MPI, OpenMP	MPI	MPI
grid	structured grid; adaptive/AMR	Cartesian; adaptive/static	Cartesina; cylidrical; spherical; adaptive/AMR
comments:	The code features a variety of numerical methods for the advection step including TVD schemes and Riemann solvers; AMR-VAC is a version of VAC with automatic adaptive mesh refinement, AMR.	Code uses a high-order fnite-difference scheme; primarily designed to deal with weakly compressible turbulent flows.	Godunov-type central scheme; piecewise linear TVD reconstruction; flux-CT scheme; dual energy formalism.
References:	—	https://arxiv.org/abs/astro-ph/0111569	https://www.sciencedirect.com/science/article/pii/S0021999110005784?via%3Dihub

Computer Codes (cont.)

acronym	CO^5BOLD	MURaM	
name	Conservative Code for the Computation of Compressible Convection in a Box of L Dimensions	MPS/University of Chicago Radiative MHD	Bifrost
web page	http://www.astro.uu.se/~bf/co5bold_main.html	https://www2.mps.mpg.de/projects/solar-mhd/muram_site/index.html	—
principal author	Bernd Freytag	Alexander Vögler / Matthias Rempel	Mats Carlsson & Boris Gudiksen
language	FORTRAN	—	C
MHD	yes	yes	yes
radiative transfer	yes/non-grey	yes/non-grey	yes/non-grey
parallelization	OpenMP	MPI	MPI
grid	Cartesian; adaptive/static	Cartesian; adaptive/static	Cartesian, adaptive/static
comments:	Riemann solver based code; realistic EOS and opacities; chemical reaction network; dynamic hydrogen ionization.	Fourth-order accurate; explicit finite differences TVD scheme; realistic EOS and opacities; includes coronal physics	Staggered grid with 6th order differential operators. Realistic EOS and opacities; Spitzer heat conduction; dynamic H and He ionization, specialized to incl, chromosphere & corona.
References:	https://arxiv.org/abs/1110.6844	https://www.aanda.org/articles/aa/pdf/2005/01/aa1507.pdf	https://arxiv.org/abs/1105.6306

acronym	Mancha	ANTARES	CLAWPACK
name	Multi-physics, Advanced, Non-ideal Code for High-resolution simulations of the solar Atmosphere	A Numerical Tool for Astrophysical REsearch	Conservation Law Package
web page	http://www.iac.es/proyecto/PI2FA/pages/codes.php	—	http://www.amath.washington.edu/ claw/
principal author	Elena Khomenko	H.J. Muthsam	Randall J. LeVeque
language	FORTRAN	FORTRAN	FORTRAN
MHD	yes	yes	yes
radiative transfer	yes	yes/non-gray	no
parallelization	MPI	MPI; OpenMP	MPI
grid	Cartesian; AMR	Cartesian; spherical; AMR/static	adaptive/AMR
comments:	4th order central differences; realistic EOS.	Features various high-resolution schemes	Features various solvers incl. Riemann solvers; solves problems on curved manifolds
References:	https://arxiv.org/abs/1006.2998	http://arxiv.org/abs/0905.0177	https://peerj.com/articles/cs-68/

Computer Codes (cont.)

acronym			
name	ZEUS-MP/2	Enzo	FLASH
web page	http://ascl.net/1102.028	https://enzo-project.org	http://flash.uchicago.edu/website/home/
principal author	Stone & Norman	Michael Norman and Enzo community	Alliances Center for Astrophysical Thermonuclear Flashes
language	FORTRAN	—	FORTRAN
MHD	yes	yes	yes
radiative transfer	no	yes	no
parallelization	MPI	yes	MPI
grid	Cartesian, spherical; cylindricalAMR/static	Cartesian, AMR	Cartesian, spherical, cylindrical polar; AMR
comments:		grid-based hybrid code (hydro + N-Body), designed to simulate cosmological structure formation; Enzo branched off from ZEUS	HD: split PPM, unsplit MUSCL-Hancock; MHD: split 8-wave solver, unsplit staggered mesh; split relativistic hydro solver; reactive gas dynamics
References:	http://adsabs.harvard.edu/abs/2006ApJS..165..188H	—	https://iopscience.iop.org/article/10.1086/317361/pdf

acronym		
name	ATHENA++	RAMSES
web page	https://princetonuniversity.github.io/athena/	https://www.ics.uzh.ch/ teyssier/ramses/RAMSES.html
principal author	James M. Stone	Romain Teyssier
language	C++	FORTRAN
MHD	yes/relativistic	yes
radiative transfer	—	no
parallelization	MPI/OpenMP; task-based execution	MPI
grid	Cartesian, cylindrical; spherical-polar; Various general-relativistic coordinates; AMR	Cartesian, tree-based AMR
comments:	special and general relativistic hydrodynamics and MHD.	Self-gravitating magneto fluid dynamics
References:	https://arxiv.org/abs/1711.07439	https://arxiv.org/abs/astro-ph/0111367

Example CO^{5}BOLD

CO^{5}BOLD is designed for simulating *hydrodynamics* and *radiative transfer* in the outer and inner layers of stars. Additionally, it can treat *magnetohydrodynamics*, non-equilibrium *chemical reaction networks*, dynamic *hydrogen ionization*, and *dust formation* in stellar atmospheres.

Box in a star

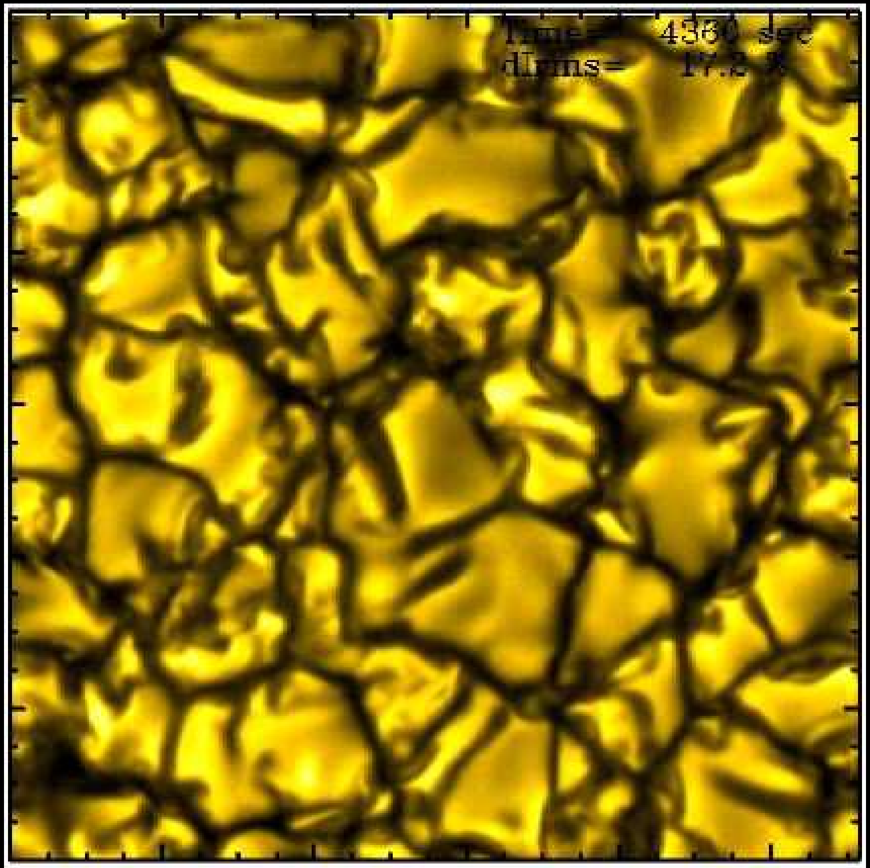

Simulation of *solar granulation with CO^{5}BOLD*.
$400 \times 400 \times 165$ grid cells, 11.2×11.2 Mm,
Contrast at $\lambda \approx 620$ nm is 16.65%.
Courtesy *M. Steffen*, AIP Potsdam

Star in a box

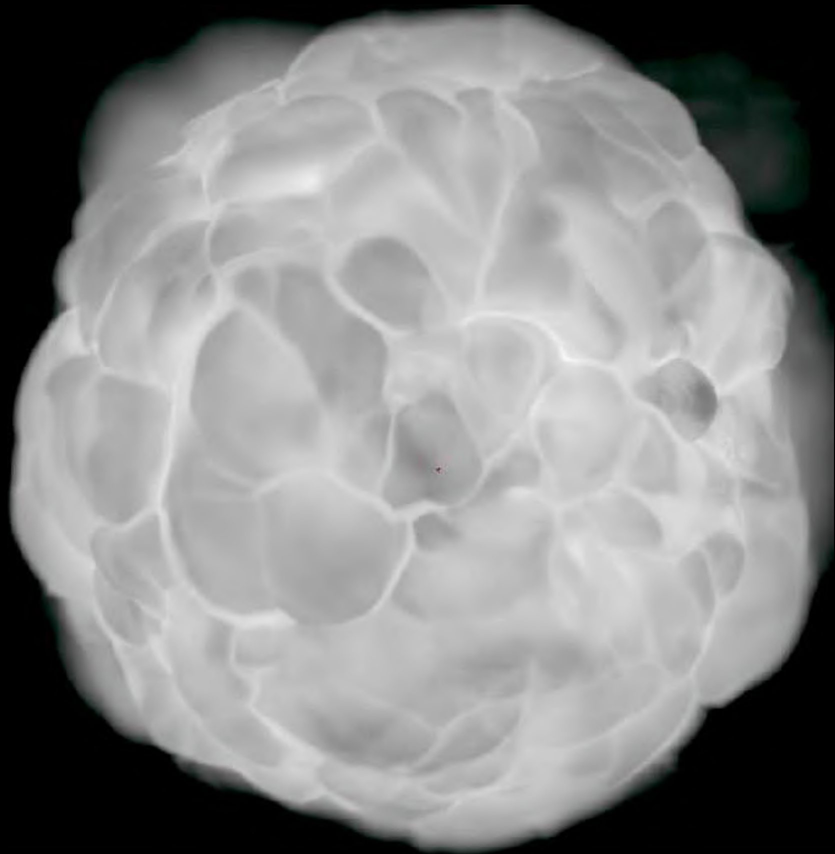

Simulation of a *Betelgeusew with CO^{5}BOLD*.
235^3 grid cells, $m_{\rm star} = 12 m_\odot$,
$T_{\rm eff} = 3436$ K, $R_{\rm star} = 875 R_\odot$
Courtesy *Bernd Freytag*, Uppsala

Computer Codes (cont.)

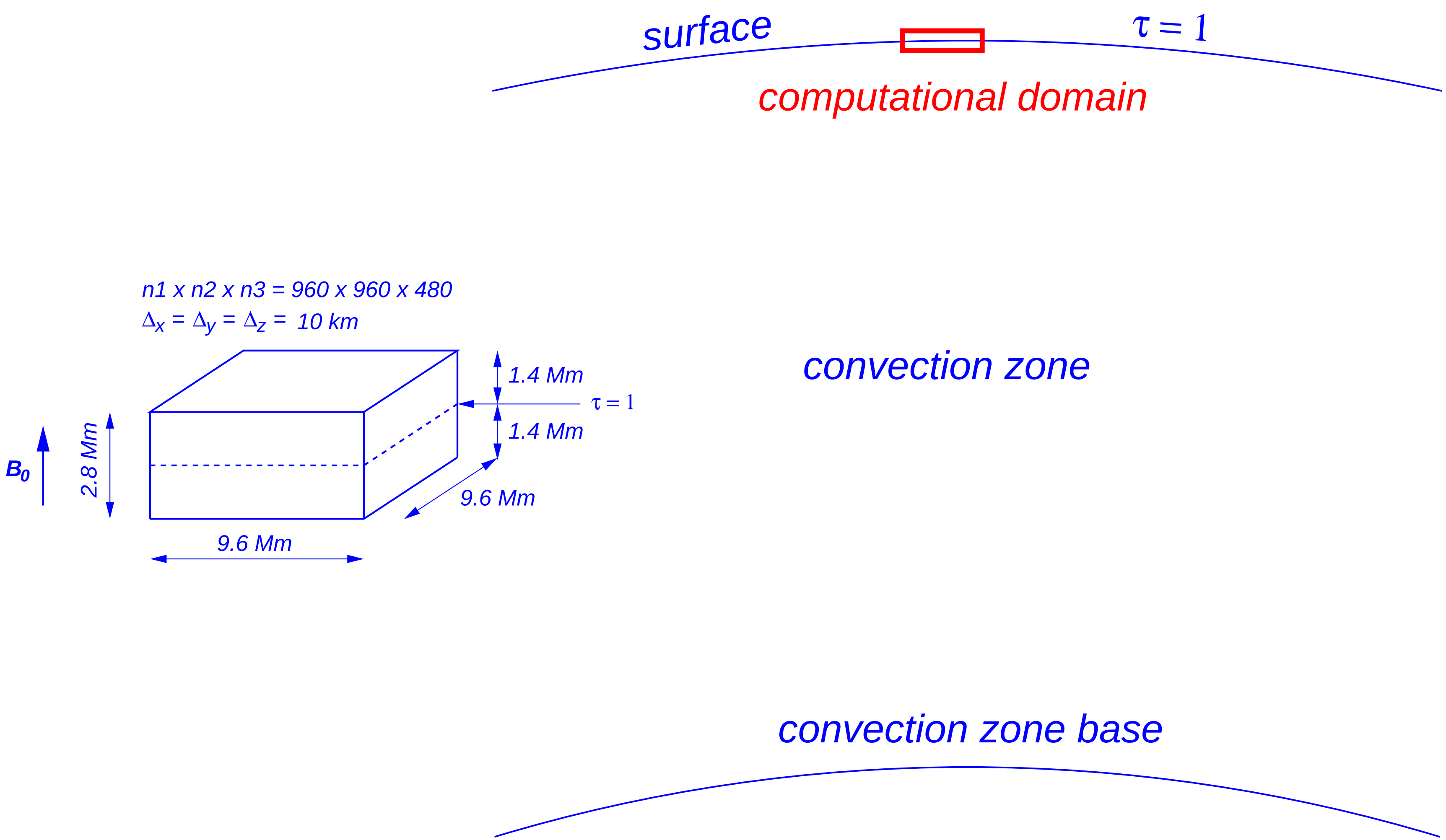

Size of a typical three-dimensional computational domain (left) in comparison with the size of the Sun (right).

Computer Codes (cont.)

Bolometric intensity maps

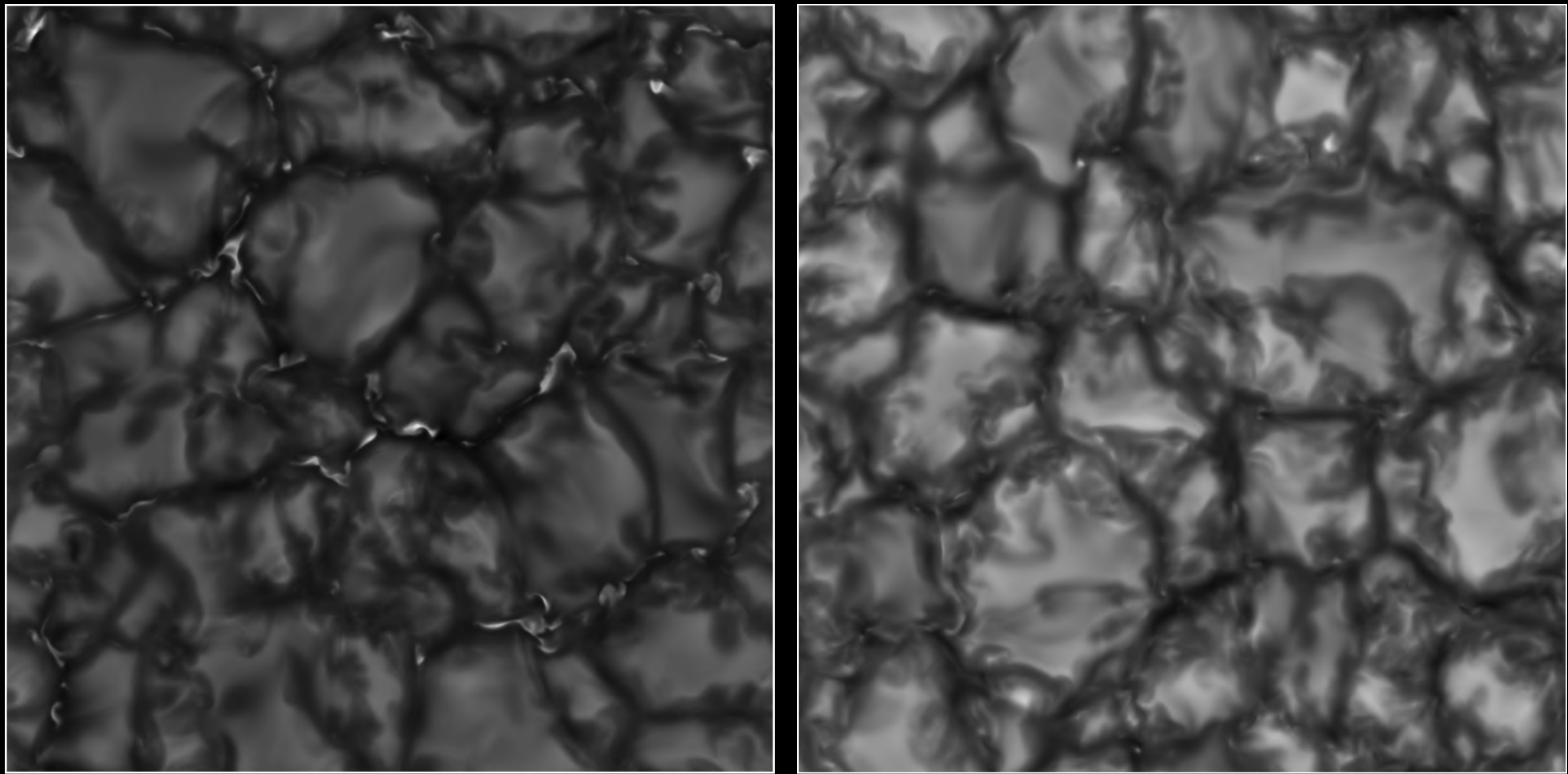

Computations: *Centro Svizzero di Calcolo Scientifico*

With magnetic fields:
Magnetohydrodynamic simulation.

Without magnetic fields:
Hydrodynamic simulation

Courtesy,
F. Calvo.

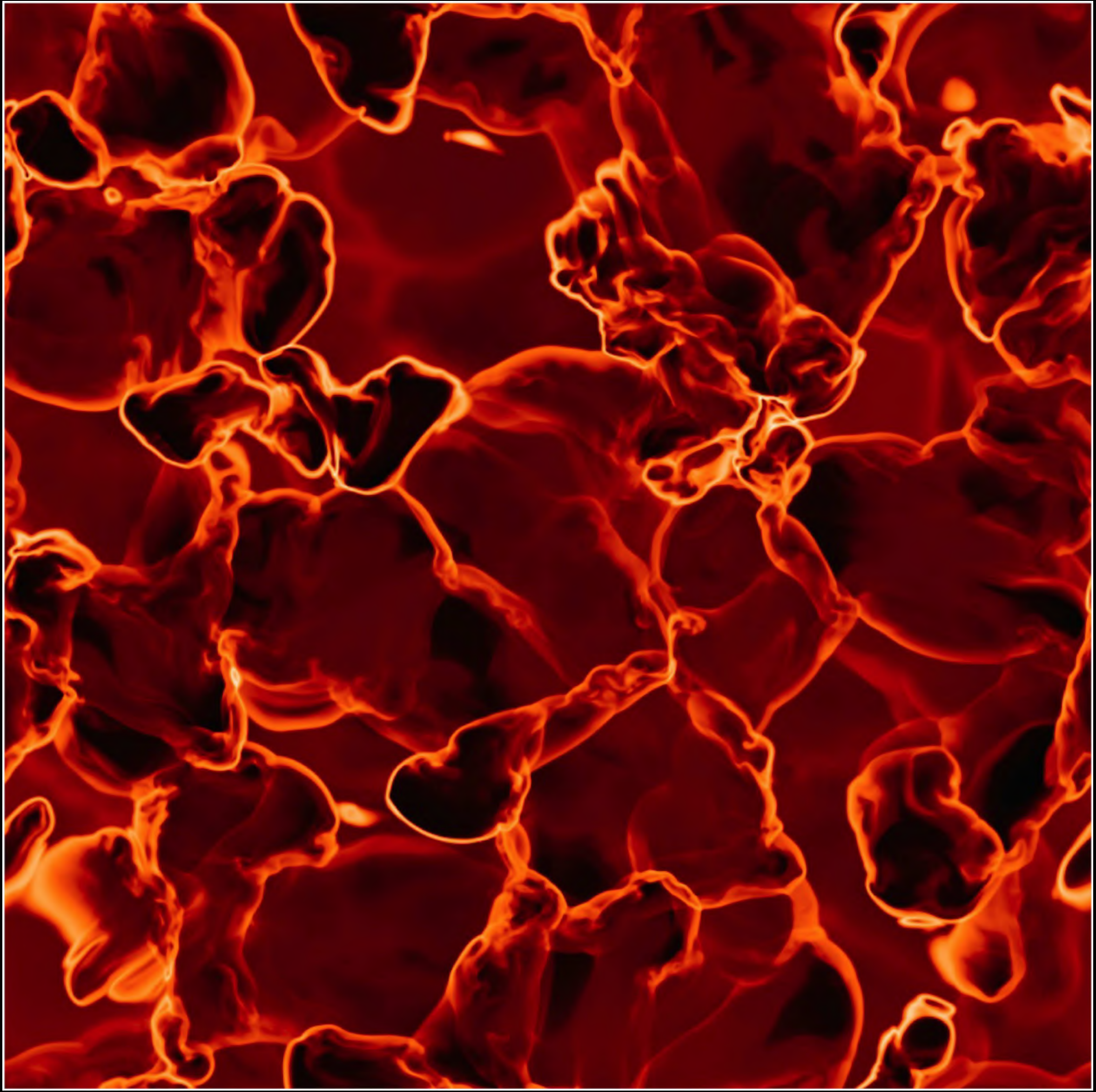

Horizontal cross-section through the chromosphere of a magnetic field-free simulation. Colors show temperature. *Shock fronts and temperature spikes* are ubiquitous.

§ 8 Equations and boundary conditions

Starting point are the *equations of magnetohydrodynamics*:

$$
\begin{aligned}
\frac{\partial \rho}{\partial t} &+ \nabla \cdot (\rho \mathbf{v}) && = 0 \ , \\
\frac{\partial \rho \mathbf{v}}{\partial t} &+ \nabla \cdot \left(\rho \mathbf{v}\mathbf{v} + \left(P + \frac{\mathbf{B}\cdot\mathbf{B}}{2} \right) \mathbf{I} - \mathbf{B}\mathbf{B} \right) && = \rho \mathbf{g} \ , \\
\frac{\partial \mathbf{B}}{\partial t} &+ \nabla \cdot (\mathbf{v}\mathbf{B} - \mathbf{B}\mathbf{v}) && = 0 \ , \\
\frac{\partial E}{\partial t} &+ \nabla \cdot \left(\left(E + P + \frac{\mathbf{B}\cdot\mathbf{B}}{8\pi} \right) \mathbf{v} - \tfrac{1}{4\pi} (\mathbf{v}\cdot\mathbf{B})\,\mathbf{B} + \mathbf{F}_{\mathrm{rad}} \right) && = \rho \boldsymbol{g} \cdot \boldsymbol{v} \ .
\end{aligned}
$$

ρ: mass density; $\mathbf{v}$: velocity; P: gas pressure; $\mathbf{B}$: magnetic field; $\mathbf{g}$ gravitational acceleration; E: total energy density; $\mathbf{F}_{\mathrm{rad}}$: radiative flux; t: time

$$E = \rho e_{\mathrm{int}} + e_{\mathrm{kin}} + e_{\mathrm{mag}} = \rho e_{\mathrm{int}} + \rho \frac{\mathbf{v}\cdot\mathbf{v}}{2} + \frac{\mathbf{B}\cdot\mathbf{B}}{2}$$

Equations and boundary conditions (cont.)

The equations of ideal magnetohydrodynamics in *conservation law form*:

$$\boxed{\frac{\partial \boldsymbol{U}}{\partial t} + \boldsymbol{\nabla} \cdot \boldsymbol{\mathcal{F}} = \boldsymbol{S}\,,}$$

where the *vector of conserved variables* $\boldsymbol{U}$, the *source term* $\boldsymbol{S}$ due to gravity and radiation, and the *flux tensor* $\boldsymbol{\mathcal{F}}$ are

$$\boldsymbol{U} = (\rho, \rho\boldsymbol{v}, \boldsymbol{B}, E)\ , \qquad \boldsymbol{S} = (0, \rho\boldsymbol{g}, 0, \rho\boldsymbol{g}\cdot\boldsymbol{v} + q_{\rm rad})\ ,$$

$$\boldsymbol{\mathcal{F}} = \begin{pmatrix} \rho\boldsymbol{v} \\ \rho\boldsymbol{v}\boldsymbol{v} + \left(p + \dfrac{\boldsymbol{B}\cdot\boldsymbol{B}}{8\pi}\right)\boldsymbol{I} - \dfrac{\boldsymbol{B}\boldsymbol{B}}{4\pi} \\ \boldsymbol{v}\boldsymbol{B} - \boldsymbol{B}\boldsymbol{v} \\ \left(E + p + \dfrac{\boldsymbol{B}\cdot\boldsymbol{B}}{8\pi}\right)\boldsymbol{v} - \frac{1}{4\pi}\left(\boldsymbol{v}\cdot\boldsymbol{B}\right)\boldsymbol{B} \end{pmatrix} .$$

Equations and boundary conditions (cont.)

The MHD equations must be closed by an *equation of state* which gives the gas pressure as a function of the density and the thermal energy per unit mass $e_{\mathrm{int}} = \epsilon$

$$p = p(\rho, \epsilon)\,,$$

usually available to the program in *tabulated* form.

In the most simplest case of a polytropic ideal gas $\epsilon = \dfrac{P}{(\gamma-1)\rho}$, where $\gamma = \mathrm{const.}$

For the numerical treatment, $\dfrac{\partial \boldsymbol{U}}{\partial t} + \boldsymbol{\nabla}\cdot\boldsymbol{\mathcal{F}} = \boldsymbol{S}$ is usaully solved in two steps:

(1) $t \to t + \Delta t$: $\boxed{\dfrac{\partial \boldsymbol{U}}{\partial t} + \boldsymbol{\nabla}\cdot\boldsymbol{\mathcal{F}} = 0}$ (2) $t \to t + \Delta t$ $\boxed{\dfrac{\partial \boldsymbol{U}}{\partial t} = \boldsymbol{S}}$

This procedure is called *operator splitting*.

In practice it is not the ideal MHD-equations that are solved but rather some kind of a viscous and resistive form of the equations with flux tensor

$$\boldsymbol{\mathcal{F}} = \left(\begin{array}{c} \rho\boldsymbol{v} \\ \rho\boldsymbol{v}\boldsymbol{v} + \left(p + \dfrac{\boldsymbol{B}\cdot\boldsymbol{B}}{8\pi}\right)\boldsymbol{I} - \dfrac{\boldsymbol{B}\boldsymbol{B}}{4\pi} - \boldsymbol{\sigma} \\ \boldsymbol{B}\boldsymbol{v} - \boldsymbol{v}\boldsymbol{B} - \eta[\nabla\boldsymbol{B} + (\nabla\boldsymbol{B})^T] \\ \left(E + p + \dfrac{\boldsymbol{B}\cdot\boldsymbol{B}}{8\pi}\right)\boldsymbol{v} - \dfrac{1}{4\pi}\left(\boldsymbol{v}\cdot\boldsymbol{B}\right)\boldsymbol{B} + \eta(\boldsymbol{j}\times\boldsymbol{B}) - \boldsymbol{\sigma}\boldsymbol{v} + \boldsymbol{q}^{\mathrm{turb}} \end{array} \right),$$

where $\boldsymbol{\sigma} = \nu\rho[(\boldsymbol{\nabla}\boldsymbol{v}) + (\boldsymbol{\nabla}\boldsymbol{v})^T - (2/3)(\boldsymbol{\nabla}\cdot\boldsymbol{v})\boldsymbol{I}]$ is the viscous stress tensor, $\eta = (\nu/\mathrm{Pr_m}) = 1/(4\pi\sigma)$ the magnetic diffusivity with σ being the electric conductivity, and $\eta(\boldsymbol{j}\times\boldsymbol{B}) = (\eta/4\pi)(\nabla\times\boldsymbol{B})\times\boldsymbol{B}$. $\mathrm{Pr_m}$ is the magnetic Prandtl number. $\boldsymbol{q}^{\mathrm{turb}}$ is a turbulent diffusive heat flux, which would typically be proportional to the entropy gradient: $\boldsymbol{q}^{\mathrm{turb}} = -(1/\mathrm{Pr})\nu\rho T\nabla s$, where Pr is the Prandtl number.

Typically, ν is not taken to be the molecular viscosity coefficient but rather some *turbulent* value that takes care of the dissipative processes that cannot be resolved by the computational grid. Such *subgrid-scale viscosities* should only act where velocity gradients are strong causing srong turbulence. Therefore, they typically depend on velocity gradients like in the Smagorinsky-type of turbulent viscosity where

$$\nu^{\mathrm{t}} = c \left\{ 2 \left[\left(\frac{\partial v_x}{\partial x} \right)^2 + \left(\frac{\partial v_y}{\partial y} \right)^2 + \left(\frac{\partial v_z}{\partial z} \right)^2 \right] + \left(\frac{\partial v_x}{\partial y} + \frac{\partial v_y}{\partial x} \right)^2 + \left(\frac{\partial v_x}{\partial z} + \frac{\partial v_z}{\partial x} \right)^2 + \left(\frac{\partial v_y}{\partial z} + \frac{\partial v_z}{\partial y} \right)^2 \right\}^{1/2} ,$$

where c is a free parameter. This parameter is normally chosen as small as possible just in order to keep the numerical integration stable and smooth, but otherwise having no effect on large scales.

Some numerical *high resolution schemes* feature an inherent dissipation that acts like the explicit dissipative terms shown in the flux tensor above. This *artificial viscosity* is made as small as possible but still large enough to keep the numerical scheme stable. One then only programs the ideal equations. Of course, in this case it is difficult to quote the actual Reynolds and Prandtl numbers because they change from grid cell to grid cell depending on the flow. For certain applications it might be preferable to *explicitly include the dissipative terms* in the equations using constant dissipation coefficients, which yield well defined dimensionless numbers. However, one handles this, when integrating the ideal equations on a discrete computational grid, one is always locked with a *discretization error* that normally assumes the form of dissipative terms in the non-ideal equations.

See *LeVeque, Mihalas, Dorfi, & Müller (1998)* for more on computational methods for astrophysical fluid flow.

5. Equations and boundary conditions (cont.)

Typical boundary conditions for the thermal variables and the velocities

$$\frac{\partial v_{x,y,z}}{\partial z} = 0 \quad (\,\mathrm{or} \quad v_z = 0\,)\,; \ \lim_{t\to\infty} \epsilon = \epsilon_0$$

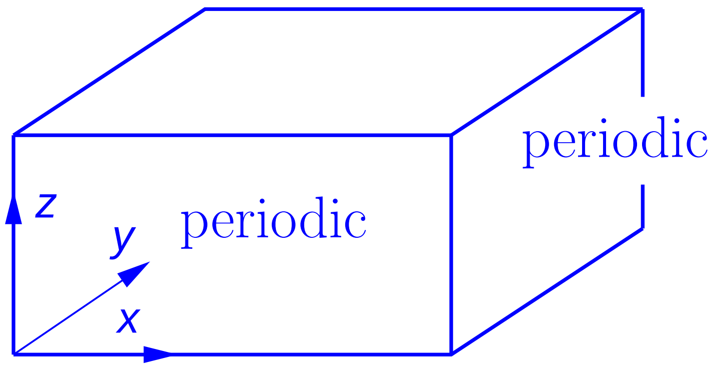

$$\frac{\partial v_{x,y}}{\partial z} = 0\,; \ \int \rho v_z \,\mathrm{d}\sigma = 0\,; \ \mathrm{outflow:}\ \frac{\partial s}{\partial z} = 0$$

$$\mathrm{inflow:}\ s = s_0$$

Periodic lateral boundary conditions in all variables. *Open bottom boundary* in the sense that the fluid can freely flow in and out of the computational domain under the condition of vanishing total mass flux.

Reflecting (closed) top boundary or open (transmitting) top boundary.

Note: For a pure hydrodynamic simulation, there are only *three free parameters*:

- The entropy of the inflowing material, s_0, which determines the effective temperature, $T_{\rm eff}$;
- The *chemical composition* of the plasma, which determines the equation of state and opacities;
- The surface gravity, $g_{\rm surf}$.

For the Sun, these parameters are all fixed.

Boundary conditions for the magnetic field

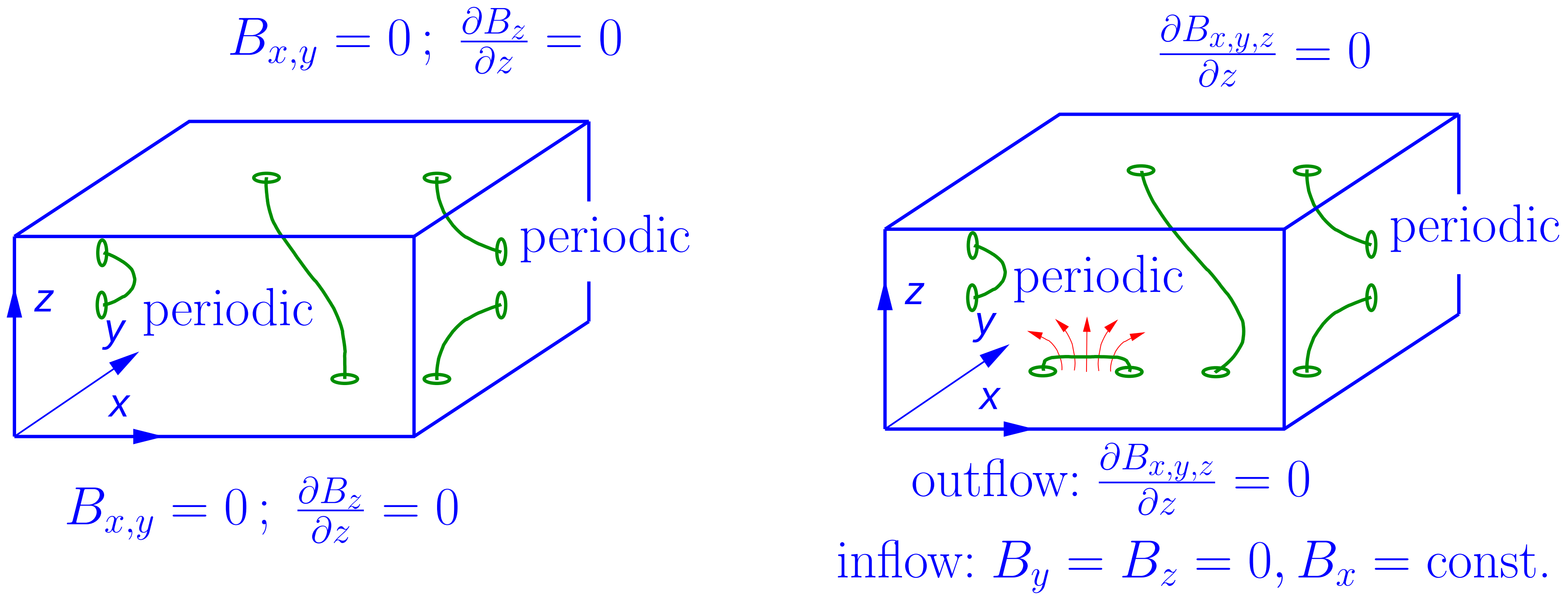

Boundary conditions for the magnetic field

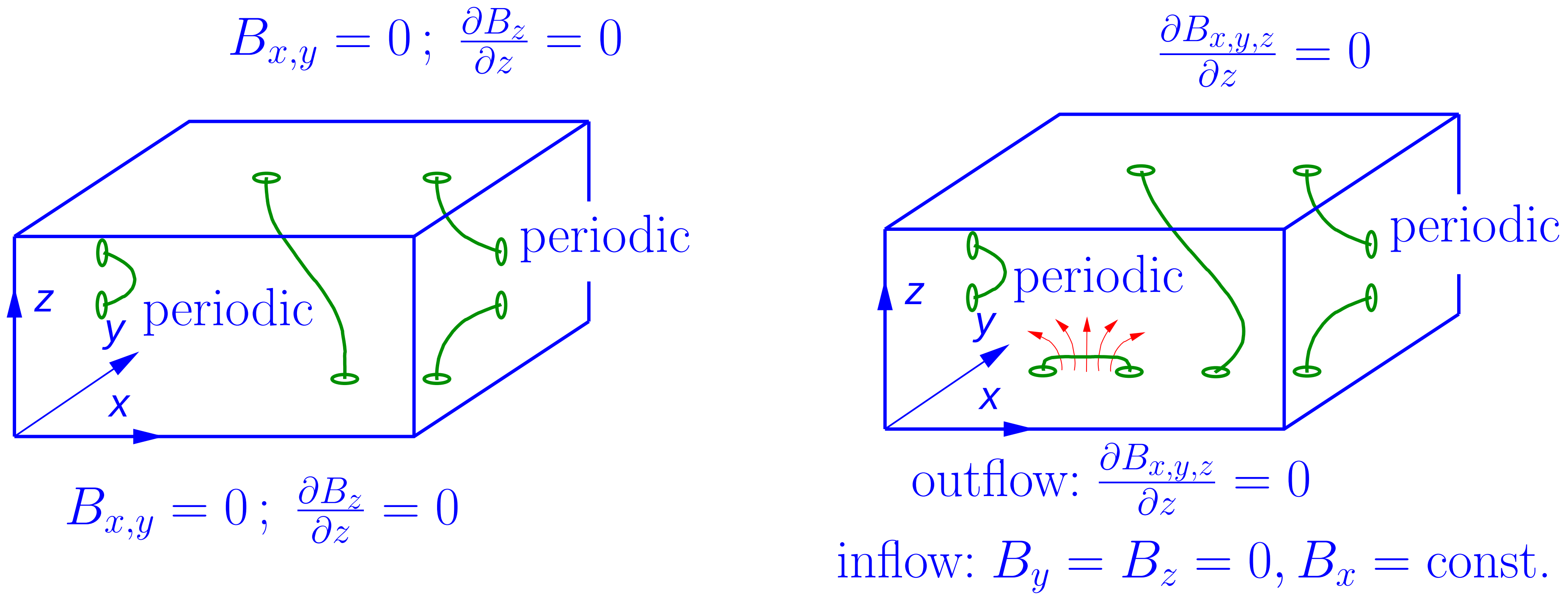

Note: The presence of a *magnetic field* introduces a *continuous spectrum of parameters* regarding to the initial condition for the magnetic field or conditions for a self exciting dynamo.

§ 9 Radiation transfer

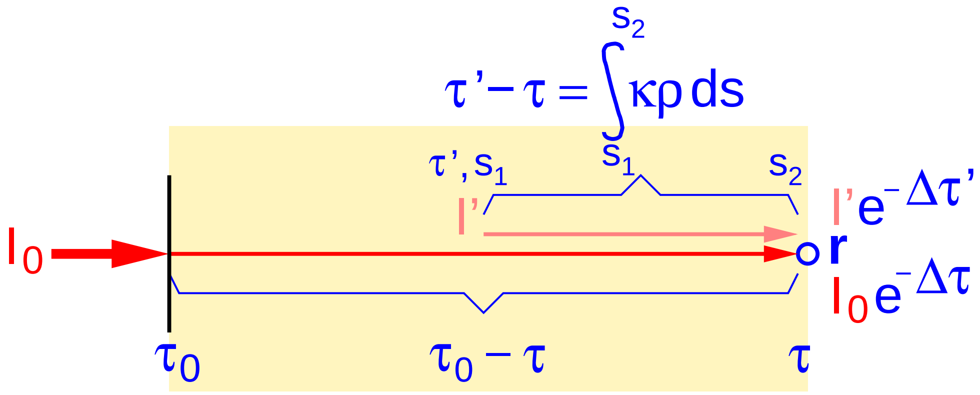

κ_ν: opacity per unit mass [cm^{2}g^{-1}]

τ: optical distance to $\boldsymbol{r}$

Formal solution of the radiative transfer equation

$$I(\boldsymbol{r},\boldsymbol{n}) = I_0 e^{-(\tau_0-\tau)} + \int_\tau^{\tau_0} S(\tau')\, e^{-(\tau'-\tau)} \mathrm{d}\tau'$$

For short: $I(\boldsymbol{r},\boldsymbol{n}) = \boldsymbol{\Lambda} S$ (Lambda operator)

The *radiative transfer equation* $\boxed{\dfrac{\mathrm{d}I_\nu}{\mathrm{d}\tau_\nu} = I_\nu - S_\nu}$ $\dfrac{\mathrm{d}I_\nu}{\mathrm{d}s} = -\kappa_\nu \rho (I_\nu - S_\nu)$

$I = I(\mathbf{r}, \hat{\mathbf{n}}, \nu, t)$ has dimension [erg cm^{-2} s^{-1} hz^{-1} sr^{-1}]

Radiative flux $\mathbf{F}_{\mathrm{rad}} = \int\limits_{4\pi}\int\limits_{0}^{\infty} I(\mathbf{r},\hat{\mathbf{n}},\nu)\hat{\mathbf{n}}\,\mathrm{d}\nu\,\mathrm{d}\omega$ [erg cm^{-2} s^{-1}]

Using the radiative transfer equation we obtain for the divergence of the radiative flux:

$$\begin{aligned}
\nabla\cdot\mathbf{F}_{\mathrm{rad}} &= \int\limits_{4\pi}\int\limits_{0}^{\infty}(\hat{\mathbf{n}}\cdot\nabla)I(\mathbf{r},\hat{\mathbf{n}},\nu)\,\mathrm{d}\nu\,\mathrm{d}\omega \\
&= \int\limits_{4\pi}\int\limits_{0}^{\infty}\left(\kappa(\mathbf{r},\nu)\rho(\mathbf{r})S(\mathbf{r},\nu) - \kappa(\mathbf{r},\nu)\rho(\mathbf{r})I(\mathbf{r},\hat{\mathbf{n}},\nu)\right)\mathrm{d}\nu\,\mathrm{d}\omega \\
&= 4\pi\int\limits_{0}^{\infty}\kappa(\mathbf{r},\nu)\rho(\mathbf{r})\left(S(\mathbf{r},\nu) - J(\mathbf{r},\nu)\right)\mathrm{d}\nu = -q_{\mathrm{rad}}
\end{aligned}$$

With $J(\mathbf{r},\nu) = \frac{1}{4\pi}\int\limits_{4\pi} I(\mathbf{r},\hat{\mathbf{n}},\nu)\,\mathrm{d}\omega$ being the *mean intensity*.

Radiation transfer (cont.)

$q_{\rm rad}$ *(per unit mass)* in a vertical section through a 3D solar model. $z = 1.3\,$Mm corresponds to $\langle\tau_{500}\rangle = 1$. *Dark/bright* shades indicate *radiative cooling/heating*.

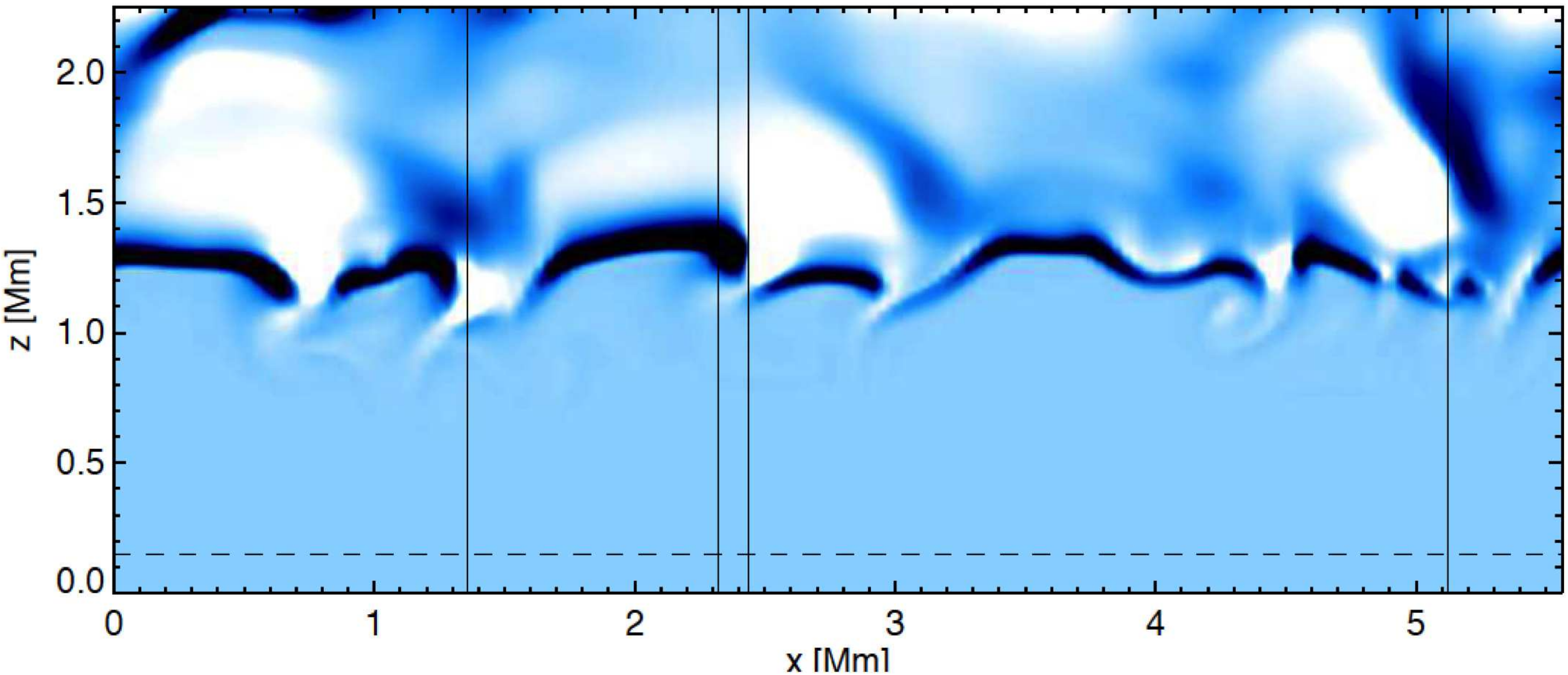

From *Steffen (2017)*.

Integration on long characteristics

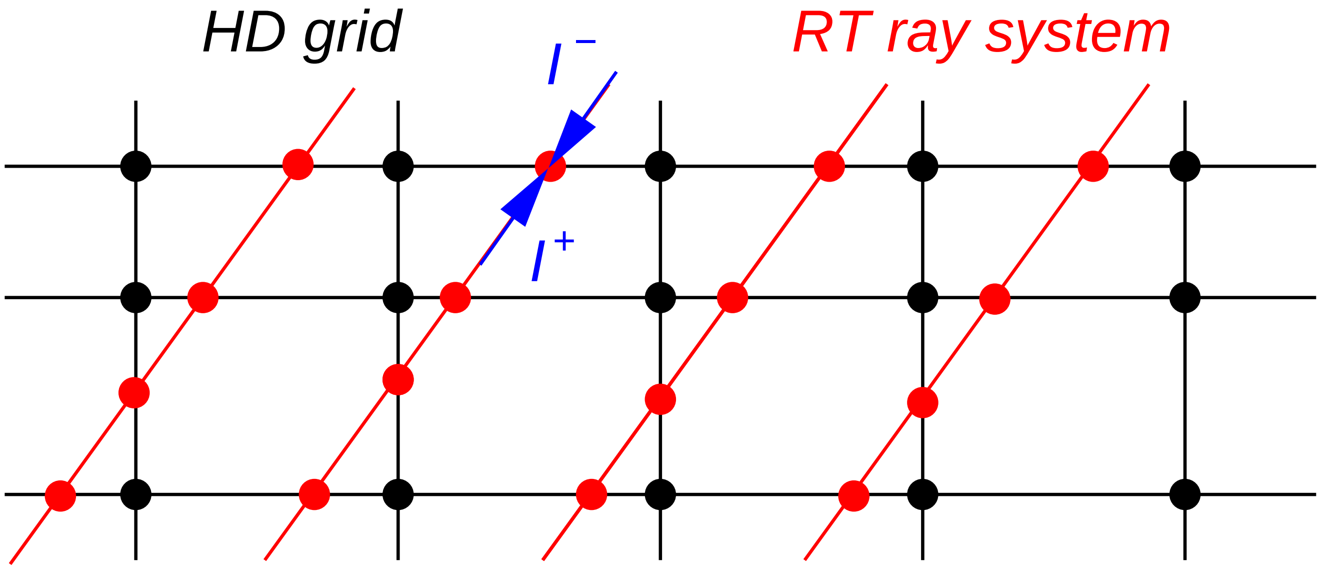

HD grid: ρ, e $\overset{\text{EOS}}{\longrightarrow}$ p, T $\rightarrow$ source function S, opacity $\rho\kappa$

$\rightarrow$ interpolation $\rightarrow$ RT Rays system: S, $\rho\kappa$

$\rightarrow$ solve RT for $y_\nu = (1/2)(I^+_\nu + I^-_\nu) - S_\nu$ (Feautrier scheme)

RT Ray system: $\rho\kappa y_\nu = q^{\theta,\phi}_{\mathrm{rad}}$ $\rightarrow$ flux conservative back-interpoation

$\rightarrow$ HD grid: $q^{\theta,\phi}_{\mathrm{rad}}$ $\rightarrow$ $\sum_{\theta,\phi} q^{\theta,\phi}_{\mathrm{rad}} = q_{\mathrm{rad}}$

Integration on short characteristics

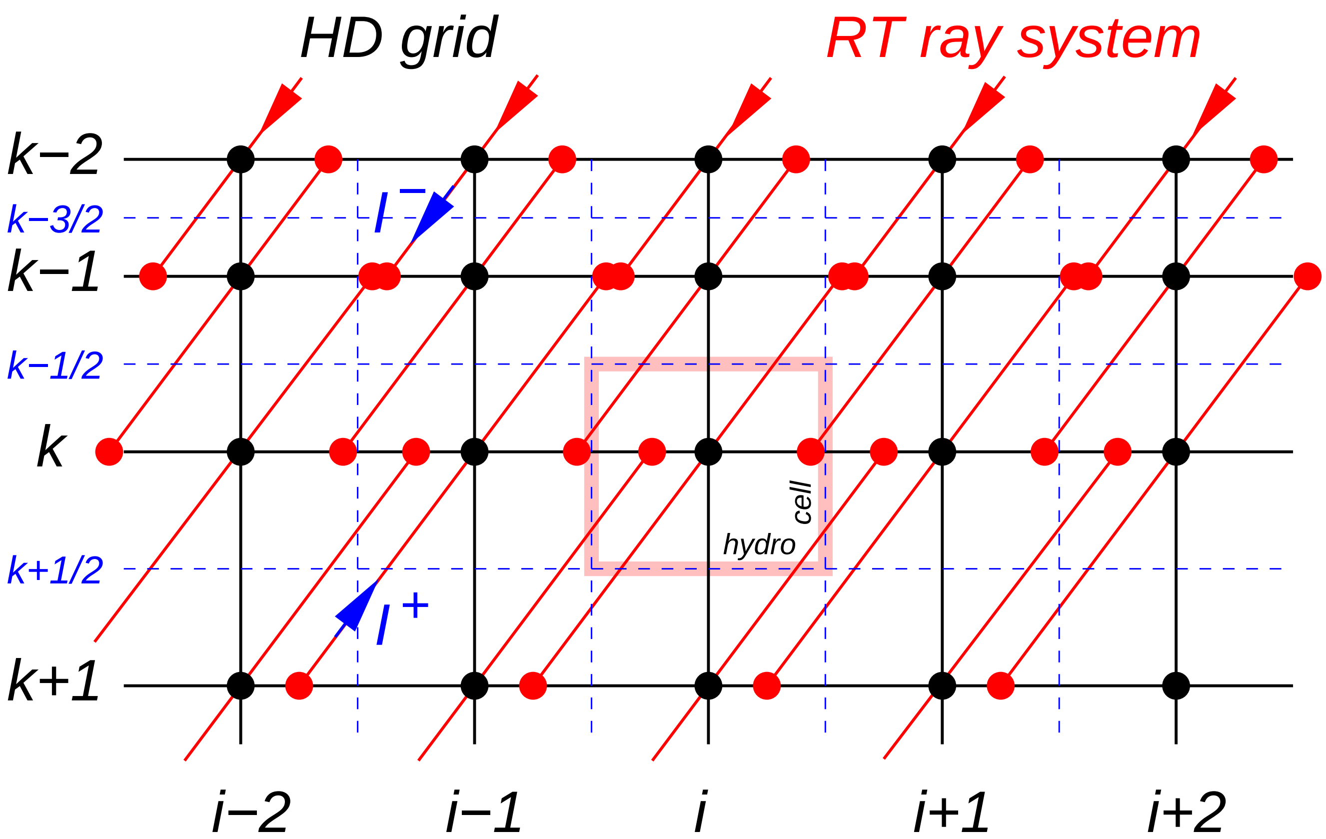

RT Rays system: start at top compute I^-, start at bottom compute I^+

$$\rightarrow \quad q_{\mathrm{rad}}(\theta,\phi) = q^-_{\mathrm{rad}}(\theta,\phi) + q^+_{\mathrm{rad}}(\theta,\phi)$$

important: flux conservative interpolation of intensities

Conservation of radiative flux

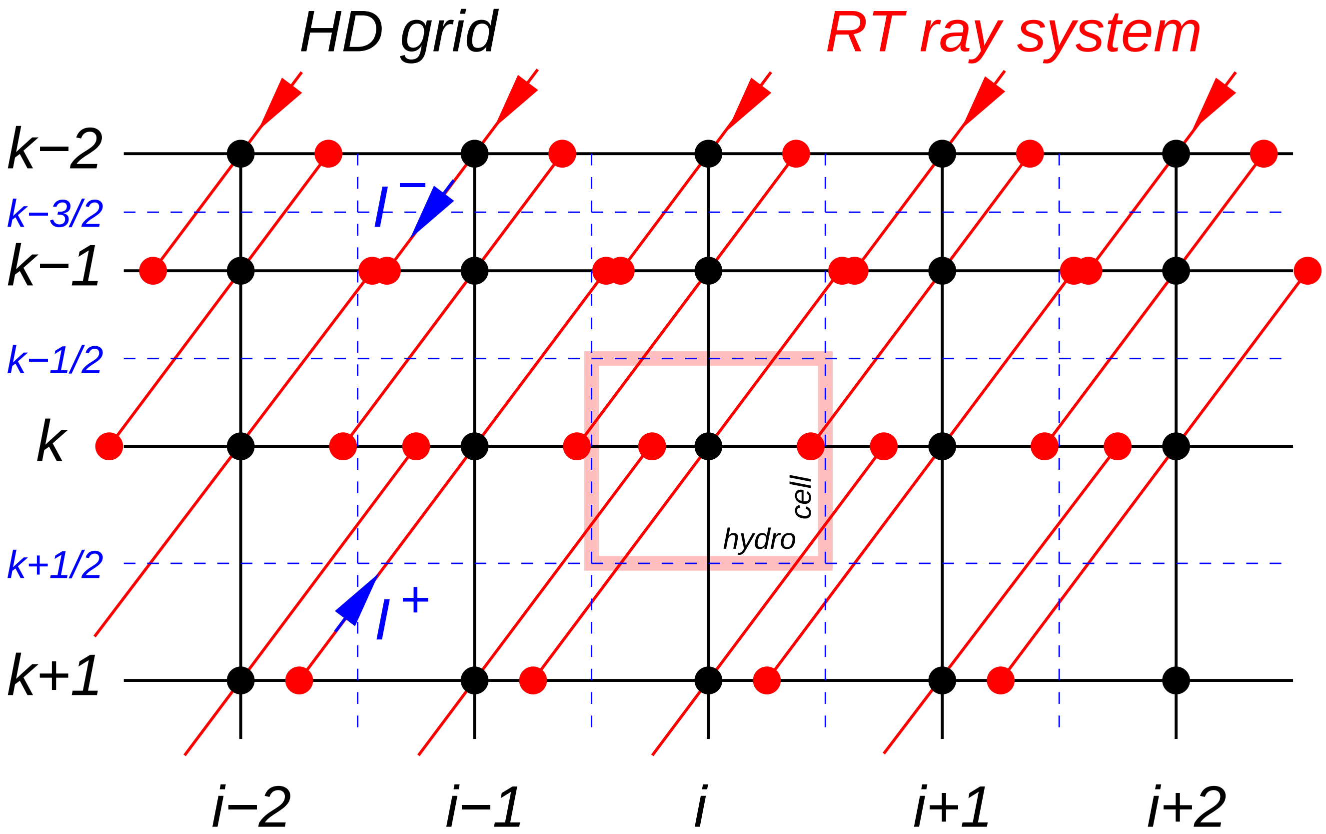

$$\int_x \int_y F_{\mathrm{rad}}^{k-\frac{1}{2}}\,\mathrm{d}x\,\mathrm{d}y - \int_x \int_y F_{\mathrm{rad}}^{k+\frac{1}{2}}\,\mathrm{d}x\,\mathrm{d}y = \int_x \int_y \int_{z_{k+1/2}}^{z_{k-1/2}} -q_{\mathrm{rad}}(x,y,z)\,\mathrm{d}x\,\mathrm{d}y\,\mathrm{d}z$$

Adapted from *Steffen (2017)*.

Radiation transfer (cont.)

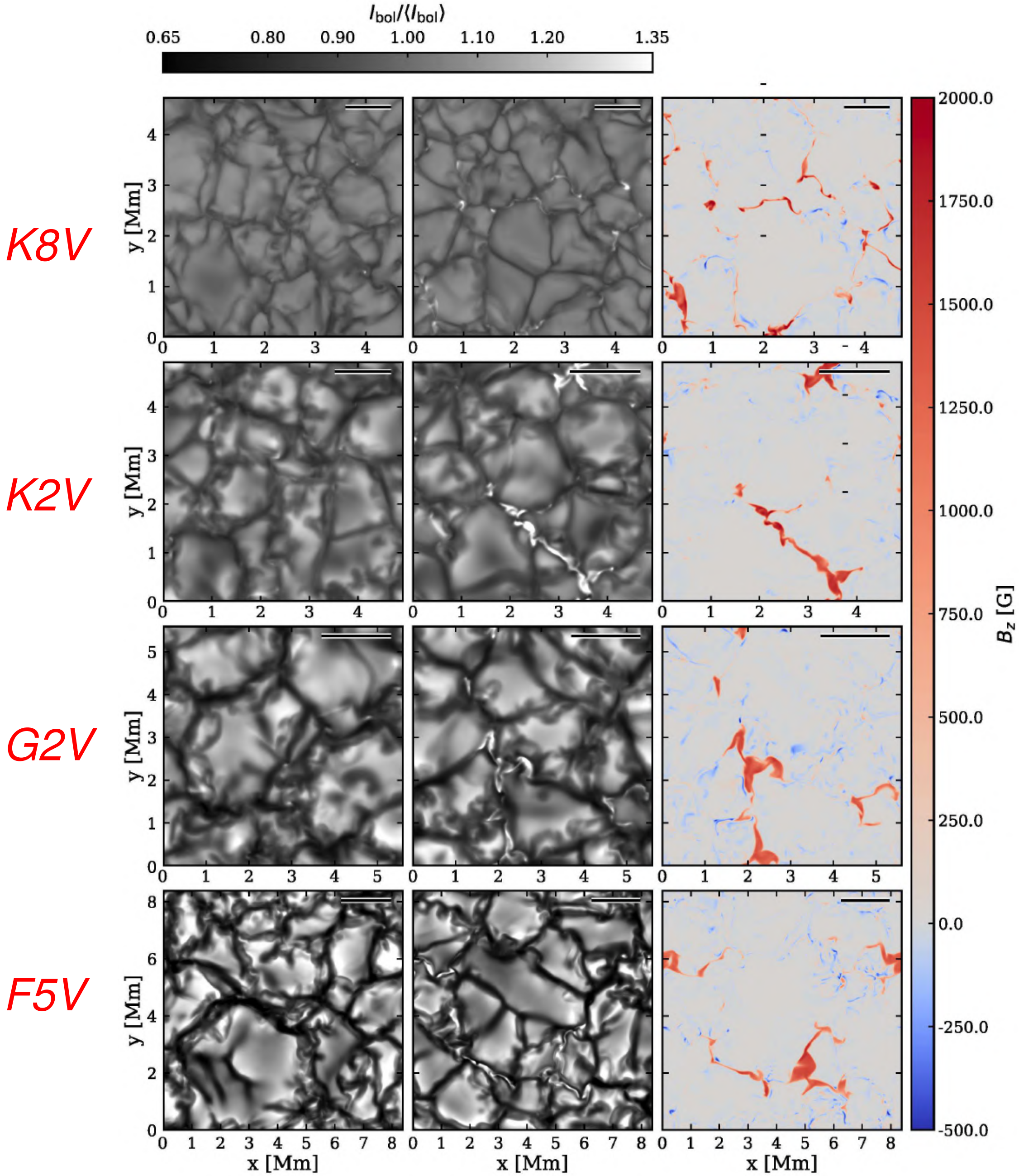

- *"Box in a star" simulations* of the surface layers of four spectral types;
- Each simulation is *run twice*: with and without magnetic fields;
- Initial vertical homogeneous field of *50 G* and *100 G*;
- Multi-group *radiation transfer* using 5 opacity bins;
- From *Salhab et al. (2018, A&A 614, A78)*.

§ 10 Multi-group radiation transfer

Nordlund, 1982; Ludwig, 1992

$$q_{\mathrm{rad}} = -\boldsymbol{\nabla} \cdot \boldsymbol{F}_{\textsf{rad}} = 4\pi\rho \int \kappa_\lambda (J_\lambda - B_\lambda)\, \mathrm{d}\lambda \,,$$

$$\begin{aligned}
\int \kappa_\lambda (J_\lambda - B_\lambda)\, \mathrm{d}\lambda &= \sum_j \kappa_{\lambda_j} (J_{\lambda_j} - B_{\lambda_j})\, w_{\lambda_j} \\
&= \sum_i \sum_{j(i)} \kappa_{\lambda_j} (J_{\lambda_j} - B_{\lambda_j})\, w_{\lambda_j} \\
&= \sum_i \sum_{j(i)} \kappa_{\lambda_j} (\boldsymbol{\Lambda}_{\lambda_j}(B_{\lambda_j}) - B_{\lambda_j})\, w_{\lambda_j} \\
&\approx \sum_i \kappa_i (\boldsymbol{\Lambda}_i - \mathbf{1}) (\sum_{j(i)} B_{\lambda_j}\, w_{\lambda_j}) \\
&\doteq \sum_i \kappa_i (\boldsymbol{\Lambda}_i - \mathbf{1}) (B_i\, w_i) \doteq \sum_i \kappa_i (J_i - B_i) w_i
\end{aligned}$$

Strategy for opacity binning:

- concentrate on radiative transfer in vertical direction,
- group together frequencies with as similar a $\tau_\nu(s)$-relationship as possible, so that $\mathbf{\Lambda}_{\lambda_{j(i)}}$ is very similar $\forall j$ of a given bin i,
- choose clever averaging procedure for κ_ν, (Rosseland averages for $\tau_i > 1$, Planck averages for $\tau_i < 1$).

See also *Nordlund, Å: 1982, A&A 107,1*; *Ludwig, H.-G.: 1992, thesis Univ. Kiel*; *Vögler et al.: 2004, A&A 421, 741*; *Hayek et al.: 2010, A&A 517,A49*.

Testing the OBM. Integrated radiative flux

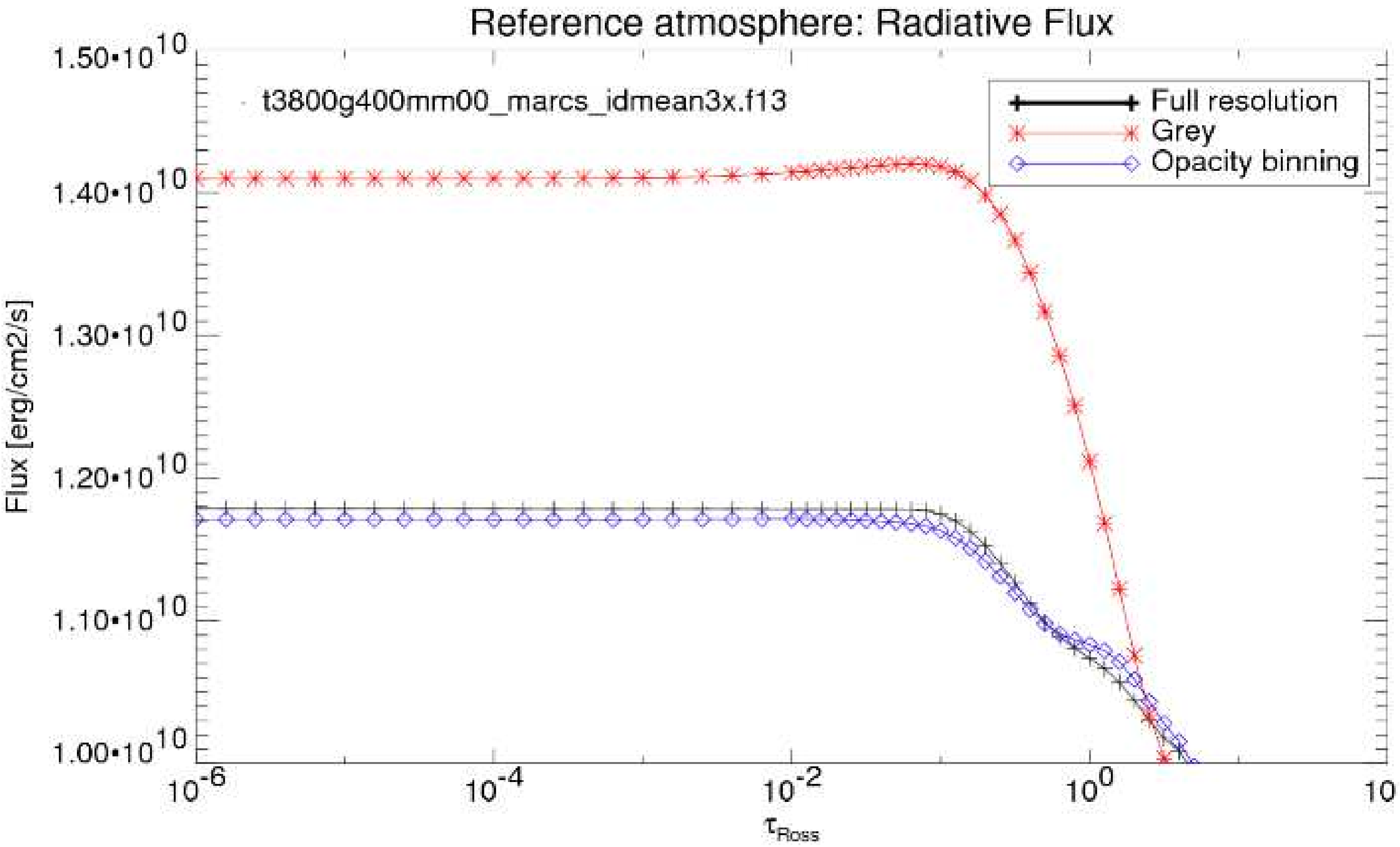

Courtesy, *M. Steffen.*

Intensity maps for different opacity bins

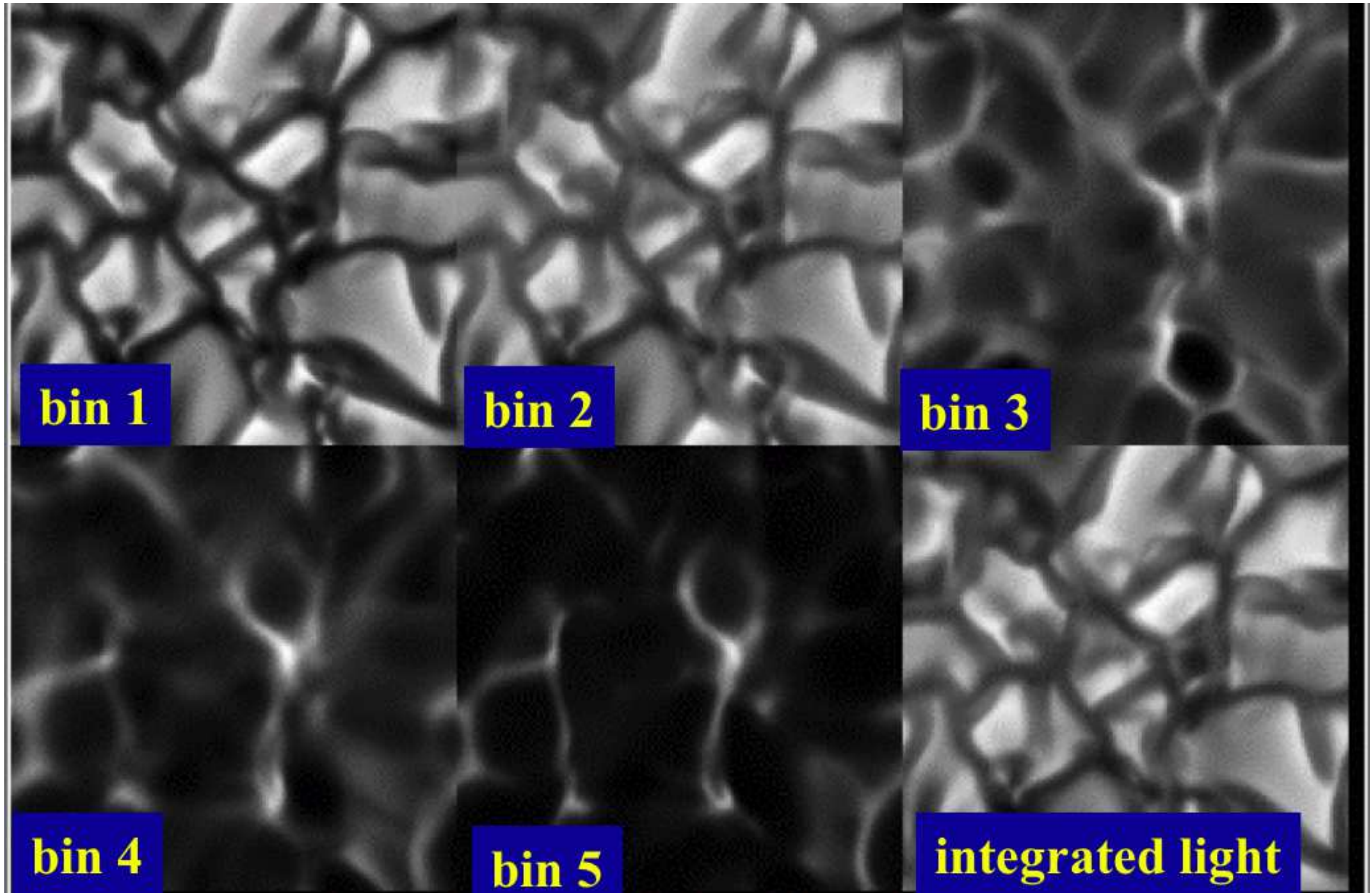

Courtesy, *M. Steffen.*

Notice that bin 3 to 5 show "inverse granulation" as their opacities represent medium to strong line cores.

§ 11 Heat conduction

If the *transition region and corona* is to be included in the simulation, *heat conduction* must be taken into account as an important mode of energy transport. For a fully ionized plasma, the heat flux (carried by the electrons) is given by

$$F_c = -\kappa_0 T^{5/2} \nabla_{||} T \, ,$$

where the gradient of T is taken along the magnetic field ($\nabla_{||}$) and $\kappa_{||} = \kappa_0 T^{5/2}$ is the *Spitzer* (1956) *coefficient for thermal conduction* along the magnetic field. The conductive part of the energy equation is typically handled in a separate operator splitting step

$$\frac{\partial E}{\partial t} = -\boldsymbol{\nabla} \cdot \boldsymbol{F}_c = -\nabla_{||} \left[\kappa_0 T^{5/2} \nabla_{||} T \right] \, .$$

Since this is a parabolic partial differential equation, the CFL condition scales $\propto \Delta x^2$ instead of $\propto \Delta x$ as for hyperbolic equations. This means, it must be solved with an implicit numerical scheme to achieve tolerable time stepping.

Heat conduction (cont.)

The second important ingredient is a (optically thin) *radiative loss function*, which takes care of the radiative loss ($q_{\rm rad}$) *in the tenuous atmosphere from the upper chromosphere up to the corona*. It can be approximated as

$$q_{\rm rad,thin} = -n_{\rm H} n_{\rm e} f(T) e^{-P/P_0} \,.$$

$n_{\rm H}$ and $n_{\rm e}$ are the number densities of H and electrons, respectively, $f(T)$ is a function of the temperature and $\exp(-P/P_0)$ provides a cutoff where $P > P_0$.

Heat conduction (cont.)

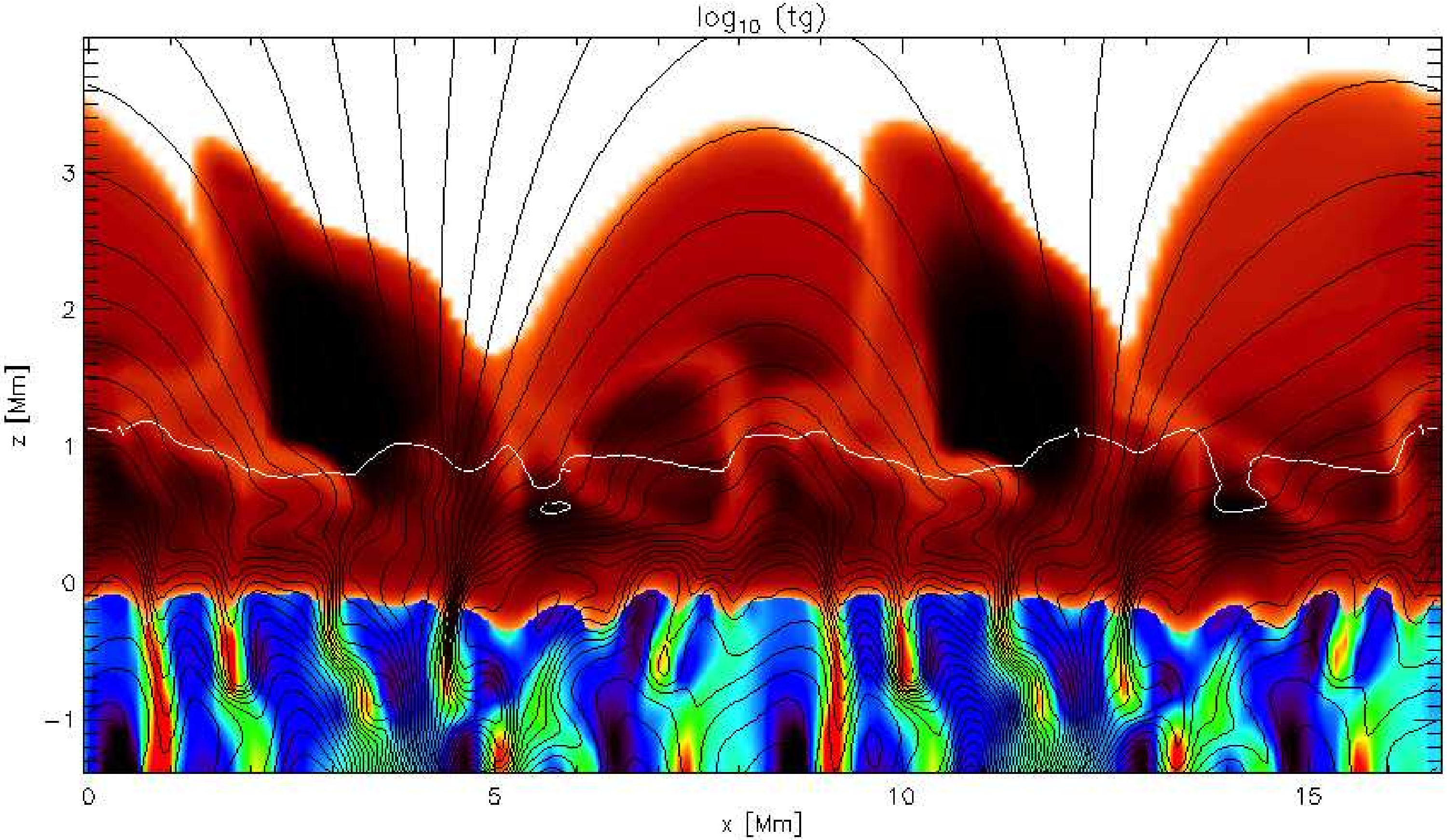

Two-dimensional *Bifrost simulation* from the top of the convection zone to the corona, *including the transition region* (transition from reddish to white colors). The color shading indicate the temperature above the lower white curve ($\tau_c = 1$). Below it, the colors indicate the vertical velocity, downflows being red. The upper white curve indicates $\beta = 1$. Above it the magnetic field (black field lines) dominates the gas pressure. From *Hansteen & Carlsson (2005)*.

Heat conduction (cont.)

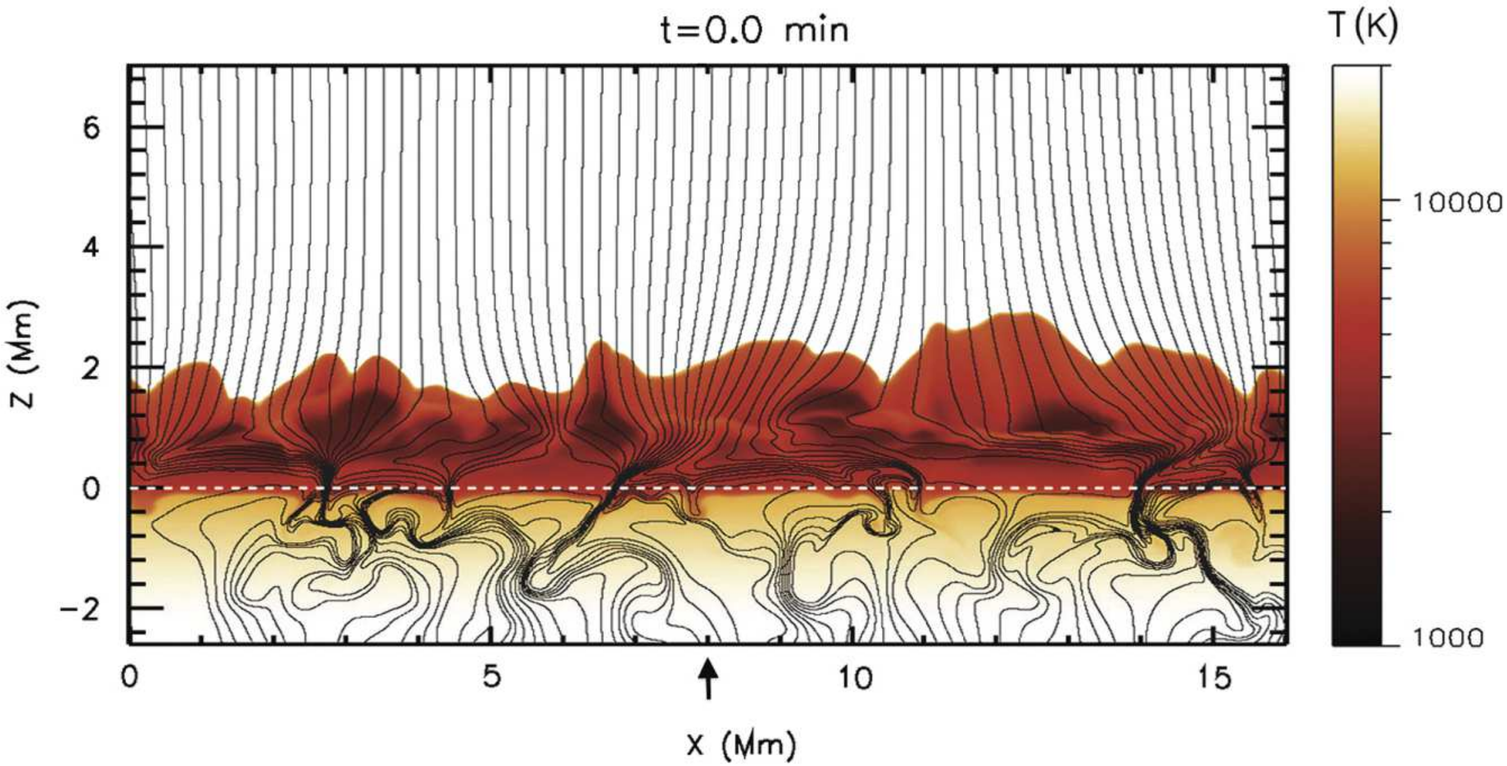

Two-dimensional *Bifrost simulation* from the top of the convection zone to the corona, *including the transition region* (transition from reddish to white colors). The color shading indicates the temperature. Courtesy, *D. Nóbrega Siverio*.

§ 11 Heat conduction (cont.)

Three-dimensional CO^{5}BOLD radiation-hydrodynamic simulation of surface convection including chromospheric layers and weak magnetic fields. The dimensions of the vertical section are: Width, 9600 km; Height above the surface of $\tau = 1$, 1600 km; Depth below this surface level: 1200 km. Colores indicate the temperature. No transition region is present.

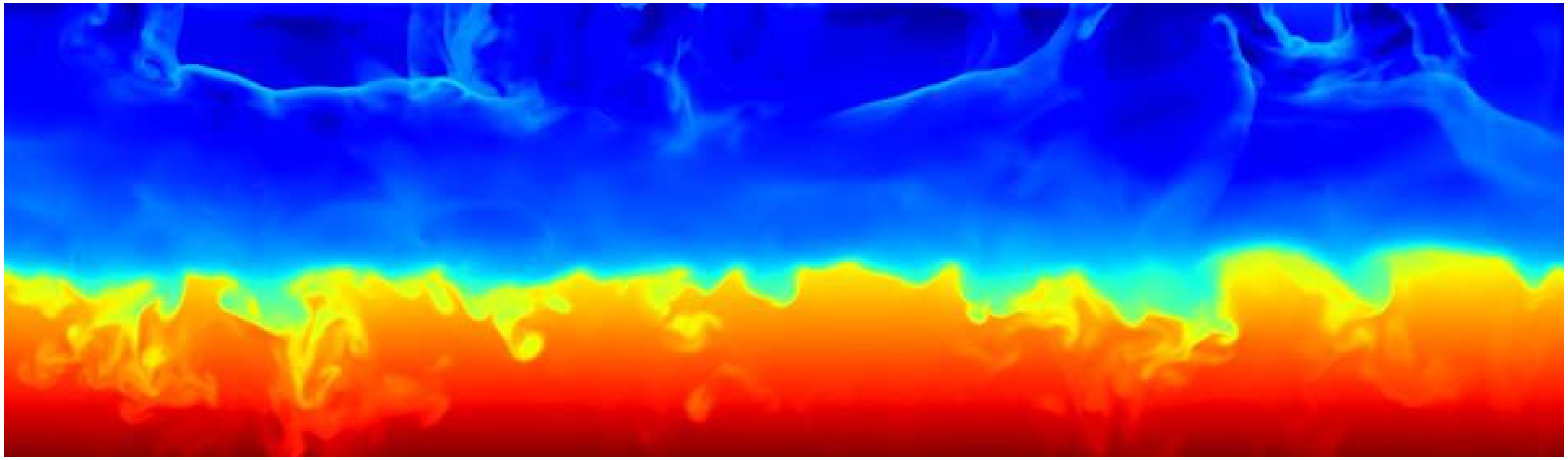

Courtesy, *F. Calvo, IRSOL*

§ 12 Non-equilibrium Hydrogen ionization

Under the condition of the dynamic solar chromosphere, the *assumption of statistical equilibrium*

$$\underbrace{n_i \sum_{j \neq i}^{N} P_{ij}}_{\text{transitions from } i \text{ to other levels}} = \underbrace{\sum_{j \neq i}^{N} n_j P_{ji}}_{\text{transitions from others to level } i} .$$

is not valid anymore. Instead the dynamic change in level populations and ionization of H and He must be taken into account. We then solve the *time-dependent rate equations*

$$\frac{\partial n_i}{\partial t} + \nabla \cdot (n_i \mathrm{v}) = \sum_{j \neq i}^{n_l} n_j P_{ji} - n_i \sum_{j \neq i}^{n_l} P_{ij}$$

$P_{ij} = C_{ij} + R_{ij}$, where we assume that the radiation field in each transition, both, bound-bound and bound-free, can be described by a formal radiation temperature T_{rad}.

In the method of fixed radiative rates (*Sollum 1999*), we assume that the radiation field in each transition, both, bound-bound and bound-free, can be described by a formal radiation temperature:

$$J_\nu = \frac{2h\nu^3}{c^2} \frac{1}{\mathrm{e}^{h\nu/kT_{\mathrm{rad}}} - 1}$$

Thus, we obtain the *fixed radiative rates* for bound-bound transitions

$$\begin{aligned} R_{lu} &= B_{lu} J_{\nu_0} = \frac{4\pi^2 e^2}{h\nu_0 m_e c} f_{lu} \frac{2h\nu_0^3}{c^2} \frac{1}{\mathrm{e}^{h\nu_0/kT_{\mathrm{rad}}} - 1} \\ R_{ul} &= A_{ul} + B_{ul} J_{\nu_0} = \frac{g_l}{g_u} \mathrm{e}^{h\nu_0/kT_{\mathrm{rad}}} R_{lu} \end{aligned}$$

B_{lu}: Einstein coefficient for radiative excitation; f_{lu}: oscillator strength; A_{ul}, B_{ul}: Einstein coefficient for spontaneous and stimulated deexcitation, respectively; $g_{l,u}$: statistical weights of the lower and upper level.

Non-equilibrium Hydrogen ionization (cont.)

The hydrogen bound-free excitations have a Kramer's absorption cross section:

$$\sigma_{ic}(\nu) = \alpha_0 \left(\frac{\nu_0}{\nu}\right)^3, \nu > \nu_0 \, ,$$

where α_0 is the absorption cross-section at the edge frequency ν_0. In this case the radiative rate coefficients are

$$\begin{aligned} R_{ic} &= 4\pi \int_{\nu_0}^{\infty} \frac{\sigma_{ic}(\nu)}{h\nu} J_\nu \mathrm{d}\nu = \frac{8\pi}{c^2}\alpha_0 \nu_0^3 \int_{\nu_0}^{\infty} \frac{1}{\nu} \frac{1}{\mathrm{e}^{h\nu/kT_{\mathrm{rad}}} - 1} \mathrm{d}\nu \\ &= \frac{8\pi}{c^2}\alpha_0 \nu_0^3 \sum_{n=1}^{\infty} E_1 \left[n \frac{h\nu_0}{kT_{\mathrm{rad}}} \right] , \quad E_1 \text{ being the first exponential integral} \\ R_{ci} &= 4\pi \left[\frac{n_i}{n_c}\right]_{\mathrm{LTE}} \int_{\nu_0}^{\infty} \frac{\sigma_{ic}(\nu)}{h\nu} \left(\frac{2h\nu^3}{c^2} + J_\nu \right) \mathrm{e}^{-h\nu/kT_e} \mathrm{d}\nu \\ &= \frac{8\pi}{c^2}\alpha_0 \nu_0^3 \left[\frac{n_i}{n_c}\right]_{\mathrm{LTE}} \sum_{n=1}^{\infty} E_1 \left[\left(n \frac{T_e}{T_{\mathrm{rad}}} + 1 \right) \frac{h\nu_0}{kT_e} \right] . \end{aligned}$$

Non-equilibrium Hydrogen ionization (cont.)

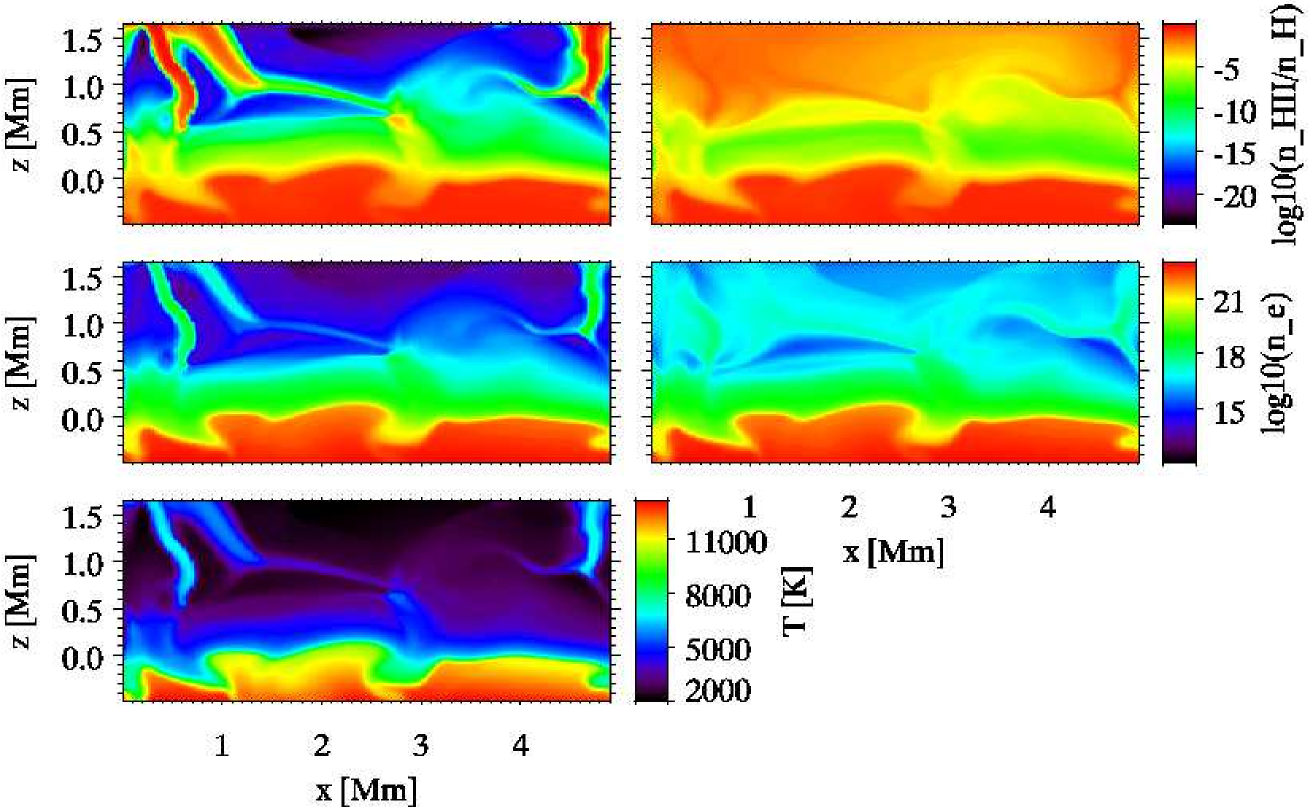

Effect of dynamic H-ionization in the upper part of a 2-D simulation. *Left column: LTE* ionization degree and electron density. *Right column:* Corresponding *time-dependent NLTE* quantities. Bottom left: Gas temperature, which is the same for the LTE and the time-dependent case. From *Leenaarts & Wedemeyer-Böhm 2006*.

§ 13 Chemical reaction network

For certain applications, e.g., the effect of CO in the solar atmosphere, an optional module for the treatment of a network of chemical reactions was added to the CO^5BOLD code. For further details see *Wedemeyer-Böhm et al. (2005), A&A 438, 1043* and *Wedemeyer-Böhm & Steffen (2007), A&A 462, L31*.

The *operator splitting* method is used in order to account for the time evolution of chemical species. In a *first step* the chemical species are advected together with all the other hydrodynamic quantities:

$$\frac{\partial n_i}{\partial t} + \nabla \cdot (n_i \boldsymbol{v}) = 0\,,$$

where n_i is the number density of a chemical species and $\boldsymbol{v}$ the velocity of the hydrodynamical flow.

Chemical reaction network (cont.)

In a *second step* (between the hydro step and the radiation-transfer step), the change in number density due to chemical reactions is accounted for:

$$
\begin{aligned}
\left(\frac{\partial n_i}{\partial t}\right)_{\rm chem} \quad = \quad & -n_i \sum_j k_{2,ij}\, n_j \\
& + \sum_j \sum_l k_{2,jl}\, n_j n_l \\
& - n_j \sum_j \sum_l k_{3,ijl}\, n_j n_l \\
& + \sum_j \sum_l \sum_m k_{3,jlm}\, n_j n_l n_m \ ,
\end{aligned}
$$

where n_i is the number densities of species i, which decreases or increases due to two-body reactions with rates $k_{2,ij}$ and $k_{2,jl}$, respectively. Three-body reactions are analogously accounted for by the third and fourth term with rates $k_{3,ijl}$ and $k_{3,jlm}$. It results in a (stiff!) system of of ordinary differential equations.

Chemical reaction network (cont.)

The rates have the basic form

$$k = \alpha\, T_{300}^{\beta}\, \mathrm{e}^{-\gamma/T}\ ,$$

where $T_{300} = T/300\,$K. For catalytic reactions the number density of a representative metal n_{M} enters: The rates have the basic form

$$k = n_{\mathrm{M}} \alpha\, T_{300}^{\beta}\, \mathrm{e}^{-\gamma/T}\ .$$

The coefficients α, β, and γ are compiled in tables, e.g., in *Wedemeyer-Böhm et al. (2005), A&A 438, 1043*

Chemical reaction network (cont.)

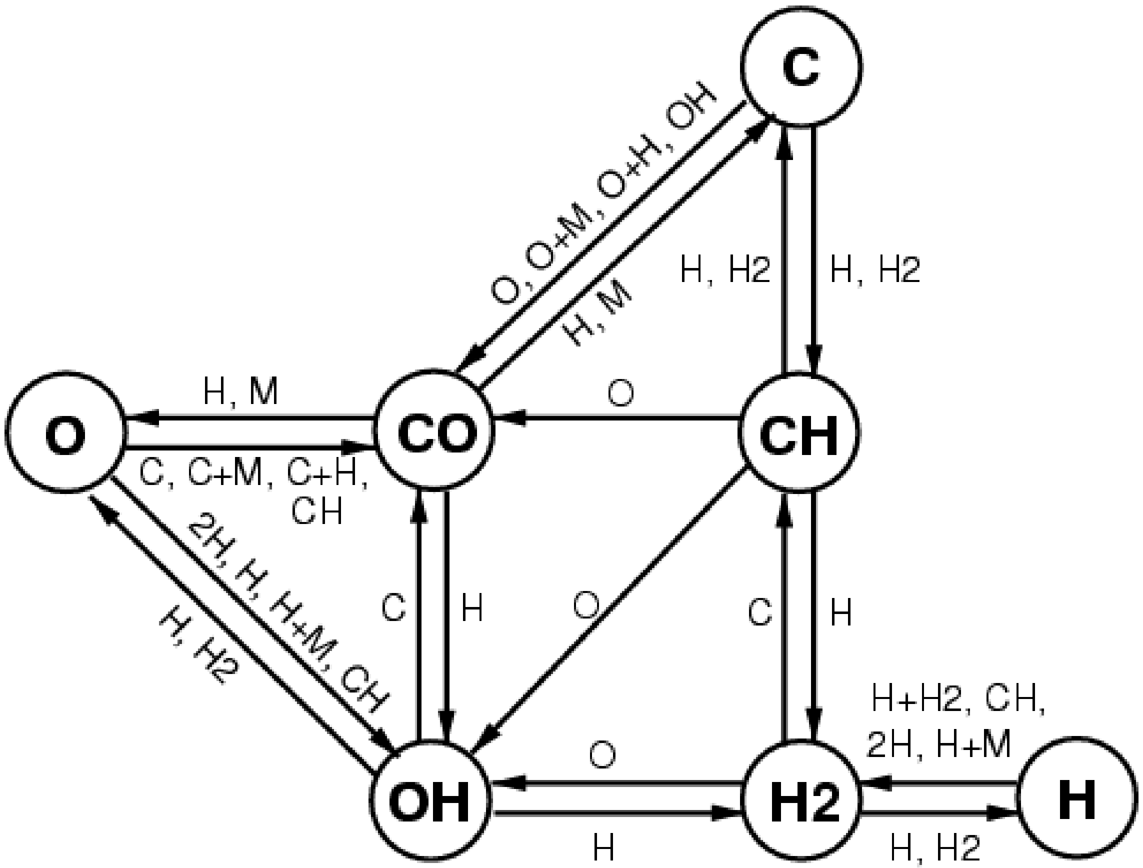

Chemical reaction network:

7 chemical species, H, H_2, C, O, CO, CH, OH, plus a representative metal M and 27 chemical reactions. From *Wedemeyer-Böhm et al. (2005), A&A 438, 1043*

Chemical reaction network (cont.)

Radiative cooling via CO lines:

- Two opacity bands:

  1.) *continuum band* with Rosseland mean opacity κ_{R} without infrared.

  2.) *infrared band* at 4.7 μm with Rosseland mean opacity plus CO line opacity, $\kappa_{\mathrm{R}} + \kappa_{CO}$.

- CO opacity calculated from (time dependent) CO number density.

Application examples:

- movie of CO number density in two-dimensional hydrodynamic solar convection.
- animation of “CO clouds” from a three-dimensional simulation.

References

Brandenburg, A., and Dobler, W.: 2002, *Hydromagnetic turbulence in computer simulations*, Comput. Phys. Comm. 147, 471-475

Calvo, F., Steiner, O., & Freytag, B.: 2016, *Non-magnetic photospheric bright points in 3D simulations of the solar atmosphere*, A&A, 596, A43

Felipe, T., Khomenko, E., Collados, M.: 2010, *Magneto-acoustic Waves in Sunspots: First Results From a New Three-dimensional Nonlinear Magnetohydrodynamic Code*, ApJ 719, 357-377

Felker, K.G. and Stone, J.M.: 2018, *A fourth-order accurate finite volume method for ideal MHD via upwind constrained transport*, J. Comput. Phys. 375, 1365-1400

Freytag, B., Steffen, M., and Dorch, B.: 2002, *Spots on the surface of Betelgeuse – Results from new 3D stellar convection models*, Astronomical Notes/AN 323, 213-219

Freytag, B., Steffen, M., Ludwig, H.-G., and Holweger, H.: 2004, *Numerical simulation of the three-dimensional structure and dynamics of the non-magnetic solar chromosphere*, A&A 414, 1121-1137

References (cont.)

Freytag, B. et al.: 2008, *CO^{5}BOLD user manual*, http://www.astro.uu.se/˜bf/co5bold_main.html

Freytag, B., Steffen, M., Ludwig, H.-G., Wedemeyer-Bhm, S., Schaffenberger, W., and Steiner, O.: 2012, *Simulations of stellar convection with CO5BOLD*, J. Comput. Phys. 231, 919-959

Fryxell, B., Olson, K., Ricker, P., Timmes, F.X. Zingale, M., Lamb, D.Q., Macneice, P., Rosner, R. Truran, J.W., and Tufo, H.: 2000, *FLASH: an Adaptive Mesh Hydrodynamics Code for Modeling Astrophysical Thermonuclear Flashes*, ApJ Suppl. Ser. 131, 273-334

Gudiksen, B.V., Carlsson, M., Hansteen, V.H., Hayek, W., Leenaarts, J., and Martínez-Sykora1, J.: 2011, *The stellar atmosphere simulation code Bifrost: Code description and validation*, A&A 531, A154

References (cont.)

Hayek, W., Asplund, M., Carlsson, M., Trampedach, R., Collet, R., Gudiksen, Hansteen, V., and Leenaarts, J.: 2010, *Radiative transfer with scattering for domain-decomposed 3D MHD simulations of cool stellar atmospheres: Numerical methods and application to the quiet, non-magnetic, surface of a solar-type star*, A&A 517, A49

Hayes, J.C., Norman, M.L., Fiedler, R.A., Bordner, J.O., Li, P.S.; Clark, S.E., ud-Doula, A., Mac Low, M.-M.: 2006, *Simulating Radiating and Magnetized Flows in Multiple Dimensions with ZEUS-MP*, ApJ Suppl. Ser. 165, 188-228

Leenaarts, J. and Wedemeyer-Böhm, S.: 2006, *Time-dependent hydrogen ionisation in 3D simulations of the solar chromosphere. Methods and first results*, A&A 460, 301-307

LeVeque, R.J., Mihalas, D., Dorfi, E.A., and Müller, E.: 1998, Computational Methods for Astrophysical Fluid Flow, O. Steiner & A. Gautschy (eds.), Springer-Verlag, Berlin

Ludwig, H.-G.: 1992, *Nichtgrauer Strahlungstransport in numerischen Simulationen stellarer Konvektion*, Ph.D. thesis, Christian-Albrechts-Universität, Kiel

References (cont.)

Mandli K.T., Ahmadia, A.J., Berger, M., Calhoun, D., George, D.L., Hadjimichael, Y., Ketcheson, D.I., Lemoine, G.I., LeVeque, R.J.: 2016, *Clawpack: building an open source ecosystem for solving hyperbolic PDEs*, PeerJ Computer Science 2:e68, https://doi.org/10.7717/peerj-cs.68

Muthsam, H.J., Kupka, F., Löw-Baselli, B., Obertscheider, C., Langer, M., Lenz, P.: 2010, *ANTARES - A Numerical Tool for Astrophysical RESearch with applications to solar granulation*, New Astronomy 15, 460-475

Nordlund, Å: 1982, *Numerical simulations of the solar granulation*, A&A 107, 1-10

Salhab, R.G., Steiner, O., Berdyugina, S.V., Freytag, B., Rajaguru, S.P., and Steffen, M.: 2018, *Simulation of the small-scale magnetism in main sequence stellar atmospheres*, A&A 614, A78

Sollum, E.: 1999, Master thesis, University of Oslo, Norway

Steffen, M.: 2017, *Radiation transport in CO5BOLD*, Mem. Soc. Astr. Ital. 88, 22

Teyssier, R.: 2002, *Cosmological hydrodynamics with adaptive mesh refinement. A new high resolution code called RAMSES*, A&A 385, 337-364

References (cont.)

Vögler, A., Bruls, J.H.M.J., and Schüssler, M.: 2004, *Approximations for non-grey radiative transfer in numerical simulations of the solar photosphere*, A&A 421, 741-754

Vögler, A., Shelyag, S., Schüssler, M., Cattaneo, F. Emonet, T., and Linde, T.: 2005, *Simulations of magneto-convection in the solar photosphere: Equations, methods, and results of the MURaM code* A&A 429, 335-351

Wedemeyer-Böhm, S., Kamp, I., Bruls, J., and Freytag, B.: 2005, *Carbon monoxide in the solar atmosphere. I. Numerical method and two-dimensional models*, A&A 438, 1043-1057

Wedemeyer-Böhm, S. and Steffen, M.: *Carbon monoxide in the solar atmosphere. II. Radiative cooling by CO lines*, A&A 462, L31-L35

Wedemeyer-Böhm, S. and Steiner, O.: 2006, *CO^{5}BOLD Workshop*, http://folk.uio.no/svenwe/cws2006/index.html

Ziegler, U.: 2011, *A semi-discrete central scheme for magnetohydrodynamics on orthogonal-curvilinear grids*, J. Comput. Phys. 230, 1035-1063

Part IV: MHD simulations: Case studies

§ 14 Basic postdictions

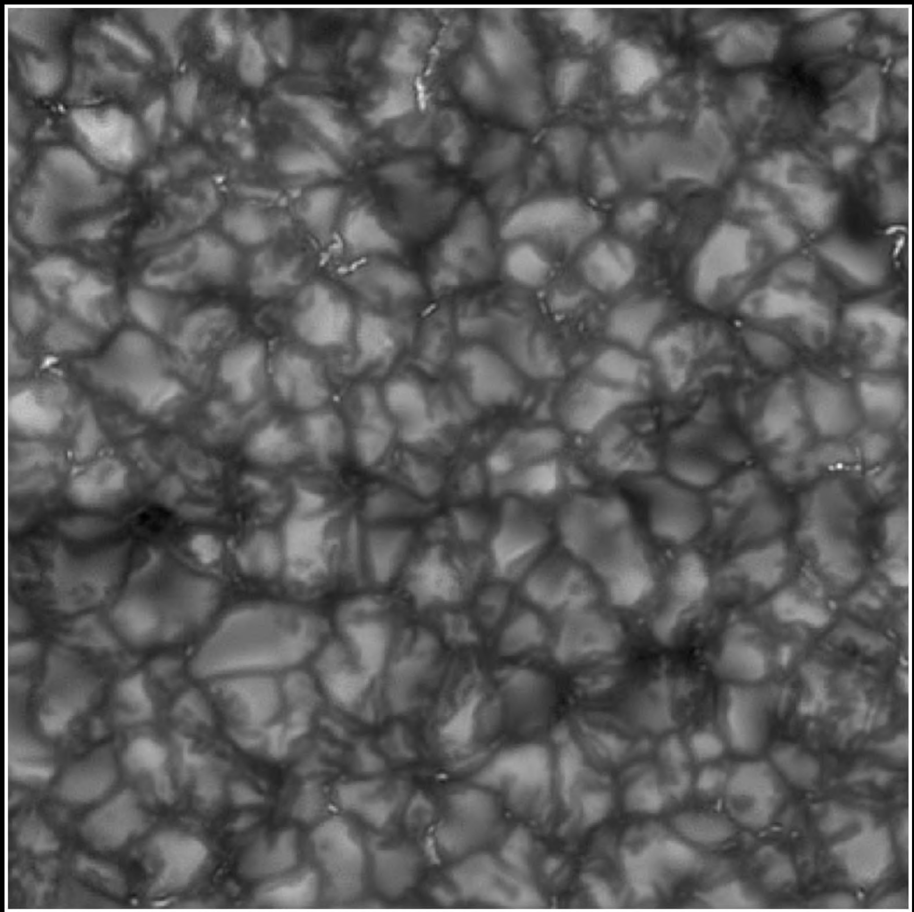

Observation of the solar surface

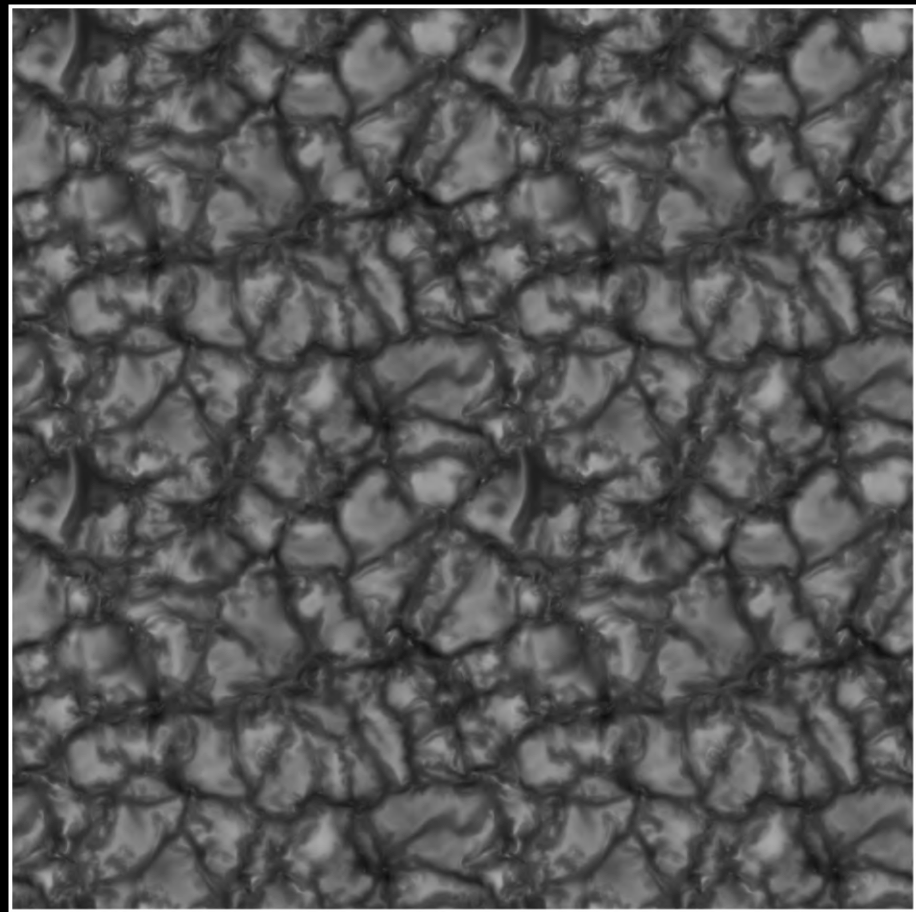

Numerical simulation

Basic postdictions (cont.)

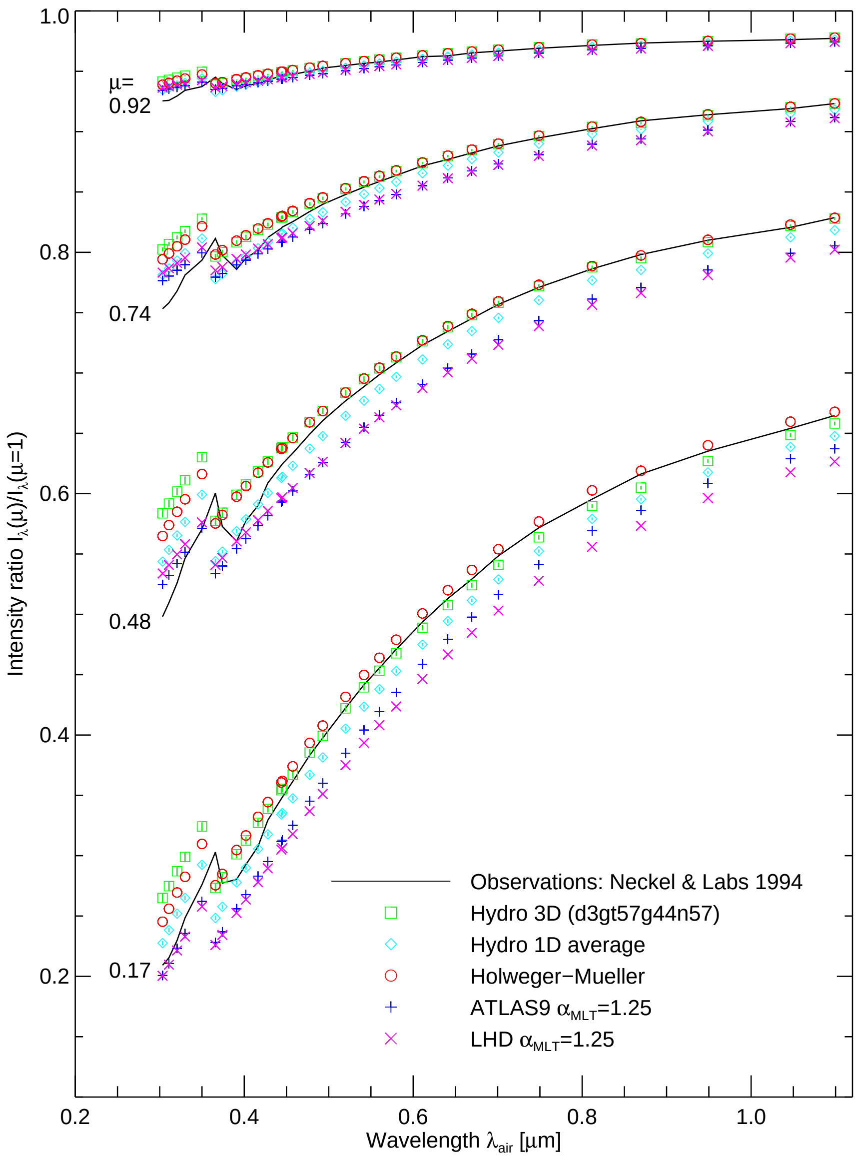

Center-to-limb intensity variation

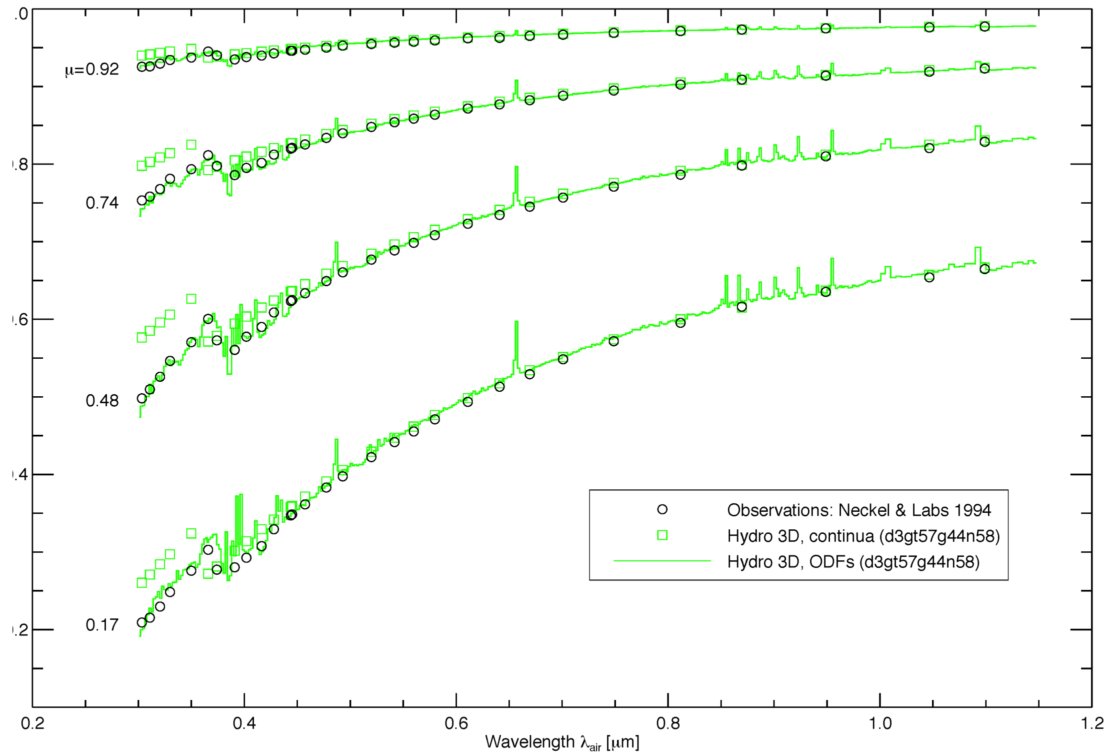

Basic postdictions (cont.)

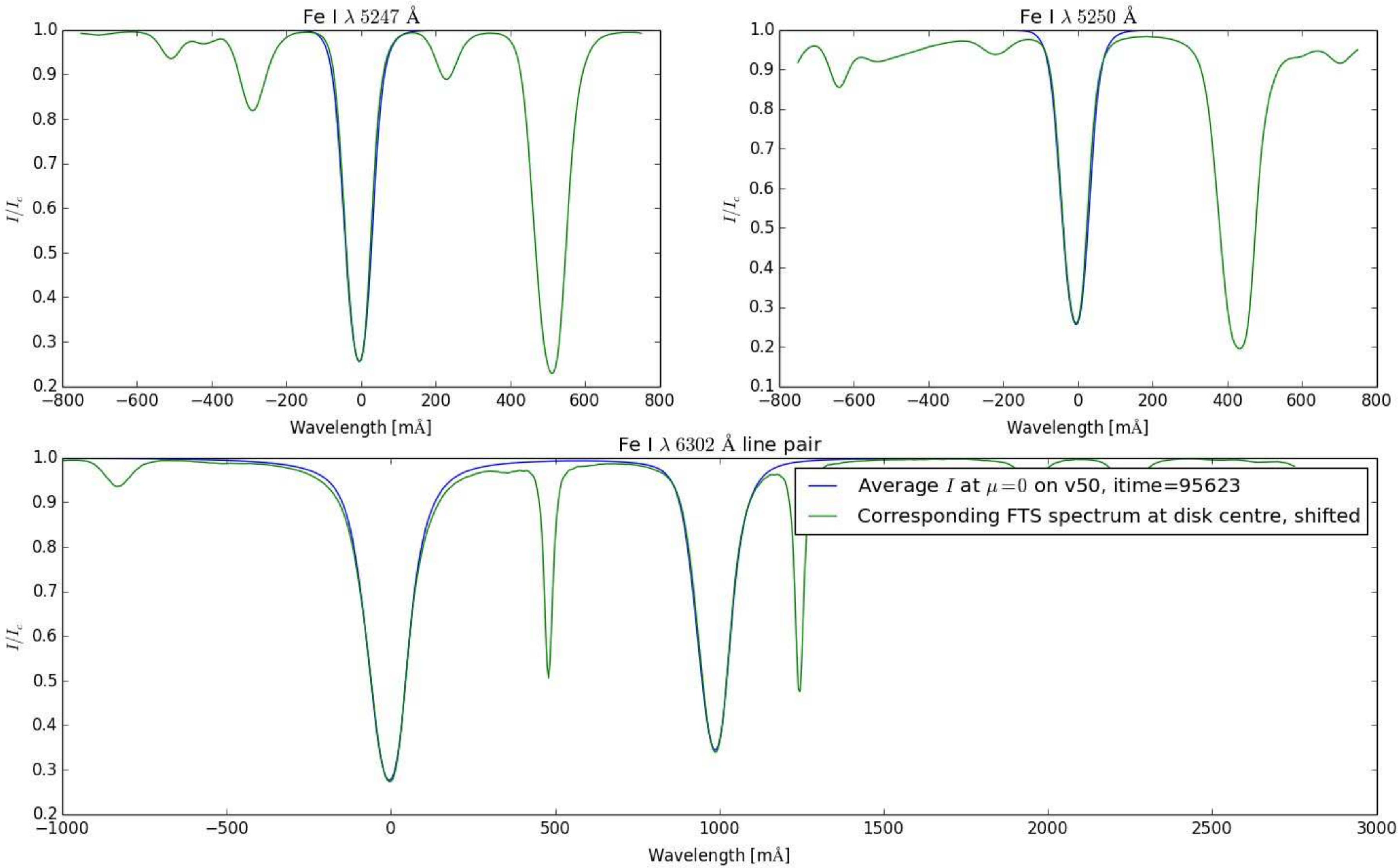

Courtesy, *F. Calvo, IRSOL*.

Synthetic Fe I spectral lines in comparison to the atlas.

§ 15 Postdiction: Stokes-V asymmetry

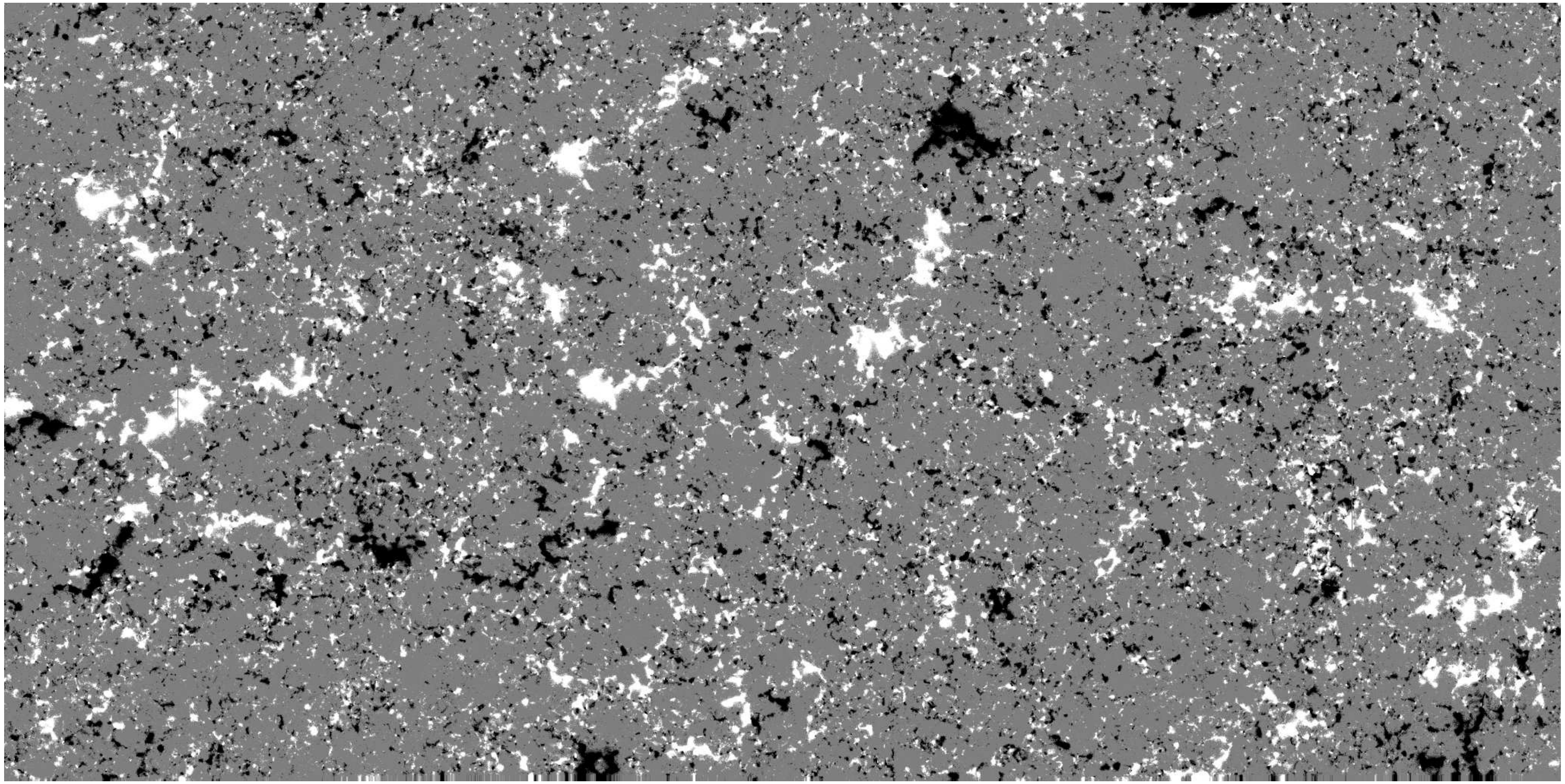

Apparent vertical magnetic flux density $B^{\mathrm{L}}_{\mathrm{app}}$ of the quiet Sun over a field of view of $302'' \times 162''$ observed from the Hinode space observatory. The grey scale saturates at ± 50 Mx cm^{-2}. 2048 steps to 5 s. From *Lites et. al. 2008, ApJ 672, 1237*

Postdiction: Stokes-V asymmetry (cont.)

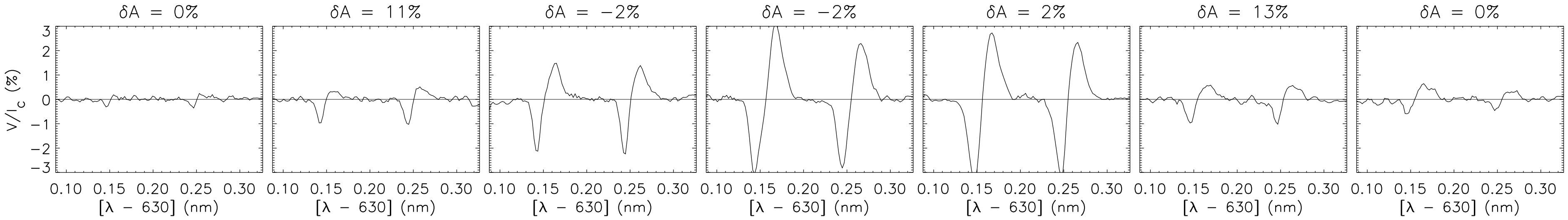

Stokes-V profiles across a magnetic element of the internetwork from the Hinode data.

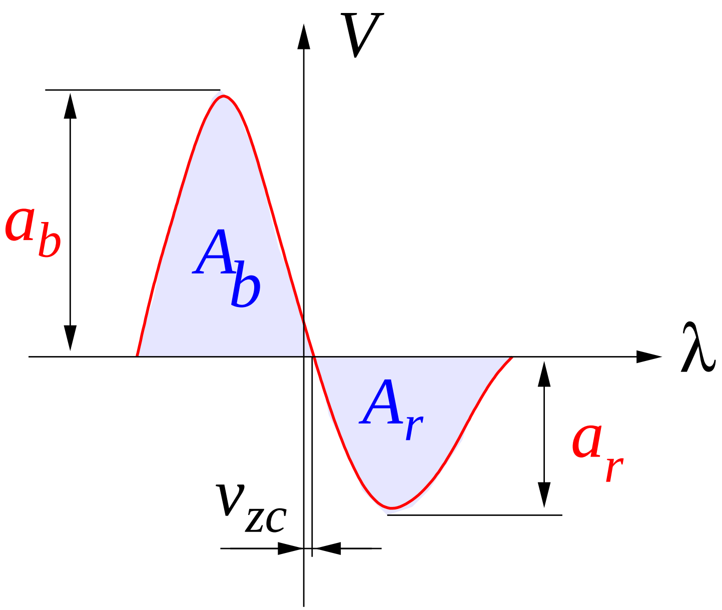

$$\delta A := \frac{A_b - A_r}{A_b + A_r}$$

$$\mathrm{sign}(\delta A) = -\mathrm{sign}\left(\frac{\mathrm{d}|B|}{\mathrm{d}\tau} \cdot \frac{\mathrm{d}v(\tau)}{\mathrm{d}\tau}\right)$$

Solanki & Pahlke, 1988; Sanchez Almeida et al., 1989

Postdiction: Stokes-V asymmetry (cont.)

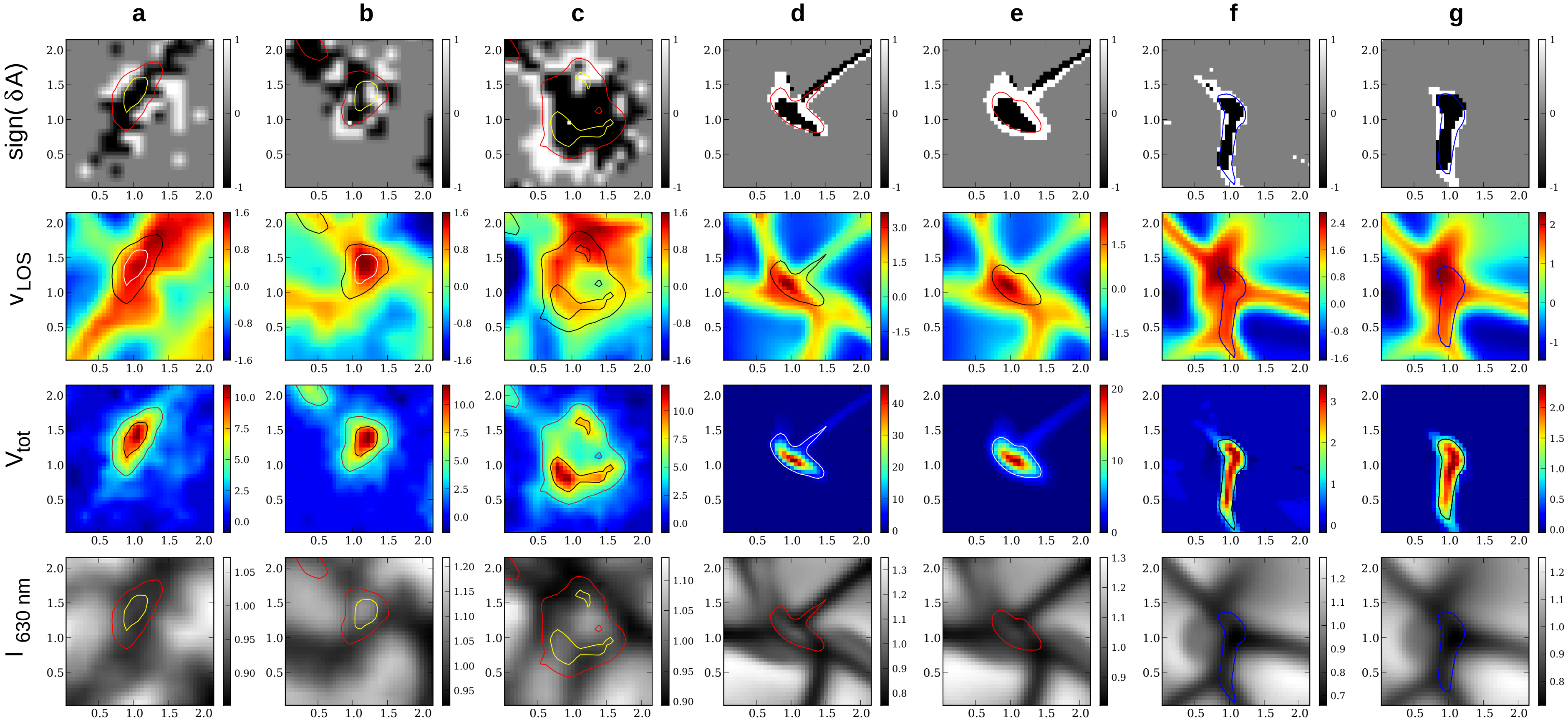

Columns a-c: observational data obtained with the spectro-polarimeter of Hinode/SOT. *Columns d and f*: synthetic data from the 3-D MHD simulation. *Columns e and g*: same as d and f but after application of the SOT-PSF to the synthetic intensity maps. Distance between tick marks is $0.5''$.

From *Rezaei, Steiner, Wedemeyer-Böhm et al. 2007, A&A 476, L33*

Postdiction: Stokes-V asymmetry (cont.)

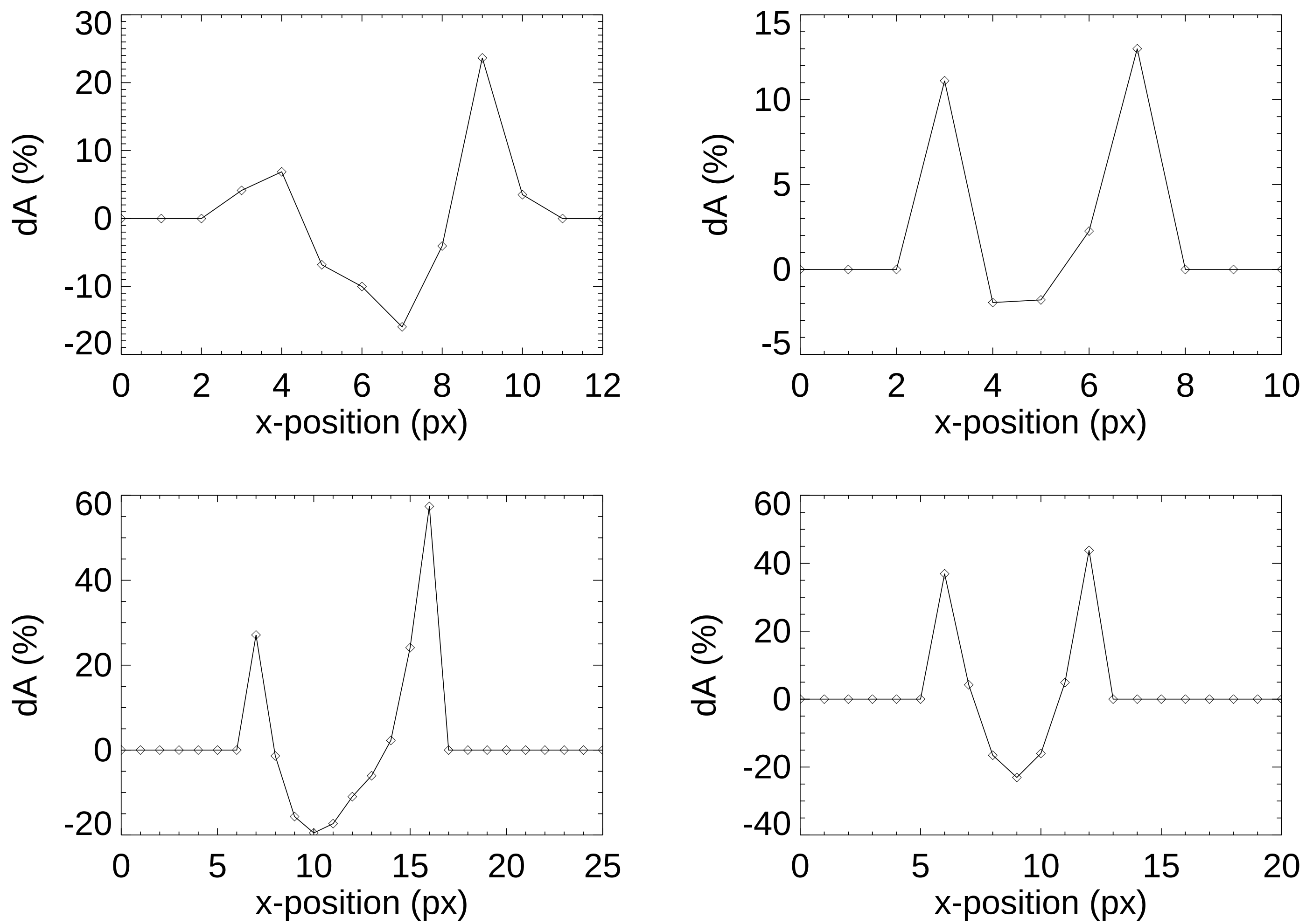

Variation in δA across magnetic elements from the Hinode data *(top row)* and the simulation *(bottom row)*.

Postdiction: Stokes-V asymmetry (cont.)

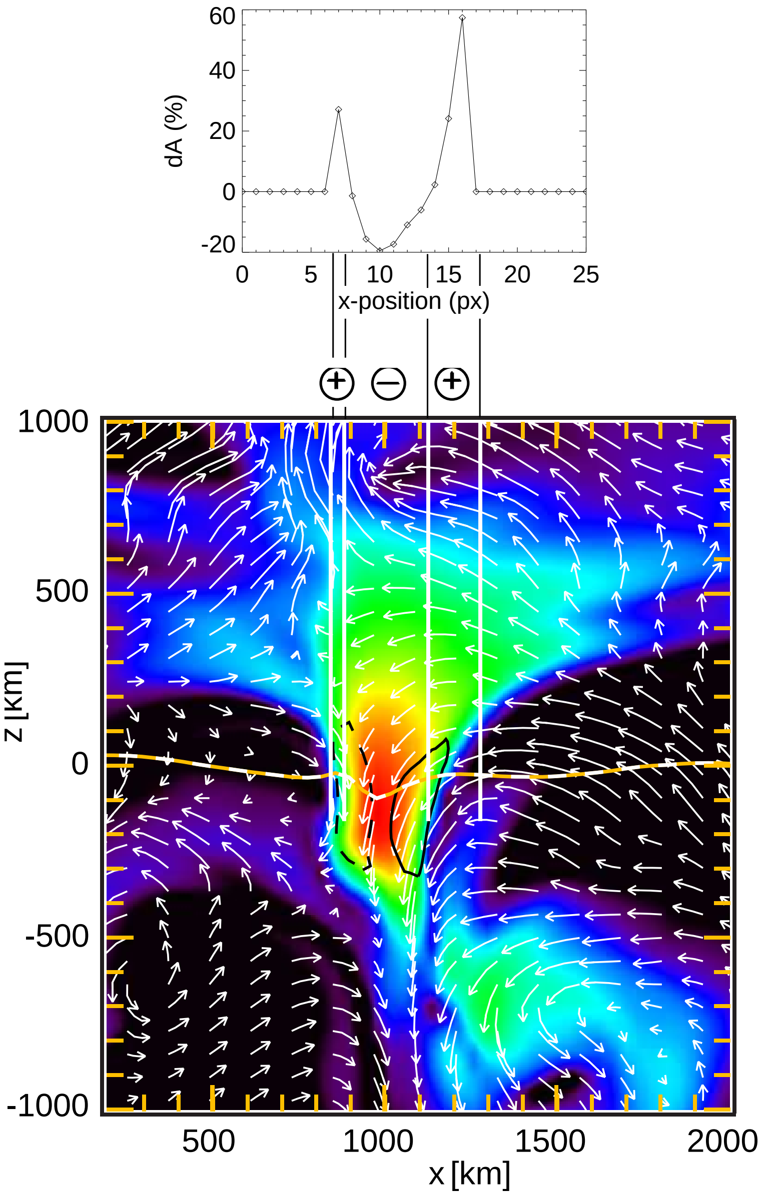

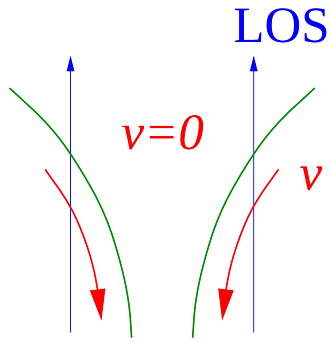

$$\left.\begin{array}{l} \dfrac{\mathrm{d}|B|}{\mathrm{d}\tau} < 0 \\ \dfrac{\mathrm{d}v(\tau)}{\mathrm{d}\tau} > 0 \end{array}\right\} \Rightarrow \delta A > 0$$

Vertical cross section through the simulation box. *Colour* displays the logarithmic magnetic field strength, *arrows* the velocity field, *black contours* the electric current density normal to the plane. The *white vertical lines* indicate ranges of either positive or negative area asymmetry, δA.

§ 16 Postdiction: Stokes-V amplitude ratio

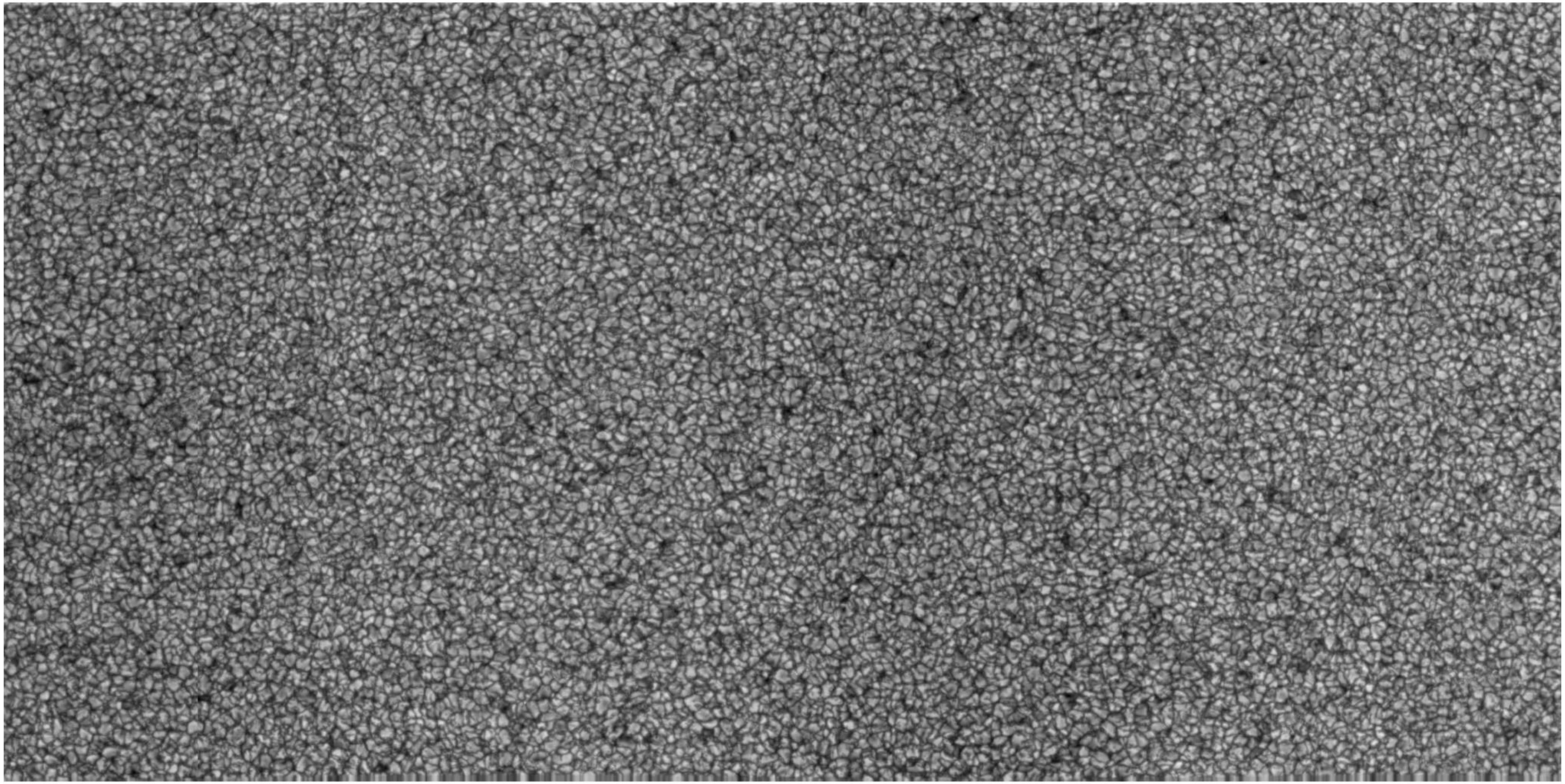

Continuum intensity at 630 nm over a field of view of $302'' \times 162''$ recorded with Hinode/SOT/SP. 2048 slit positions. From *Lites et. al. 2008, ApJ 672, 1237*

Postdiction: Stokes-V amplitude ratio (cont.)

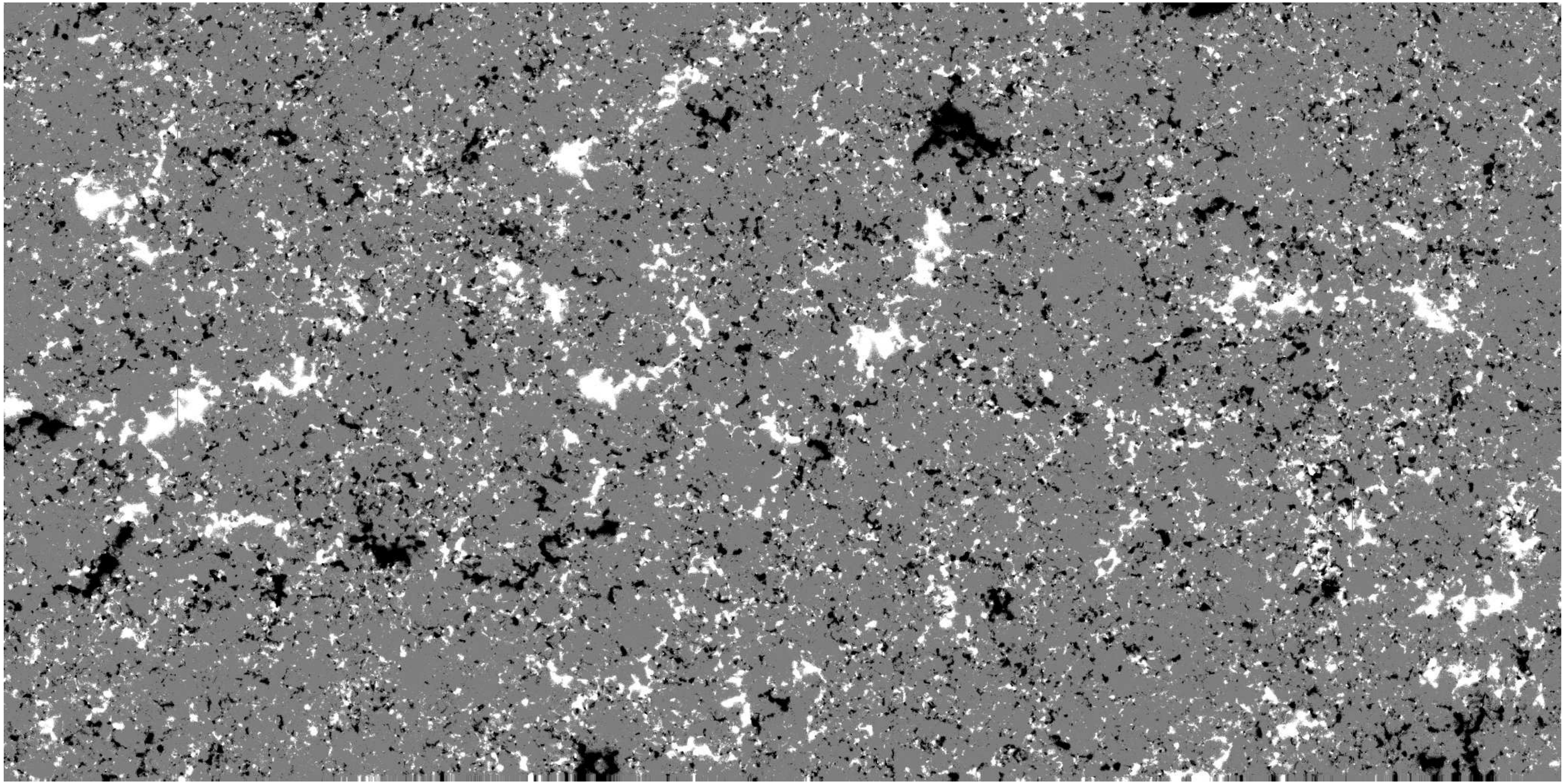

Apparent vertical magnetic flux density, $B^{\mathrm{L}}_{\mathrm{app}}$, of the quiet Sun over a field of view of $302'' \times 162''$. 2048 steps to 4.8 s. Maps of Fe I 630.15 and 630.25 nm.

From *Lites et. al. 2008, ApJ 672, 1237*

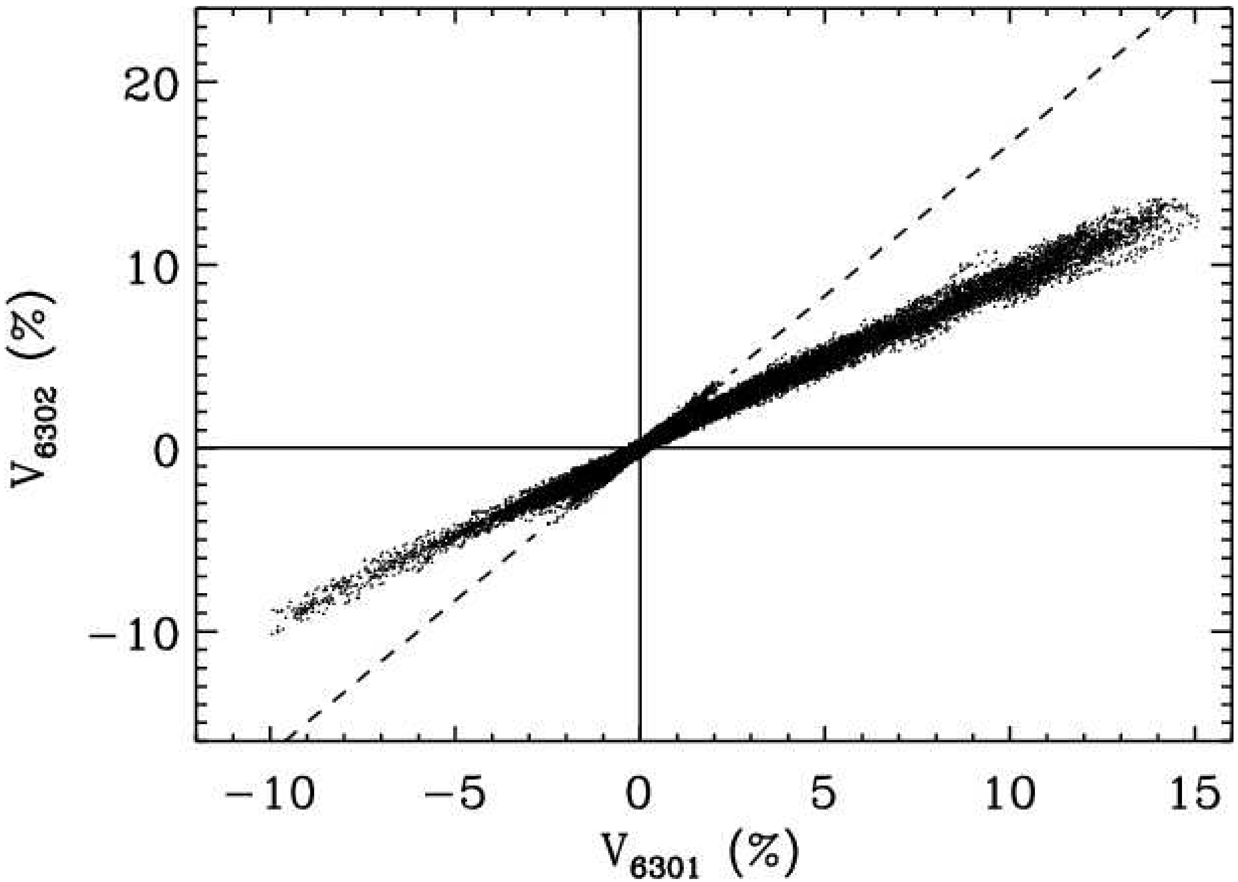

Scatter plot of the blue lobe Stokes-V amplitudes of the 6302.5 Å line vs. the 6301.5 Å line as *observed with Hinode/SOT/SP*. The dashed line is the regression relation expected for weak magnetic fields. We identify two populations of points. From *Stenflo (2011) A&A 529 A42*.

⇒ Section at 1%

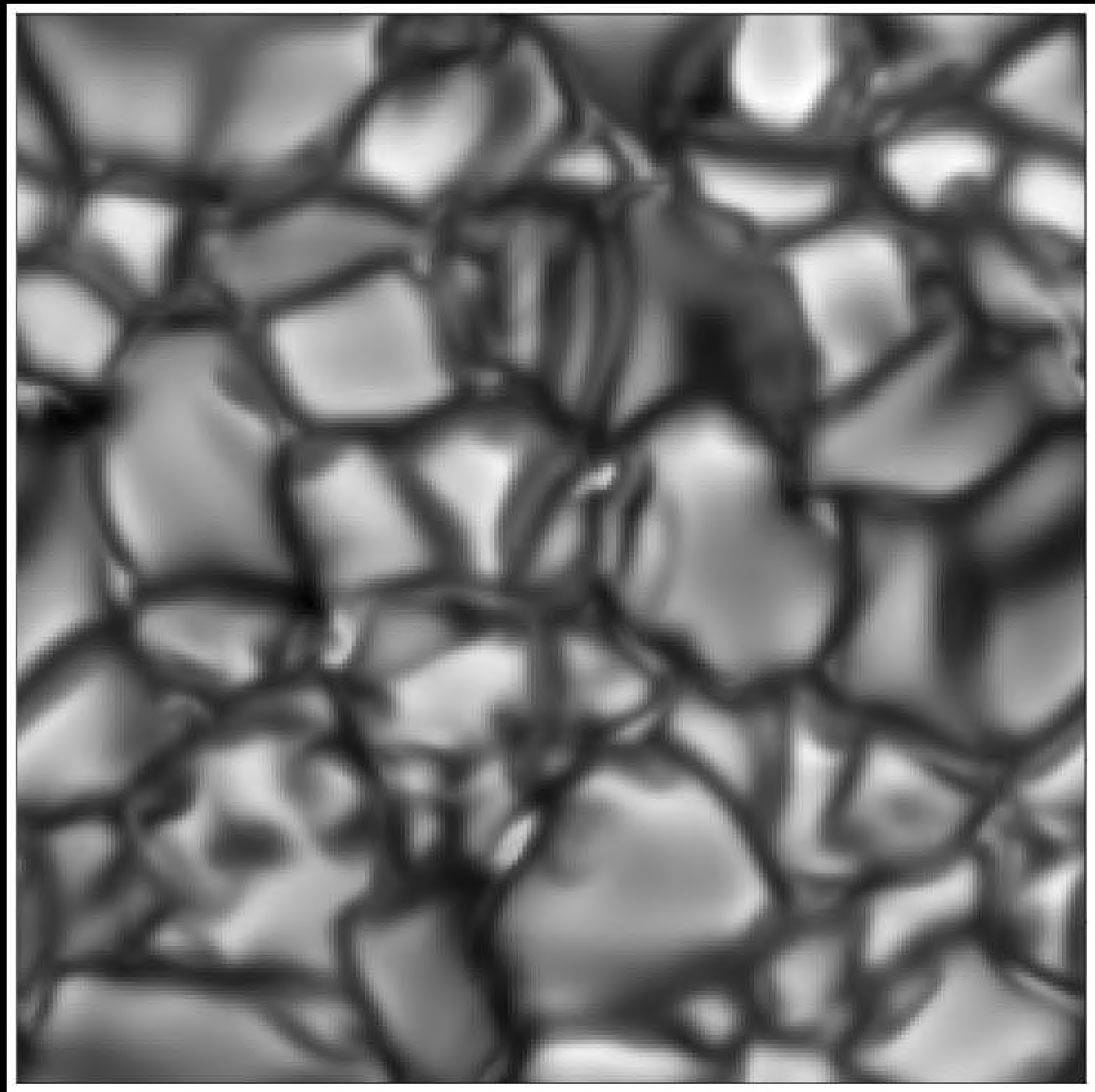

Postdiction: Stokes-V amplitude ratio (cont.): simulation data

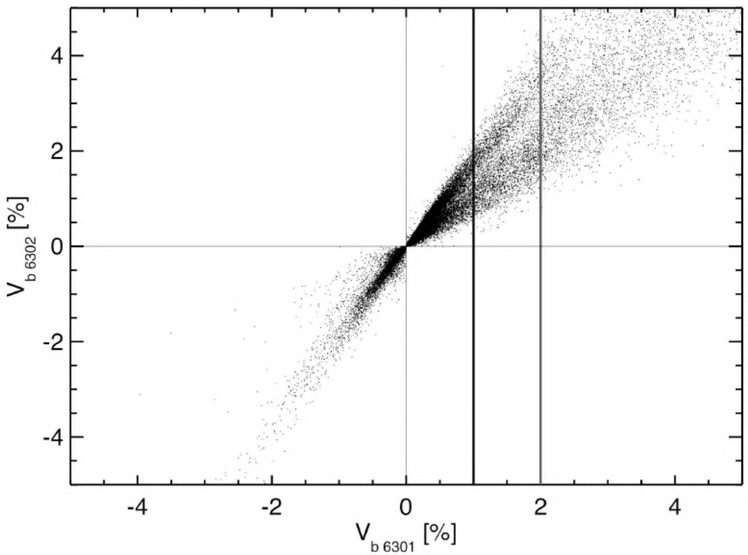

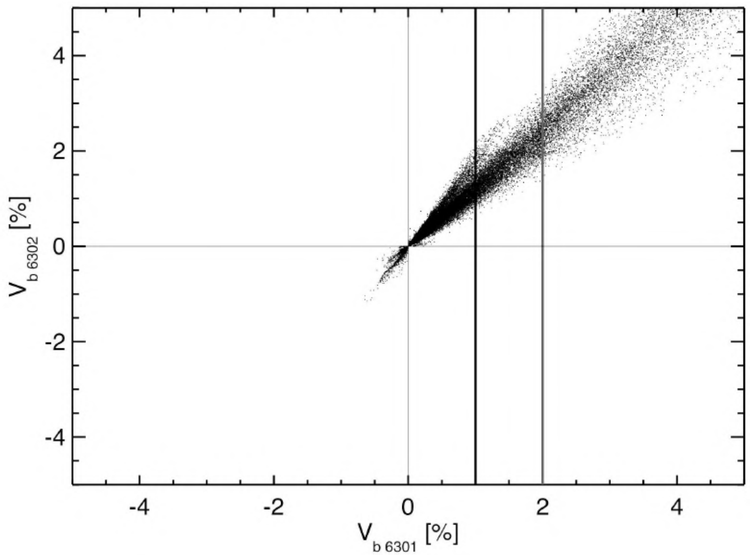

Scatter plot of the Stokes-V line ratio from the simulation. *Left:* full resolution; *Right:* degraded with the SOT/SP point spread function. From *Steiner & Rezaei (2012)*.

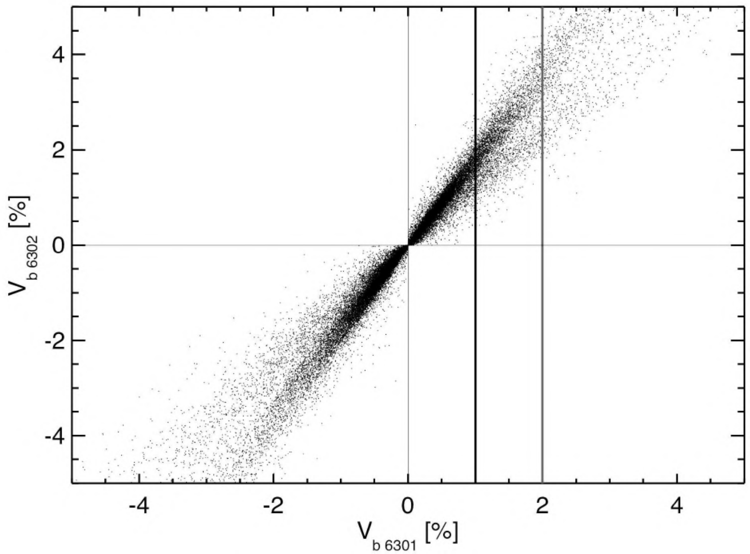

Scatter plot of the Stokes-V line ratio from a mixed polarity simulation.

“It is nice to know that the computer understands the problem, but I would like to understand it too.”

Attributed to E.P. Wigner

meaning:

“It is nice to know that our simulations reproduce the observations, but what can we learn from it?”

Postdiction: Stokes-V amplitude ratio (cont.)

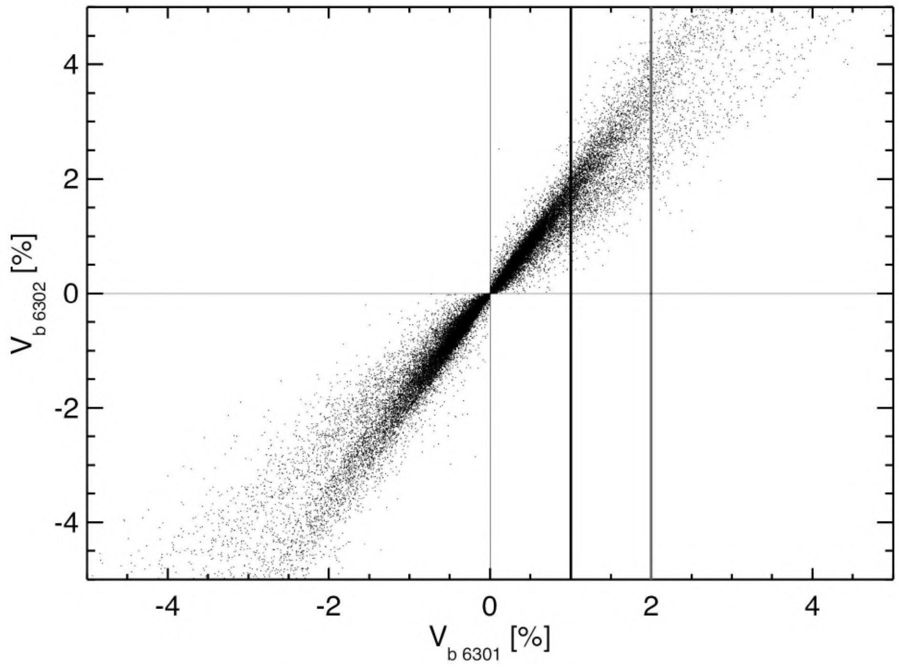

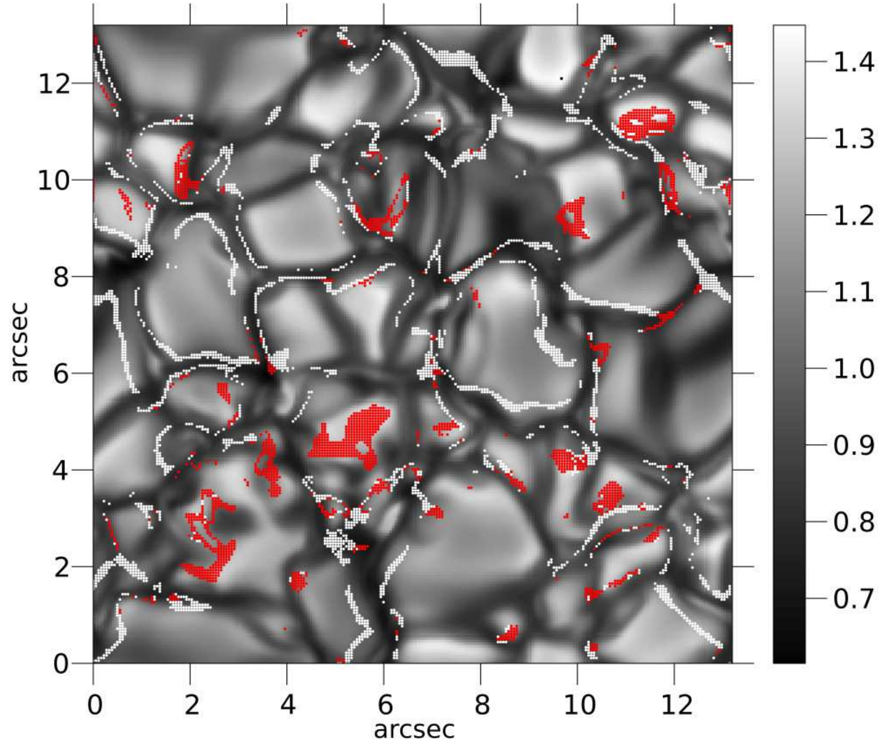

From *Steiner & Rezaei (2012)*

Conclusion: The two populations can be explained in terms of weak (hectogauss) magnetic fields. *Numerical simulations are indispensable for the correct interpretation.*

Maurizio Nannucci, Neon installation in the court of the Museo Novecento, Florence

Case studies I and II are typical examples of *post diction*: Something that was observed got *reproduced by simulations*, which helped us to better understand and interpret the observation.

The next paragraph treats an example of *prediction*.

§ 17 Prediction: Non-magnetic bright points

Bolometric intensity maps

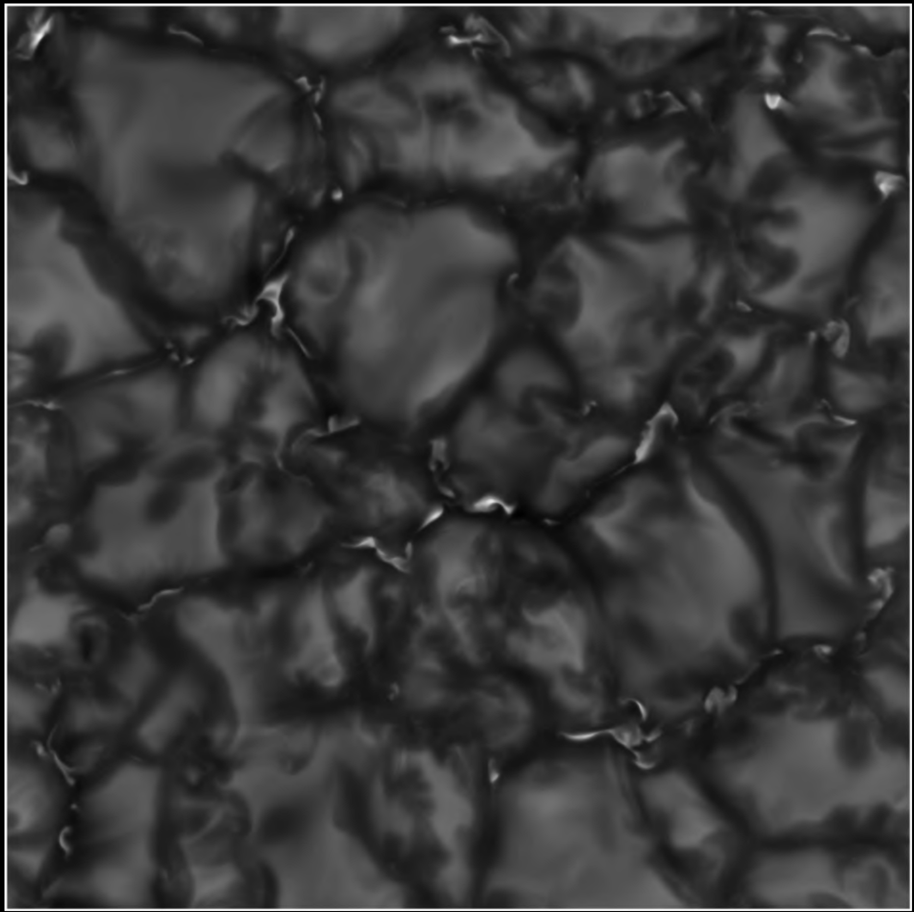

With magnetic fields:
Magnetohydrodynamic simulation

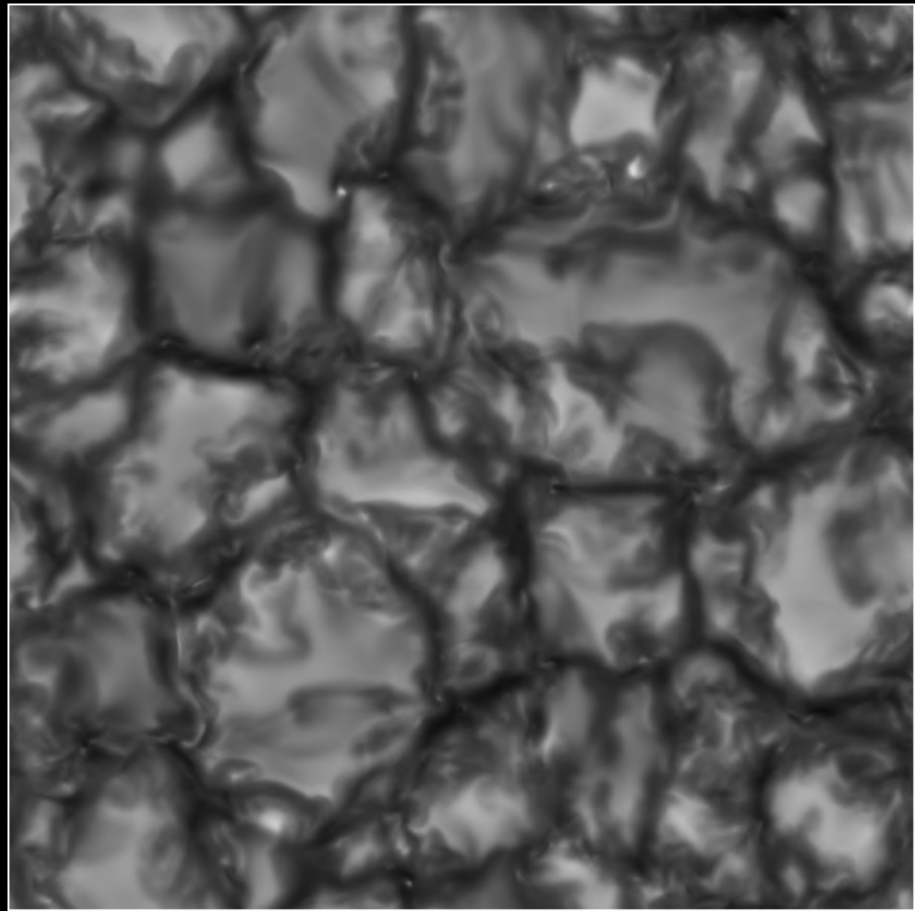

Without magnetic fields:
Hydrodynamic simulation

Computations: *Centro Svizzero di Calcolo Scientifico*

Courtesy,
F. Calvo

Slices across a non-magnetic bright point (nMBP0868)

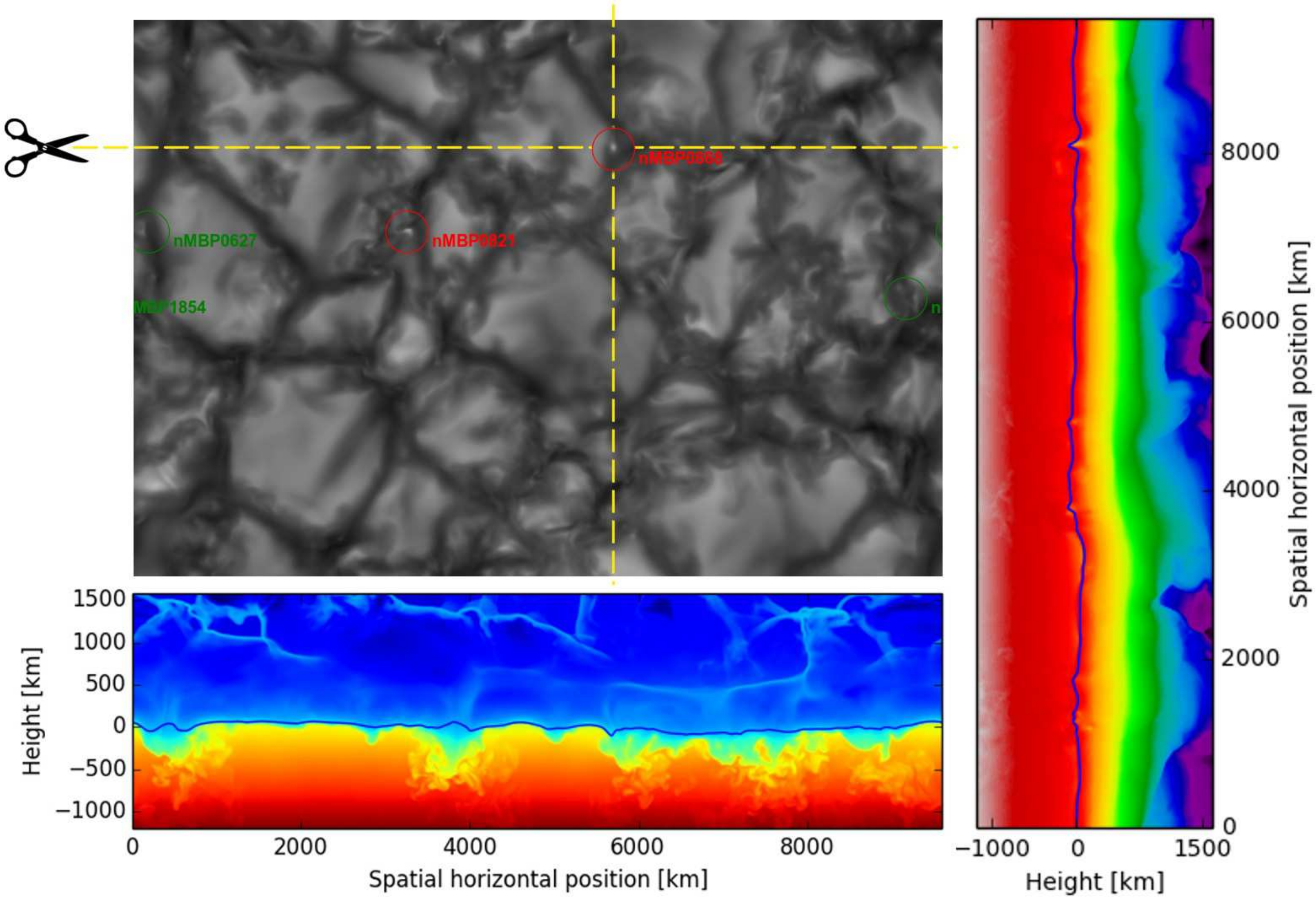

Courtesy, *F. Calvo, IRSOL.*

Emergent intensity I (*top left*), temperature T (*bottom*), density $\log(\rho)$ (*right*)

Prediction: Non-magnetic bright points (cont.)

Slices across a non-magnetic bright point (nMBP0868)

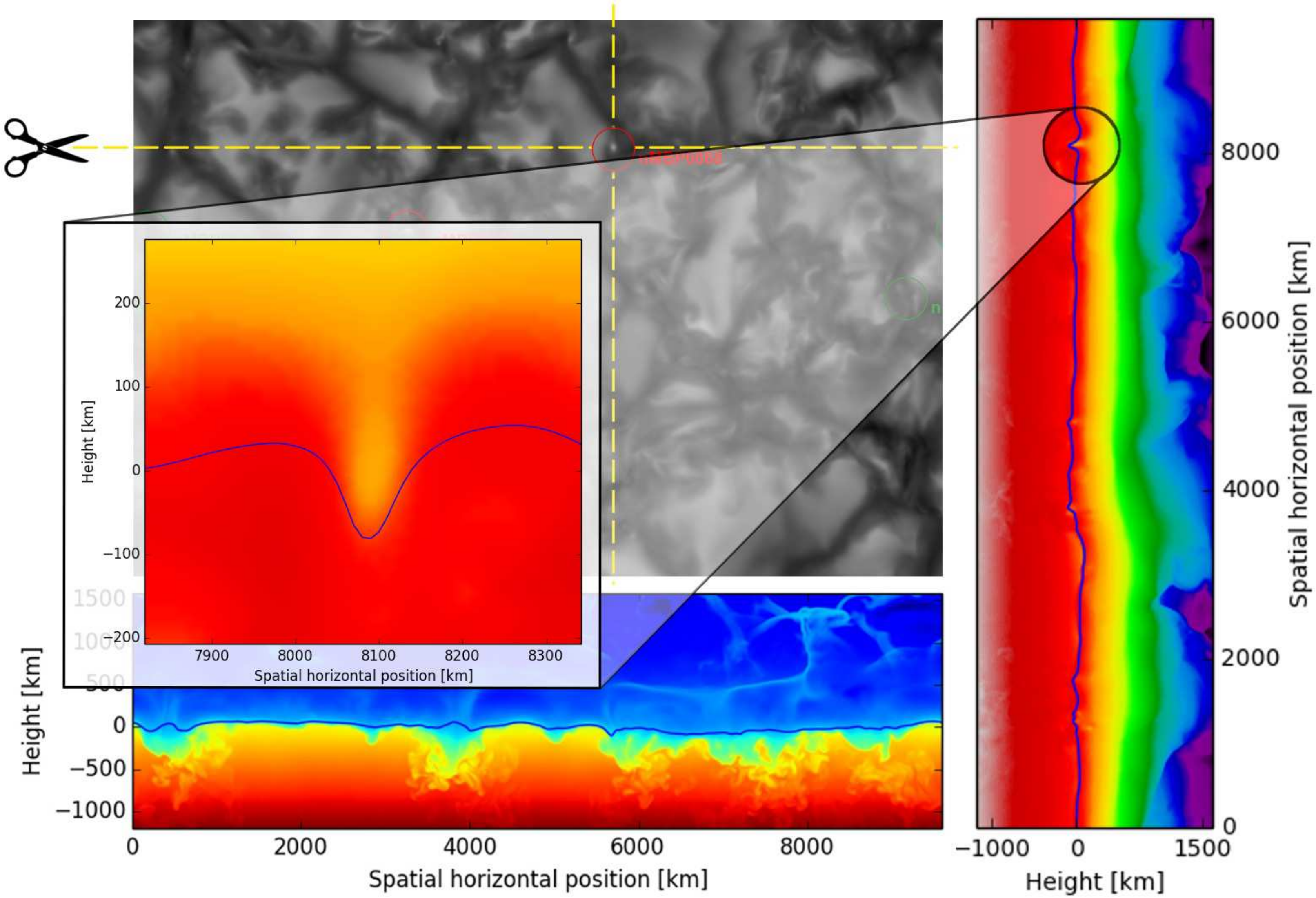

Courtesy, *F. Calvo, IRSOL.*

Emergent intensity I (*top left*), temperature T (*bottom*), density $\log(\rho)$ (*right*)

Prediction: Non-magnetic bright points (cont.)

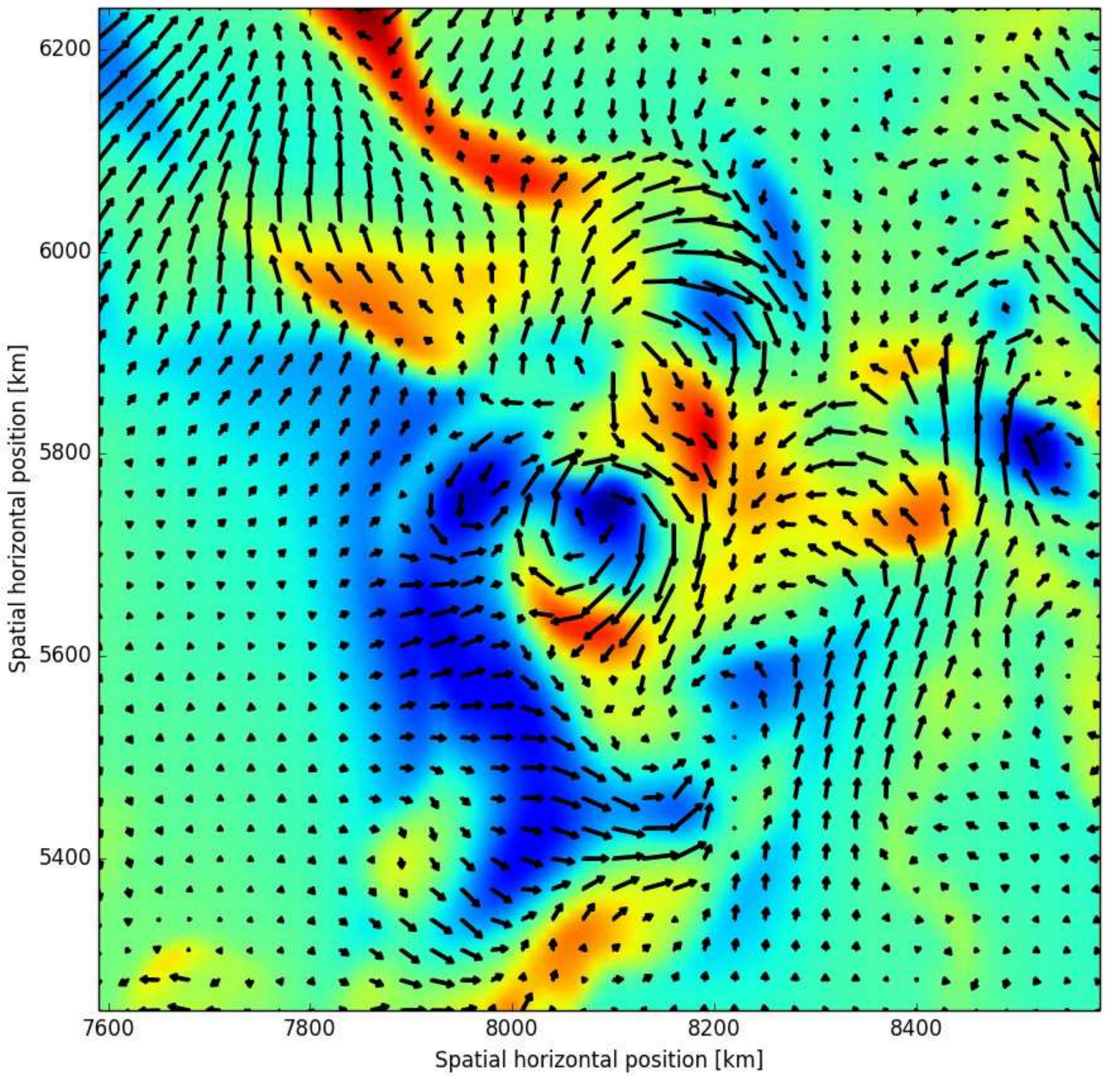

non-magnetic bright points (nMBPs) are locations with:

- *swirling motion* (but ≈ 150 [km] below $\tau = 1$ there are often swirls that do not produce nMBPs);
- *low density* (but a density deficiency alone does not warrant nMBP's);
- *high intensity contrast* (but a local intensity peak does not need to be a nMBP).

Density (blue: low, red: high) and velocity field in an horizontal plane, 150 [km] below $\langle \tau \rangle = 1$

From *F. Calvo et al. 2016*.

Prediction: Non-magnetic bright points (cont.)

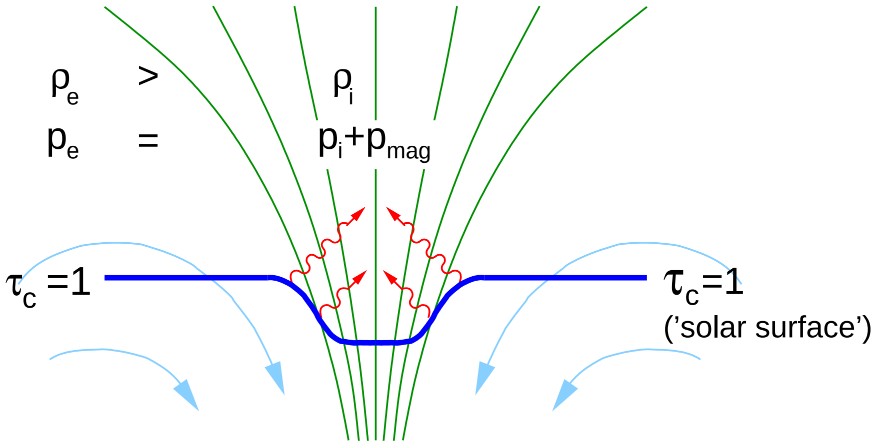

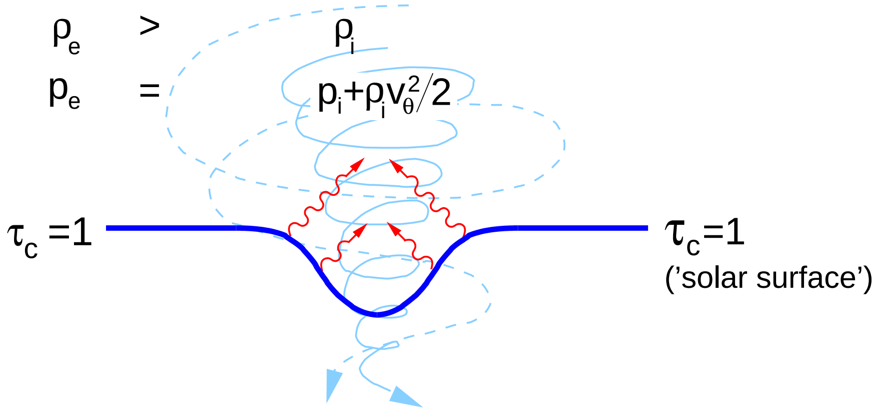

Magnetic flux sheet. Depression due to magnetic pressure.

Swirl. Depression due to centrifugal force.

In both cases is the 'hot wall effect' responsible for the enhanced radiation from the depression.

Prediction: Non-magnetic bright points (cont.)

Reduction to an analytical toy model

Starting from the momentum equation

$$\frac{\partial \boldsymbol{v}}{\partial t} + (\boldsymbol{v} \cdot \boldsymbol{\nabla})\, \boldsymbol{v} + \frac{1}{\rho} \boldsymbol{\nabla} P + \boldsymbol{g} = 0\,,$$

we assume

1. nMBPs are long-lived and stable so that the velocity field can be considered stationary;
2. They have cylindrical symmetry;
3. Their velocity field has a non-vanishing azimuthal component;
4. They extend in the vertical direction and their shape does not depend on depth.

Because of 2., the Euler momentum equation can be written in cylindrical coordinates.

Reduction to an analytical toy model

The advection term is then given by

$$(\boldsymbol{v}\cdot\boldsymbol{\nabla})\boldsymbol{v} = \left[(\boldsymbol{v}\cdot\boldsymbol{\nabla})v_r - \frac{v_\theta^2}{r}\right]\hat{\boldsymbol{r}} + \left[(\boldsymbol{v}\cdot\boldsymbol{\nabla})v_\theta + \frac{v_\theta v_r}{r}\right]\hat{\boldsymbol{\theta}} + (\boldsymbol{v}\cdot\boldsymbol{\nabla})v_z\hat{\boldsymbol{z}}\,,$$

where the directional derivative is

$$\boldsymbol{v}\cdot\boldsymbol{\nabla} = v_r\partial_r + \frac{v_\theta}{r}\partial_\theta + v_z\partial_z\,.$$

The simplest field satisfying the conditions 1–4 is $\boldsymbol{v} = v_\theta\,(r)\,\hat{\boldsymbol{\theta}}$. Inserting it into the Euler momentum equation and projecting it into the horizontal plane yields

$$\frac{\partial P}{\partial r} - \rho\frac{v_\theta^2}{r} = 0\,.$$

The pressure gradient is provided by the centripetal force.

Reduction to an analytical toy model

One can then estimate the magnitude of v_θ. With

$$\frac{P_{\rm ext}-P_{\rm int}}{\rho_{\rm ext}} \approx v_\theta^2 \,, \qquad \frac{\rho_{\rm int}-\rho_{\rm ext}}{\rho_{\rm ext}} \equiv C_\rho \,, \quad \frac{T_{\rm int}-T_{\rm ext}}{T_{\rm ext}} \equiv C_T \,,$$

$$\frac{P_{\rm ext}}{\rho_{\rm ext}} \approx R_{\rm s}\, T_{\rm ext} \,, \qquad T_{\rm ext} \approx T_{\rm eff} \,,$$

one obtains with $C_\rho \approx -0.5$ and $C_T \approx 0$

$$v_\theta = \sqrt{R_{\rm s}\, T_{\rm eff}\, [1-(1+C_\rho)(1+C_T)]} \approx \sqrt{\frac{R_{\rm s}\, T_{\rm eff}}{2}} = 4.4\,\text{km s}^{-1} \,,$$

while the maximum azimuthal velocities in the simulation are $v_\theta^{\rm max} \approx 6\,{\rm kms}^{-1}$.

Prediction: Non-magnetic bright points (cont.)

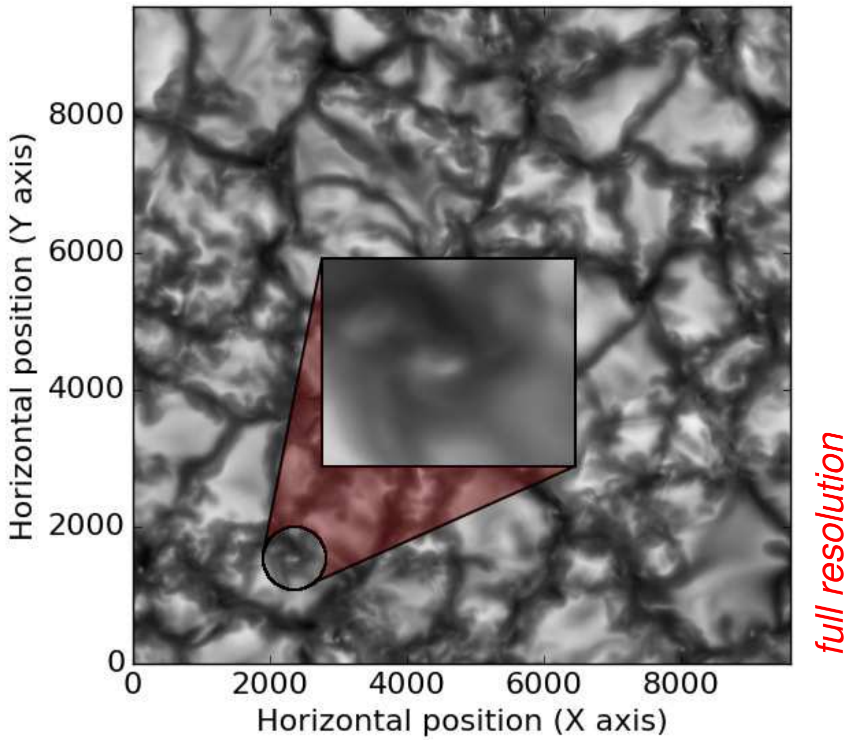

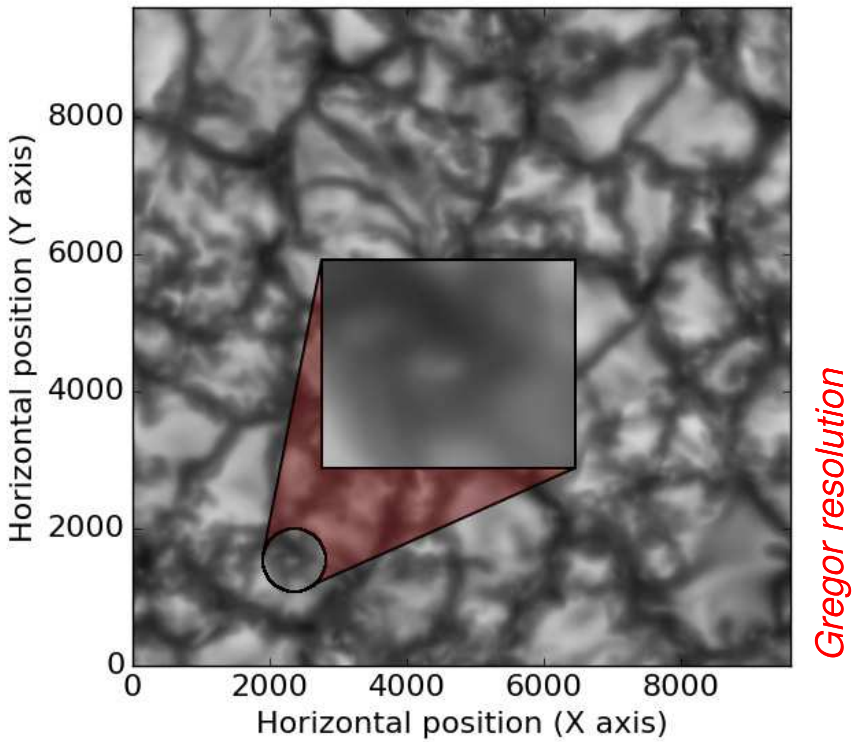

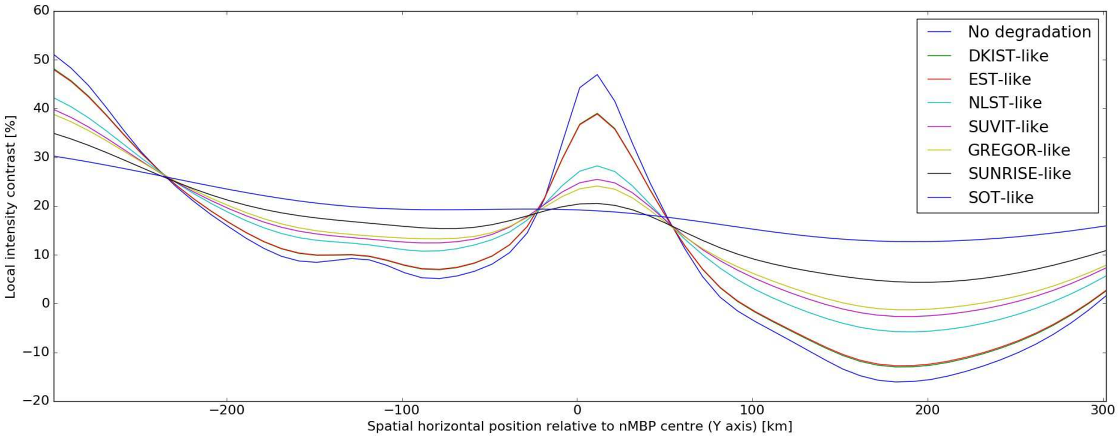

Intensity contrast across a non-magnetig bright point as observed with different telescopes.

From *Calvo et al. (2016)*.

§ 18 Prediction: Stellar photometric variability

K8V

K2V

G2V

F5V

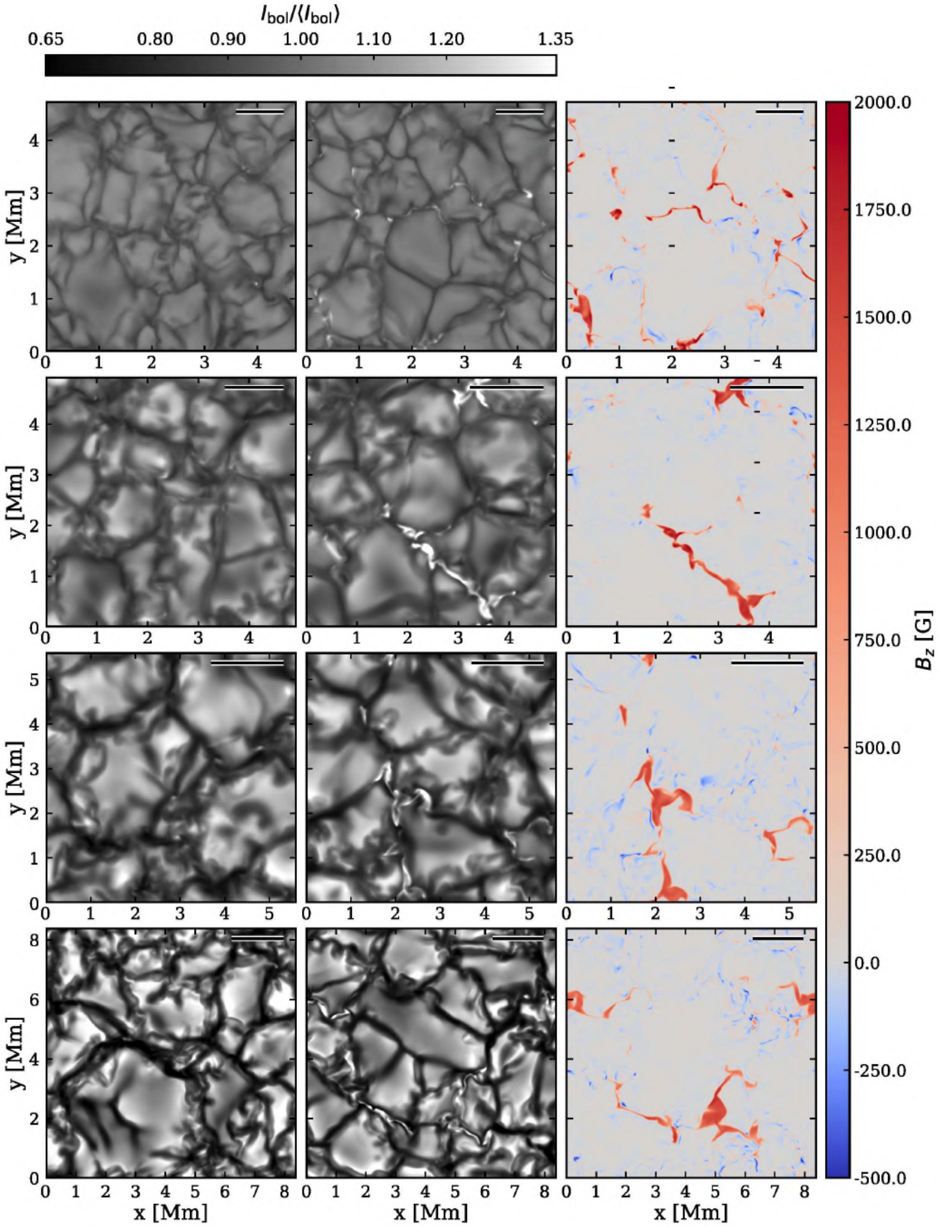

- *"Box in a star" simulations* of the surface layers of four spectral types;
- Each simulation is *run twice* : with and without magnetic fields;
- Initial vertical homogeneous field of *50 G* and *100 G* ;
- Multi-group *radiation transfer* using 5 opacity bins;
- Numerical, non-stationary, three-dimensional radiation magnetohydrodynamics using the *CO^{5}BOLD code*.

Prediction: Stellar photometric variability (cont.)

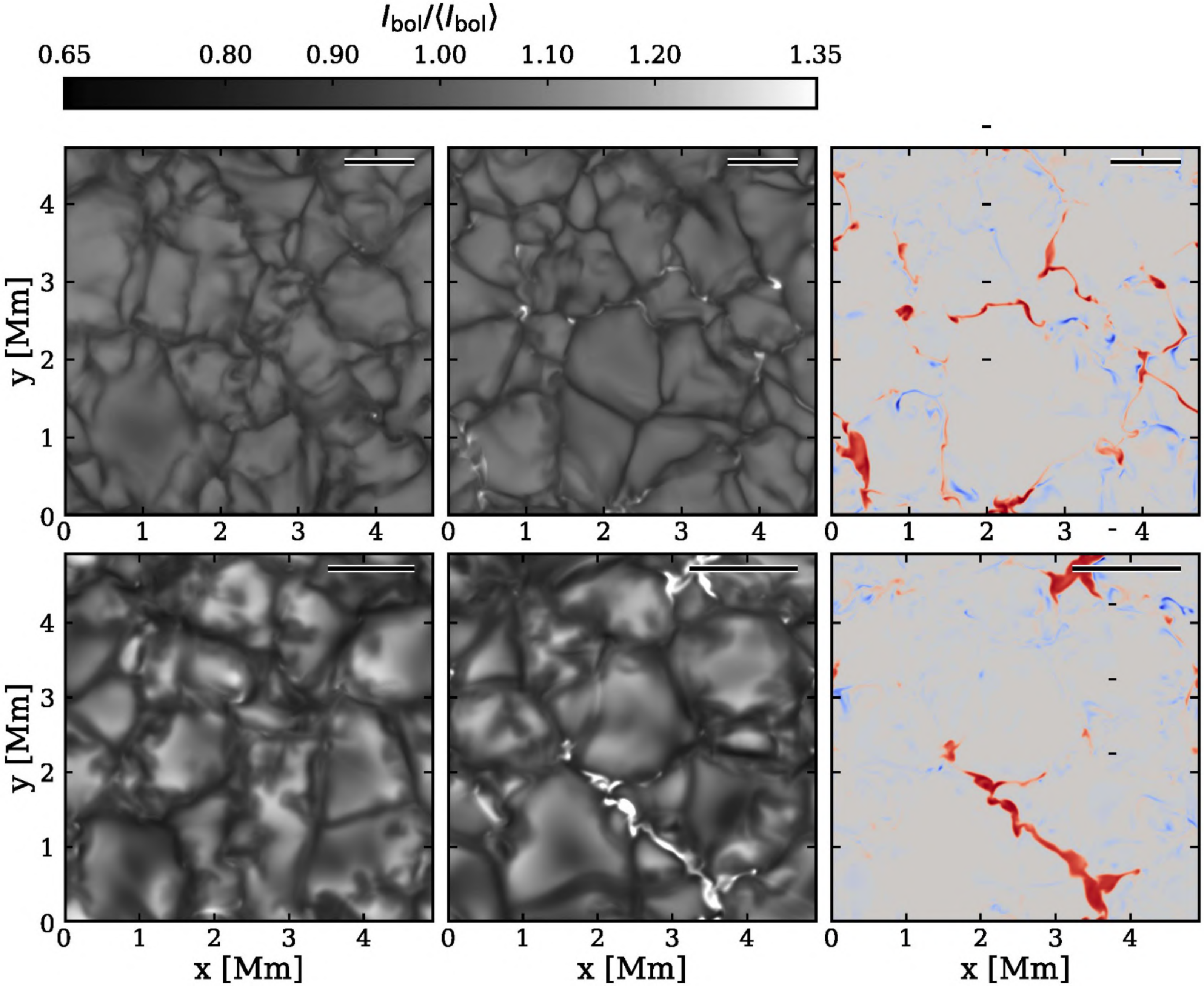

K8V

$c_{\mathrm{bol\,rms}} =$ 5.6 %

B0, v50

K2V

$c_{\mathrm{bol\,rms}} =$ 9.8 %

B0, v50

From *Salhab et al. (2017)*

Prediction: Stellar photometric variability (cont.)

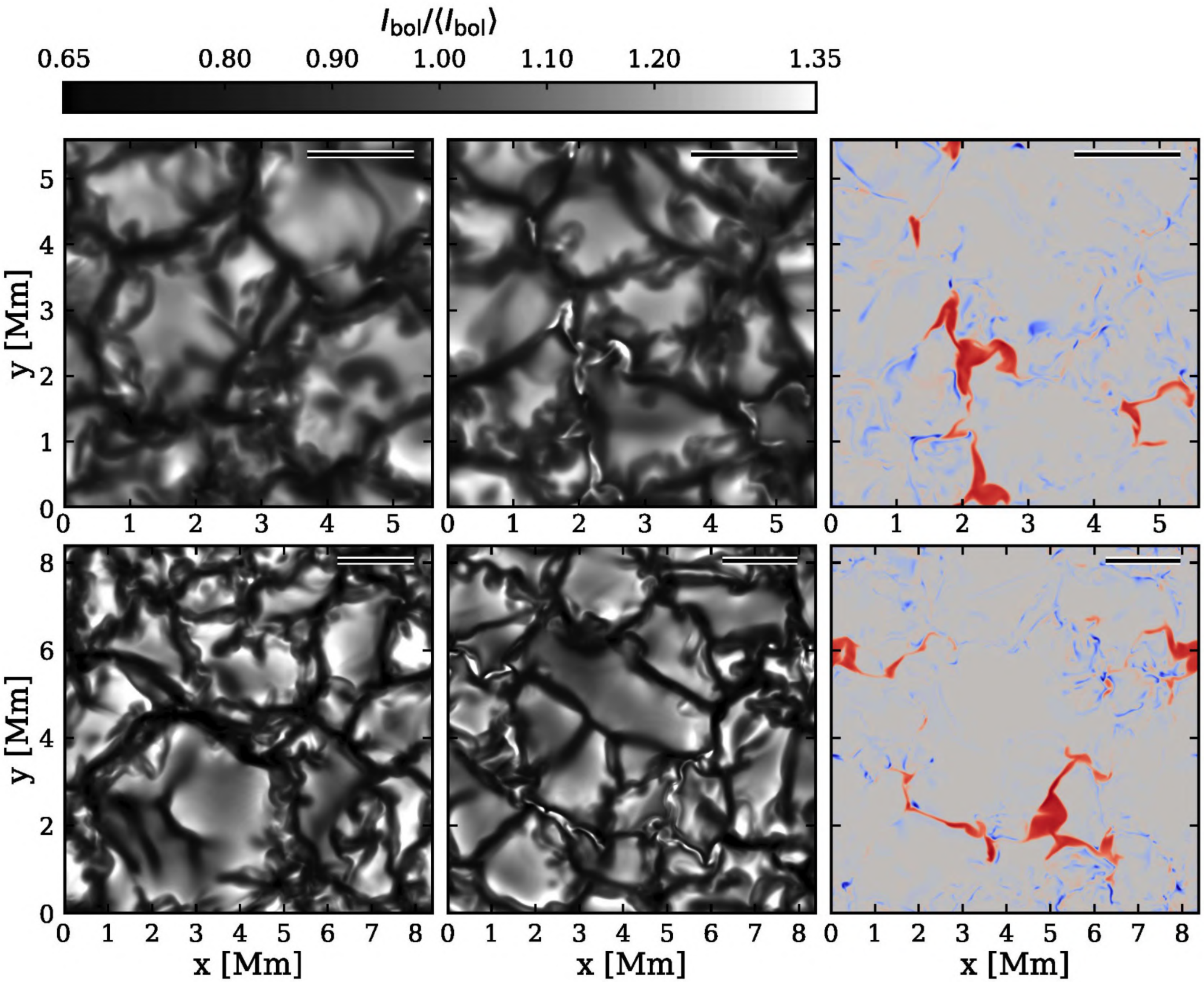

G2V

$c_{\rm bol\,rms} =$ 15.3 %

B0, v50

F5V

$c_{\rm bol\,rms} =$ 18.7 %

B0, v50

From *Salhab et al. (2017)*

Prediction: Stellar photometric variability (cont.)

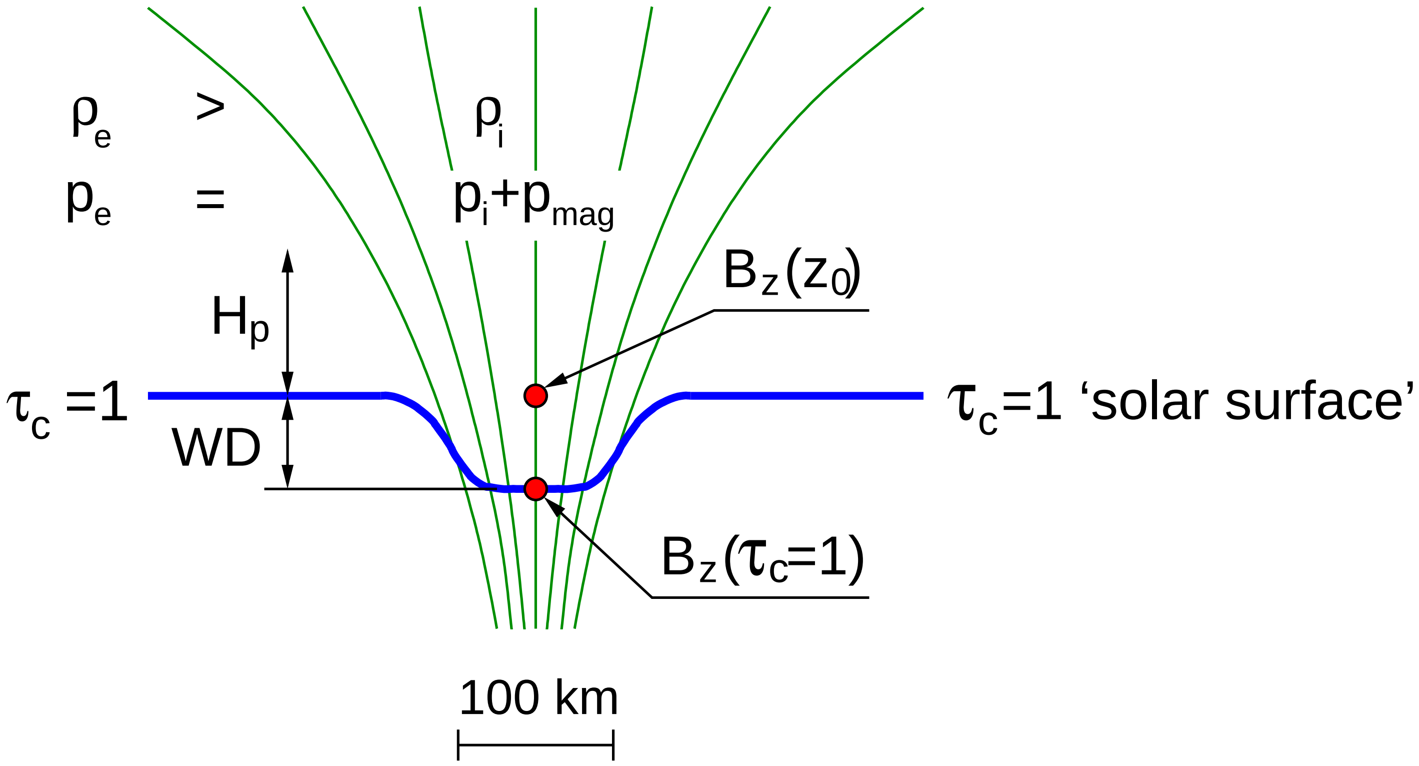

Magnetic flux concentration *(green)* with optical surface $\tau_c = 1$ *(blue)*, and "Wilson depression" WD.

Conclusion: $B_z(\tau_\mathrm{R} = 1) \approx 1550$ [G] is fairly *independent of spectral type*

Prediction: Stellar photometric variability (cont.)

Magnetic flux sheath in a

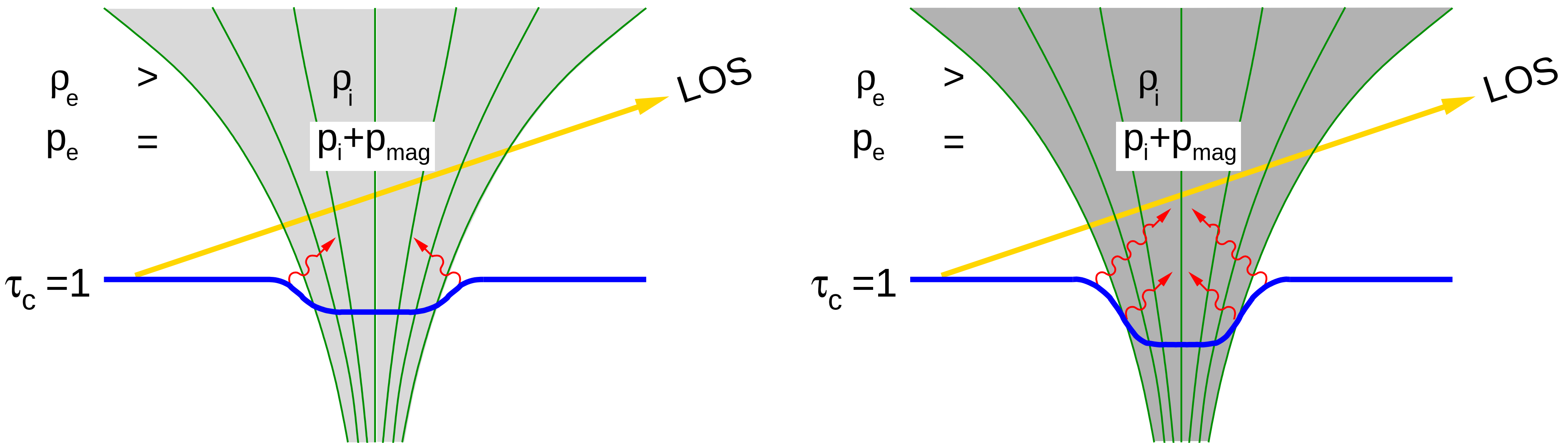

K-type atmosphere

G-type atmosphere.

Small depression of the $\tau_c = 1$ surface

$\Rightarrow$ *weak hot-wall effect*.

Weak evacuation

$\Rightarrow$ *faint facular granules*.

Large depression of the $\tau_c = 1$ surface

$\Rightarrow$ *strong hot-wall effect*.

Strong evacuation

$\Rightarrow$ *bright facular granules*.

Prediction: Stellar photometric variability (cont.)

	spectral type	K8V	K2V	G2V	F5V
	initial B_z [G]	50	50	50	50
25	$\delta_{I_{\rm bol}}$ [%]	0.25 $\pm$0.2	0.68 $\pm$0.9	0.88 $\pm$1.1	0.53 $\pm$0.8
26	$\delta_{F_{\rm bol}}$ [%]	*0.39* $\pm$0.2	*0.86* $\pm$0.9	*1.15* $\pm$1.1	*0.95* $\pm$0.8
27	$\delta_{F_{\rm bol}} - \delta_{I_{\rm bol}}$ [%]	0.14	0.18	0.27	0.42
30	$\mathrm{WD_w}$ [km]	60 $\pm$14	139 $\pm$34	232 $\pm$65	388 $\pm$113
31	$\mathrm{WD_w}/H_p(\tau_R = 1)$ [-]	0.7 $\pm$0.1	1.3 $\pm$0.3	1.4 $\pm$0.3	2.6 $\pm$0.7
15	$\rho_{\rm int}/\rho_{\rm ext}(z_0)$ [-]	0.75 $\pm$0.02	0.54 $\pm$0.03	0.46 $\pm$0.04	0.36 $\pm$0.05
16	$\beta(z_0)$ [-]	2.7 $\pm$0.2	1.3 $\pm$0.1	0.74 $\pm$0.1	0.38 $\pm$0.1

Radiative surplus of the magnetic over the field-free models, weighted mean *Wilson depression*, and degree of *evacuation* of the flux concentrations.

Conclusion: For spectral types K8V to F5V, the small-scale magnetic fields produce a *surplus in radiative intensity and flux*. It is most pronounced for G-type and early K-type stars.

In the last two examples, numerical simulations served to make a *prediction*. Because the simulations faithfully reproduce observed features like granules, the granular rms intensity contrast, or the shape of spectral lines, we can with some confidence predict new features, like swirling non-magnetic bright points, to really exist on the Sun. The complex structure of the non-magnetic bright points found in the simulations got *reduced to an analytical toy model*.

The next paragraph treats an example of *virtual experimentation*. Since we cannot take the Sun in the laboratory and since we cannot travel to the Sun and cary out experiments in situ, we reconstruct it in the computer for carrying out experiments.

§ 19 Experiment: MHD wave conversion

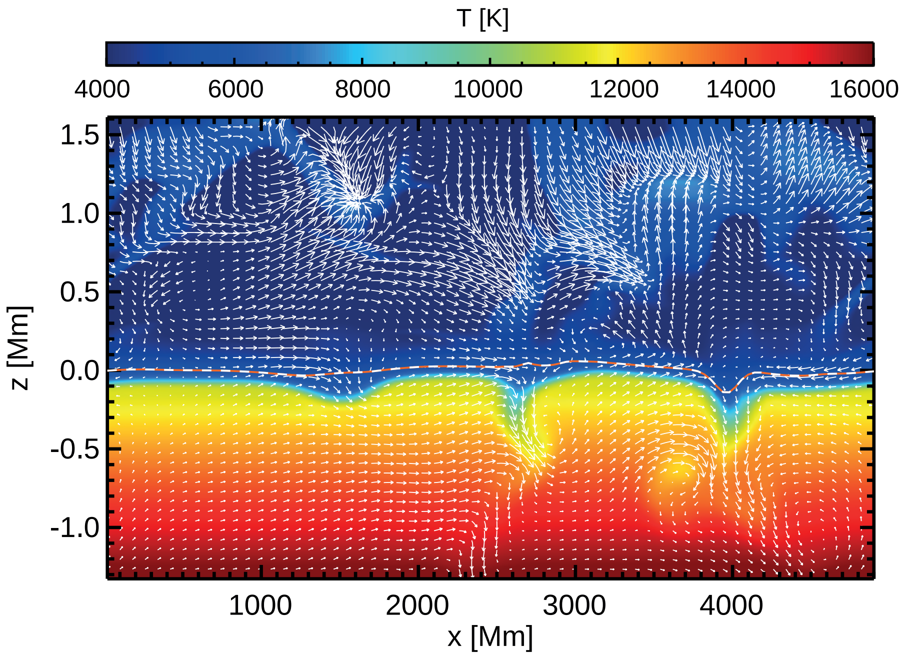

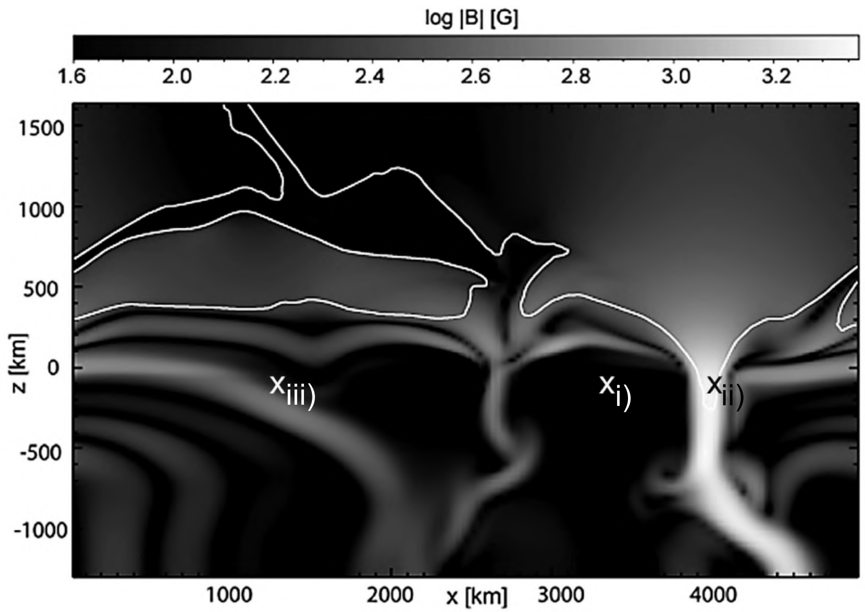

Temperature (colors), velocity (arrows), and optical depth $\tau_c = 1$ (dashed curve).

Magnetic field strength (gray scales), level where $c_s = c_A$ (white contour), locations of local wave excitation (crosses).

Movies of wave excitation at $\times_{\rm i}$, $\times_{\rm ii}$, $\times_{\rm iii}$, and along the lower boundary.

From *Nutto et al., 2012 A&A 538, A79*.

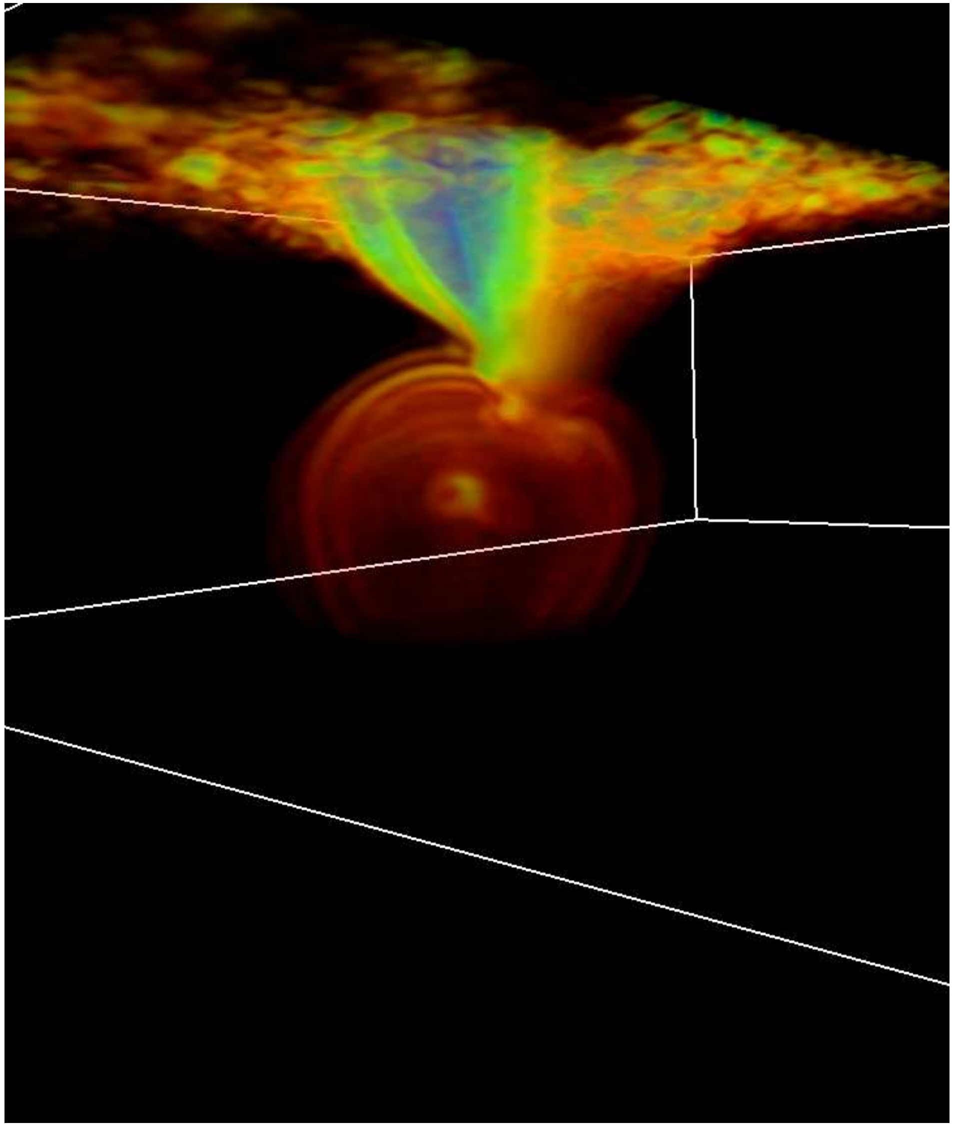

Time instant of a spherical, fast acoustic wave, initiated by a local pressure perturbation in the convection zone. When the wave encounters the low beta magnetic flux concentration in the photosphere, it partially converts into a fast magnetic mode, which shows the typical “faning out” already encountered in the 2-D simulation. Colors show absolute velocity perturbation.

Courtesy *Christian Nutto, KIS*.

§ 19.1 Magnetic halos and shadows

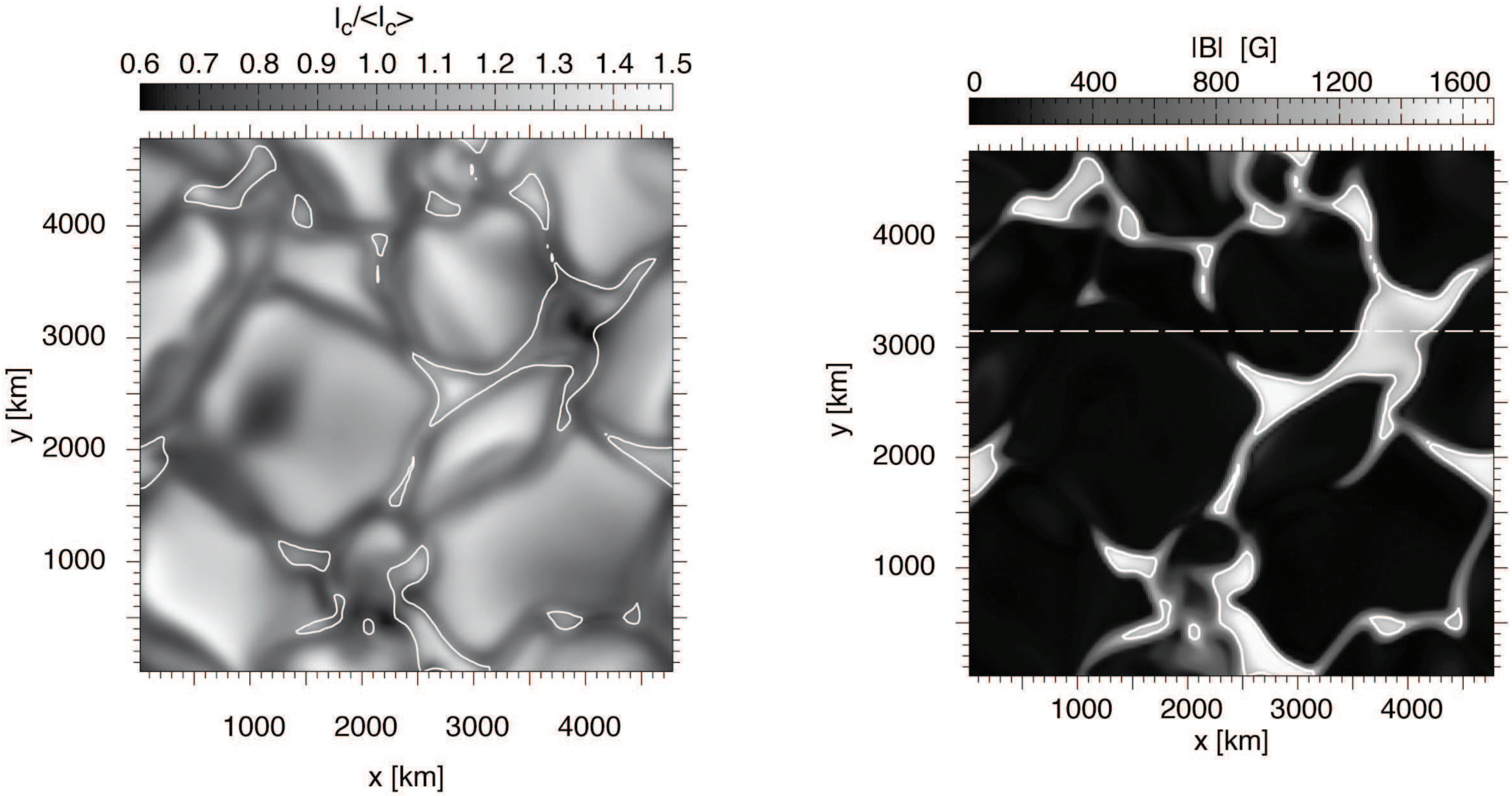

Left: FOV of $6.6'' \times 6.6''$ in white light. *Right:* Magnetic field strength at $\langle \tau_c \rangle = 1$.

Contours: Equipartition level where $c_s = c_A$. From *Nutto et al. 2012, A&A 542, L30*.

Magnetic halos and shadows (cont.)

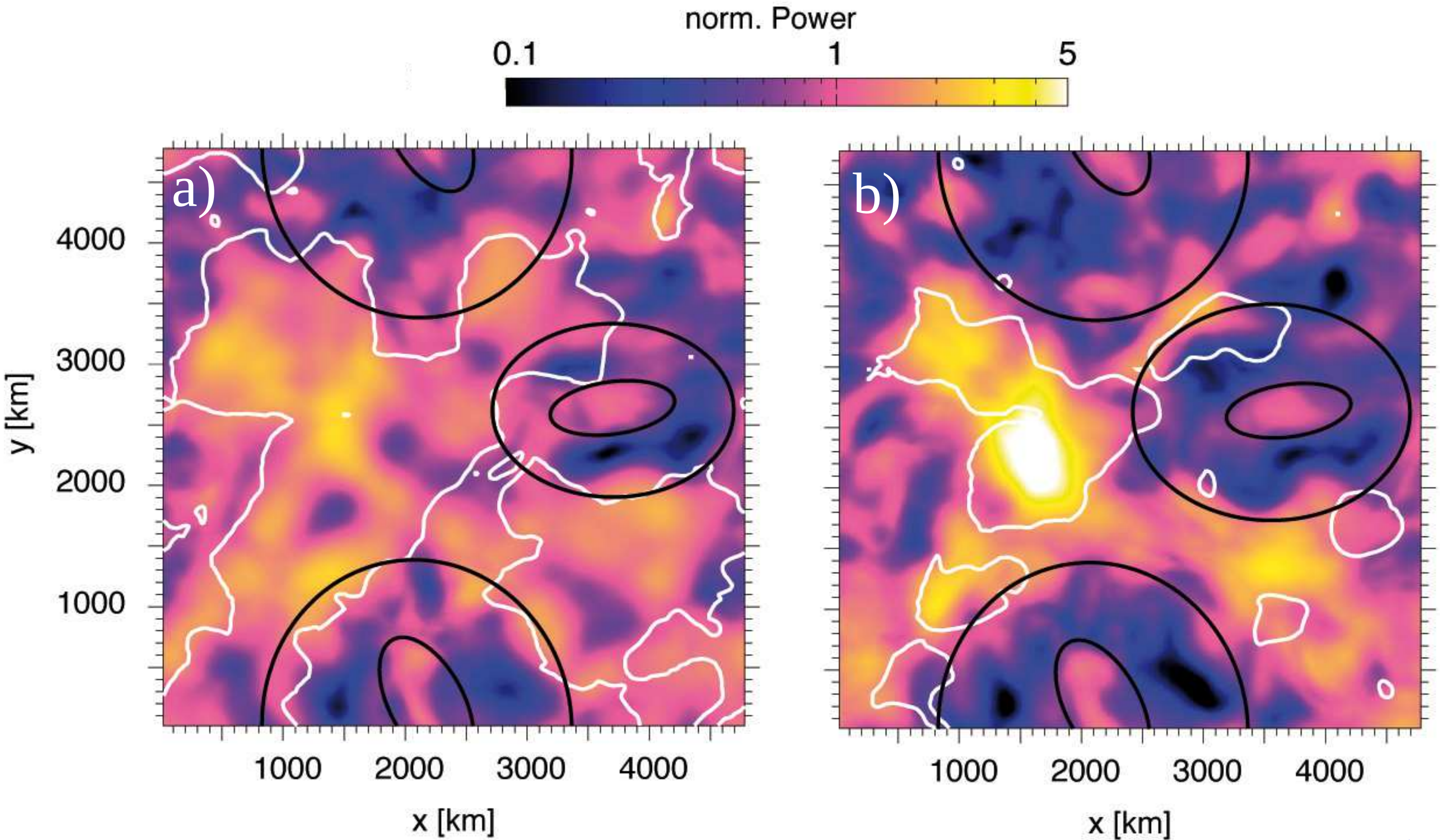

Power maps of the vertical velocity perturbations, δv_z, taken at *a)* $\tau_c = 8 \cdot 10^{-4}$ and *b)* $\tau_c = 6.7 \cdot 10^{-5}$. The *white contours* shows the equipartition level $c_s = c_A$. The *ellipses* mark regions where the *magnetic shadow* can be identified. Note suppression of power in the region between the large and the small ellipses. From *Nutto et al. 2012*.

Magnetic halos and shadows (cont.)

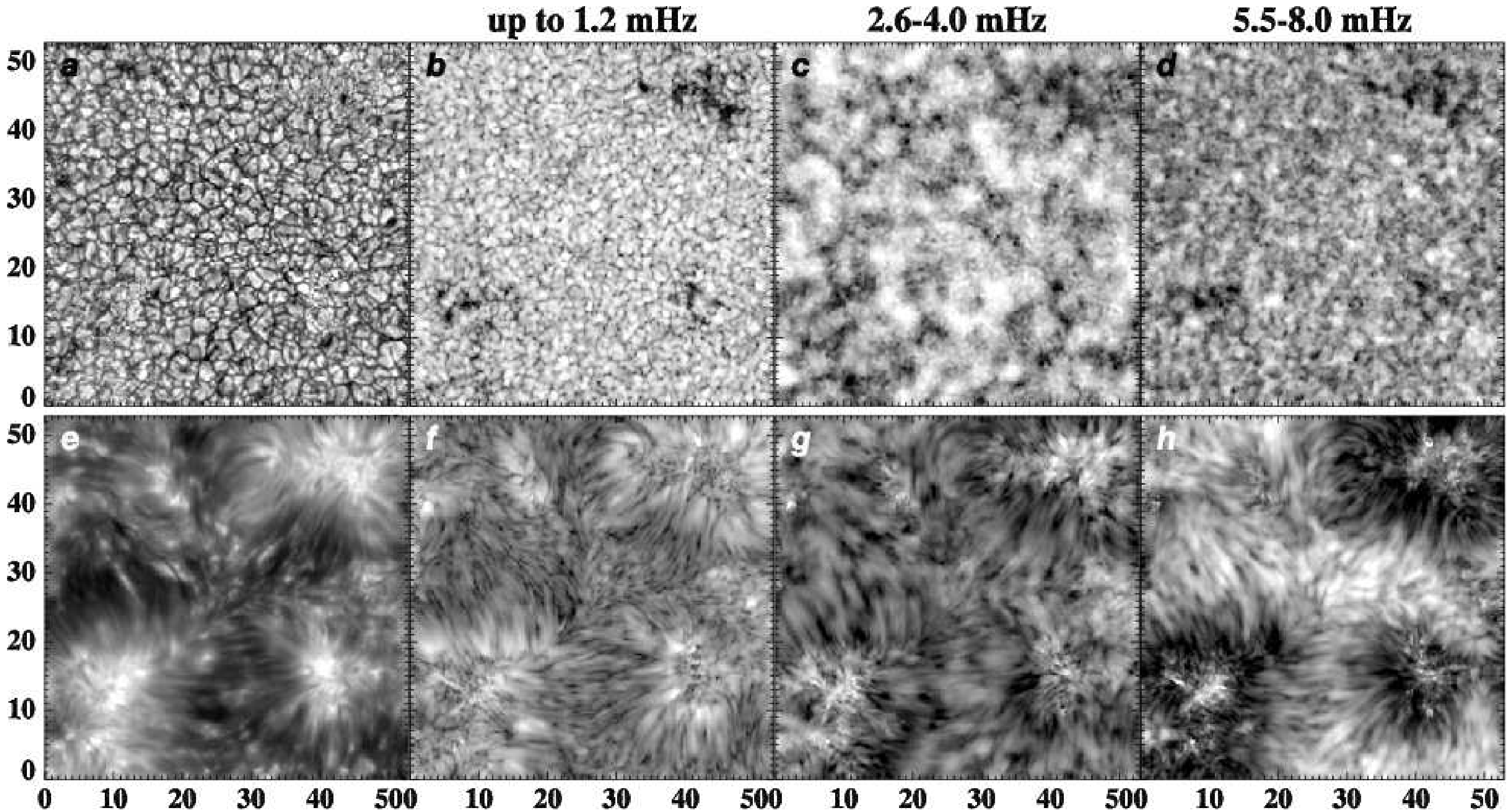

a) Broadband continuum at 710 nm. *e)* Line core intensity of CaII 854.2 nm. *b)–d)* and *f)–h)* Logarithm of the Fourier Doppler-velocity power averaged over the indicated range of frequencies of the photospheric line Fe I 709.0 nm *(b)–d))* and the chromospheric line Ca II 854.2 nm *(f)–h))*. From *Vecchio, Cauzzi, Reardon et al. (2007), A&A 461, L1.* obtained with IBIS at DST.

Magnetic halos and shadows (cont.)

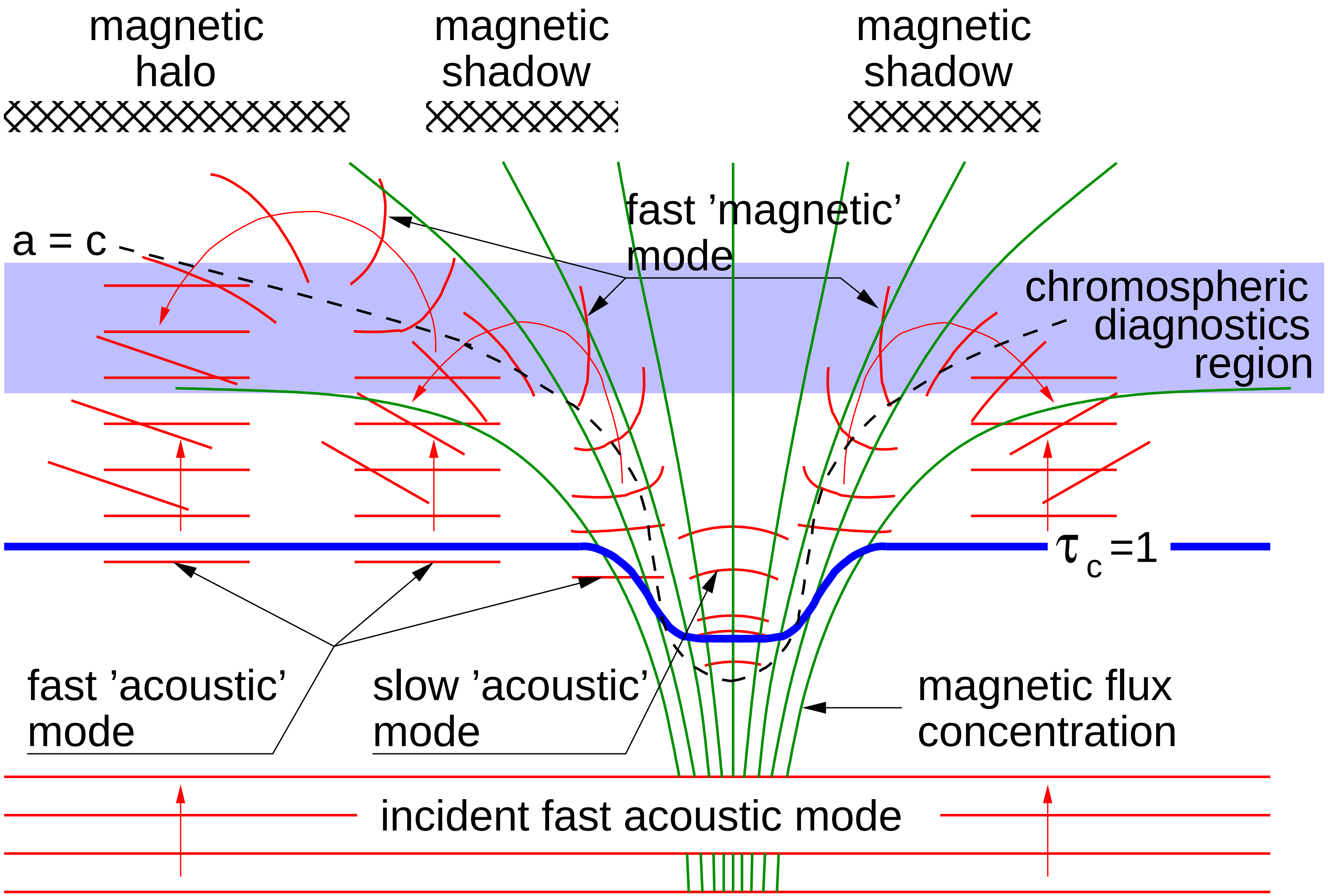

From *Komm, De Moortel, Fan, Ilonidis & Steiner, 2015 Space Sci. Rev 196, 167-199*.

Sketch of the three different magneto-acoustic modes that lead to the phenomenon of the magnetic shadow and the magnetic halo.

References

Calvo, F., Steiner, O., & Freytag, B.: 2016, *Non-magnetic photospheric bright points in 3D simulations of the solar atmosphere*, A&A 596, A43

Lites, B. W., Kubo, M., Socas-Navarro, H., Berger, T., Frank, Z., Shine, R., Tarbell, T., Title, A., Ichimoto, K., Katsukawa, Y., Tsuneta, S., Suematsu, Y., Shimizu, T., and Nagata, S.: 2008, *The Horizontal Magnetic Flux of the Quiet-Sun Internetwork as Observed with the Hinode Spectro-Polarimeter*. ApJ 672, 1237-1253

Komm, R., De Moortel, I., Fan, Y., Ilonidis, S. and Steiner, O.: 2015, *Sub-photosphere to Solar Atmosphere Connection*, in Helioseismology and Dynamics of the Solar Interior, J. Len Culhane et al. (eds.), Space Science Reviews 196, 167-199

Neckel, H. and Labs, D.: 1994, *Solar Limb Darkening 1986-1990 ($\lambda\lambda$ 303 to 1099 nm)*, Sol. Phys. 153, 91-114

Nutto, C., Steiner, O., & Roth, M.: 2012, *Revealing the nature of magnetic shadows with numerical 3D-MHD simulations*, A&A, 542, L30

Nutto, C., Steiner, O., Schaffenberger, W., & Roth, M.: 2012, *Modification of wave propagation and wave travel-time by the presence of magnetic fields in the solar network atmosphere*, A&A 538, A79

Rezaei, R., Steiner, O., Wedemeyer-Böhm, Schlichenmaier, R., Schmidt, W., and Lites, B.W.: 2008, *Hinode observations reveal boundary layers of magnetic elements in the solar photosphere*, A&A 476, L33-L36

Salhab, R.G., Steiner, O., Berdyugina, S.V., Freytag, B., Rajaguru, S.P., and Steffen, M.: 2018, *Simulation of the small-scale magnetism in main sequence stellar atmospheres*, A&A 614, A78

Sánchez Almeida, J., Collados, M., and del Toro Iniesta, J.C.: 1989, *On the generation of the net circular polarization observed in solar faculae*, A&A 222, 311

Solanki, S.K. and Pahlke, K.D.: 1988, *Can stationary velocity fields explain the Stokes V asymmetry observed in solar magnetic elements?*, A&A 201, 143

Steiner, O. & Rezaei, R.: 2012, *Recent Advances in the Exploration of the Small-Scale Structure of the Quiet Solar Atmosphere: Vortex Flows, the Horizontal Magnetic Field, and the Stokes-V Line-Ratio Method*, in L. Golub, I. De Moortel, and T. Shimizu (eds.), Hinode 5: Exploring the Active Sun, ASP Conf. Ser. 456, p. 3-32.

Stenflo, J.O.: 2010, *Distribution functions for magnetic fields on the quiet Sun*, A&A 517, A37

Stenflo, J.O.: 2011, *Collapsed, uncollapsed, and hidden magnetic flux on the quiet Sun*, A&A 529, A42

Vecchio, A., Cauzzi, G., Reardon, K. P., Janssen, K., & Rimmele, T.: 2007, *Solar atmospheric oscillations and the chromospheric magnetic topology*, A&A 461, L1